

Jamming in Granular Media: Modeling of Experimental Data

THÈSE N° 4490 (2009)

PRÉSENTÉE LE 18 SEPTEMBRE 2009

À LA FACULTÉ SCIENCES DE BASE
INSTITUT DE MATHÉMATIQUES
PROGRAMME DOCTORAL EN MATHÉMATIQUES

ÉCOLE POLYTECHNIQUE FÉDÉRALE DE LAUSANNE

POUR L'OBTENTION DU GRADE DE DOCTEUR ÈS SCIENCES

PAR

Michel TSUKAHARA

acceptée sur proposition du jury:

Prof. T. Mountford, président du jury
Prof. T. Liebling, directeur de thèse
Prof. S. Luding, rapporteur
Prof. G. Margaritondo, rapporteur
Prof. L. Pournin, rapporteur



ÉCOLE POLYTECHNIQUE
FÉDÉRALE DE LAUSANNE

Suisse
2009

Acknowledgements

First, I would like to thank Prof. Liebling for giving me the chance to carry out this PhD and for the time and energy he has invested in this work. There has been so much I have learned since arriving in his group (computer programming, lots of physics, how to write scientific papers, how to do presentations, ...). For this, I feel very lucky.

I would also like to thank the jury of my thesis and particularly Prof. Margaritondo who gave me support during my thesis.

Thank you also to my colleagues of the ROSO chair who all, at one moment or the other, helped me out in my work: Marco, Christophe, Emma, Gautier, Rodrigue, Jean-François, Gérard, Sébastien, Antoine, Mats, Alain Prodon, Marianne, Stefano, Carolina, Komei Fukuda, Jamshid, Michel Bierlaire, Michaël.

A very special thanks to Lionel Pournin who was my diploma work supervisor and has since always encouraged and helped me.

A big thanks also to all the students who have done projects under my supervision: Mohamed Amine Ajil, Raphaël Huser, Didier Francey, Gwenol Grandperrin, Laura Lakatos, and Majdi Zahaf.

My parents who have undoubtedly helped me to get this far in my studies deserve the biggest thanks. I also would like to thank my sister and her family, the Froidevaux family and all my friends for their help and support.

Finally, I would like to thank my wife Aline and our children, Zélie and Noé for all their support and love.

Abstract

This thesis studies the phenomenon of jamming in granular media, such as when a salt shaker gets clogged. We use modern instrumentation, like X-ray synchrotron tomography, to look inside real jamming experiments. High performance computers allow simulating mathematical models of jamming, but we are also able to treat some of them just using paper and pencil.

One main part of this thesis consists of an experimental validation of the distinct-element-method (DEM). In this model, grains are modeled separately, their trajectories obey Newton's laws of motion and a model of the contacts between grains is given. Real experiments of jamming of glass beads flowing out of a container were carried out. 3D snapshots of the interior of the media were taken using X-ray synchrotron tomography. These snapshots were computer processed using state of the art image analysis. It was found that 3D DEM is capable of predicting quite well the final positions of the grains of the real experiments. Indeed, in cases of instant jamming (jamming without a substantial previous flow of beads) the simulations agree well with the real experiments. However, in cases of non instant jamming, because of chaotic behavior of the model and the system, the results do not agree. Furthermore, a sensitivity analysis to grain location and size perturbations was carried out.

In a second part, we describe results on 2D DEM simulations of jamming in a hopper. We focus on the jamming probability J , the average time T before jamming and the average number ψ of beads falling through the hole when jamming occurs. These quantities were related to global parameters such as the number of grains, the hole size, the friction coefficient, grain length or the angle of the hopper (in opposition to fine-scale parameters that are the positions and radii of the grains). In agreement with intuition, a monotonic behavior of J and ψ as a function of the number of grains, the hole size, the friction coefficient was found. However, surprising results were also found such as the non-monotonicity of the average number of beads falling through the hole when jamming occurs as a function of the grain length and the hopper angle.

In the third part, we study simple probabilistic 2D models called SPM, in which non-interacting particles move with constant speed towards the center of a circular sector. Formulas giving the jamming probability or the average time before jamming when jamming occurs as a function of global parameters were found. SPM and 2D DEM were compared and a locally good correspondence between the global parameters of the two was established.

SPM led us to study some combinatorial problems, in particular two bi-indexed recurrence sequences. One gives the number of ways of placing identical balls in fixed-size numbered urns and the other the number of subsets of a given ordered set without a certain number of consecutive elements. Several different ways of computing the sequences, each advantageous in certain cases, were found.

keywords: jamming, granular media, tomography, X-ray synchrotron, distinct element method, discrete geometry, image processing, optimization, numerical simulations, combinatorics, bi-indexed recurrences, order statistics, probability and statistics

Résumé

Cette thèse étudie le phénomène du blocage dans les milieux granulaires, comme, par exemple, quand une salière se bouche. Nous utilisons des outils modernes, comme la tomographie utilisant un synchrotron à rayons-X, pour regarder à l'intérieur d'expériences réelles de blocage. La puissance de calcul des ordinateurs actuels permet de simuler des modèles mathématiques du blocage, certains que nous avons pu traiter avec papier et crayon.

Une partie importante de cette thèse consiste en une validation expérimentale de la méthode des éléments distincts (DEM). Dans ce modèle, les grains sont modélisés séparément, leurs trajectoires obéissent aux lois du mouvement de Newton et un modèle des contacts entre les grains est donné. Des expériences réelles de blocages de billes de verre s'écoulant d'un récipient ont été menées. Des instantanés 3D de l'intérieur des milieux ont été pris par tomographie utilisant un synchrotron à rayons-X. Ces instantanés ont été traités informatiquement en utilisant l'état de l'art de l'analyse d'images. Il a été trouvé que le DEM 3D est capable de prédire assez bien les positions finales des grains des expériences réelles. En effet, dans les cas des blocages instantanés, c'est-à-dire, les blocages de billes sans un écoulement important, les simulations reflètent bien les expériences réelles. Cependant, dans les cas de blocages non-instantanés le comportement chaotique du modèle et du système, font que les résultats ne correspondent pas. Une analyse de sensibilité par rapport à des perturbations des tailles et des positions des grains a été réalisée.

Dans la seconde partie, nous décrivons des résultats sur la simulation DEM 2D du blocage dans un entonnoir. On se concentre sur la probabilité de blocage J , le temps moyen T avant blocage lorsque celui-ci a lieu, et le nombre moyen ψ de billes qui passent à travers le trou lorsque le blocage a lieu. Ces quantités ont été mises en relation avec des paramètres globaux tel que le nombre de grains, la taille du trou, le coefficient de friction, la longueur des grains et l'angle de l'entonnoir (en opposition avec les paramètres locaux que sont les positions et les rayons de grains). En accord avec l'intuition, un comportement monotone de J et ψ en fonction du nombre de grains, de la taille du trou, du coefficient de friction a été trouvé. Cependant, des résultats surprenants ont aussi été trouvés comme la non-monotonie du nombre moyen de billes tombant à travers le trou lorsque le blocage a lieu comme fonction de la longueur des grains et de l'angle de l'entonnoir.

Dans la troisième partie, nous étudions des modèles probabilistes simples 2D, notés SPM dans lesquels des particules non-interagissantes, placées dans un entonnoir ayant la forme dans secteur circulaire évoluent vers le centre de ce dernier. Des formules pour la probabilité de blocage et le temps avant blocage lorsque celui-ci se produit en fonction des paramètres globaux ont été établies. Les modèles SPM et DEM ont été comparés et une correspondance, localement bonne, entre les paramètres globaux des deux modèles a pu être établie.

Les modèles SPM ont conduit à l'étude de certains problèmes combinatoires, en particulier deux récurrences à double index. La première permet de calculer le nombre de manières de placer des billes indiscernables dans des urnes numérotées à taille fixe et l'autre calcule le nombre de sous-ensembles ne contenant pas plus qu'un certain nombre d'éléments d'un ensemble ordonné. Plusieurs manières de calculer ces séquences, chacune meilleure que les autres dans certaines situations, sont présentées.

mots-clés: blocage, milieu granulaire, tomographie, synchrotron à rayons-X, méthodes des éléments distincts, géométrie discrète, analyse d'images, optimisation, simulation numérique, combinatoire, récurrence à double index, statistiques d'ordre, probabilités and statistiques

Contents

Introduction	1
I Heritage of this thesis	3
1 State of the art	5
1.1 A glimpse at the history of physics	5
1.2 Granular media	7
1.2.1 Why study granular media?	7
1.2.2 Pioneers in the study of granular media	8
1.2.3 Modern research on granular media	8
1.3 Jamming	10
1.4 Models of granular media	13
1.5 What is in this thesis?	14
2 The distinct element method	15
2.1 Updating the medium	16
2.2 DEM contact force model	17
2.2.1 Contact force model	18
2.2.2 Tuning DEM with real experiments	19
2.3 Implementation details	20
2.3.1 Numerical integration of the motion laws	20
2.3.2 Detection of contacts	20

II Fine-scale modeling	25
3 Synchrotron tomography of jamming experiments	27
3.1 Introduction	27
3.2 The experiment	28
3.3 Image analysis	31
3.3.1 The processing procedure	31
3.3.2 Results and validation of the image processing procedure	33
3.3.3 Reconstructing the exact shape and position of the container	36
4 Experimental validation of 3D DEM	39
4.1 Introduction	39
4.2 Numerical Hourglass Experiment Simulations with DEM	39
4.2.1 Procedure	39
4.2.2 Results and discussion of the experiment simulations with DEM	41
4.3 Sensitivity analysis	42
4.3.1 Perturbation experiments	44
4.3.2 Discussion of the sensitivity analysis	45
4.4 Ensemble forecasting	47
III Simple modeling, statistical physics and global modeling	49
5 Two bi-indexed recurrence sequences	51
5.1 Introduction	51
5.2 Placing balls into fixed-size urns	53
5.2.1 An introductory example	53
5.2.2 Definition of recurrence sequence $G^{(u)}(n, k)$	55
5.2.3 Interpretation of recurrence sequence $G^{(u)}(n, k)$	55
5.2.4 A first theorem for $G^{(u)}(n, k)$	56

5.2.5	A second theorem for $G^{(u)}(n, k)$	59
5.2.6	A lemma generalizing theorem 2	60
5.2.7	How to calculate values of $G^{(u)}(n, k)$	61
5.3	Subsets without consecutive elements in an ordered set	64
5.3.1	Definition of recurrence sequence $F^{(u)}(n, k)$	64
5.3.2	Interpretation of $F^{(u)}(n, k)$	65
5.3.3	Relating $G^{(u)}(n, k)$ and $F^{(u)}(n, k)$	65
5.3.4	How to calculate values of $F^{(u)}(n, k)$	66
5.4	Conclusion	66
6	Simple models	67
6.1	Introduction	67
6.2	Model SPM-D	67
6.2.1	Description	67
6.2.2	Jamming probability	68
6.2.3	Average time before jamming when jamming occurs	69
6.3	Model SPM-C	70
6.3.1	Description	70
6.3.2	Order statistics	71
6.3.3	Jamming probability	71
6.4	Conclusion	75
7	2D DEM simulations of granular jamming in a hopper	77
7.1	Introduction	77
7.2	Influence of friction, hole size, number of grains	77
7.2.1	Setup	77
7.2.2	Results and discussion	79
7.3	Influence of grain length	89
7.3.1	Setup	89

7.3.2	Results and discussion	89
7.4	Influence of hopper angle	91
7.4.1	Setup	91
7.4.2	Results and discussion	91
8	Fitting SPM and DEM	97
8.1	How to find a relationship between SPM and DEM	97
8.2	Results and discussion	98
8.3	Conclusion	100
Conclusion		103
Bibliography		105

*We're jamming, jamming
And I hope you like jamming too
– Bob Marley*

Introduction

Jamming? Where have we heard that word before? When asked what jamming is about, I think most people would answer that it is about vehicles stuck in a traffic jam, or about salt stuck in the shaker. About somethings getting stuck ... Other people may think about Bob Marley's song "Jamming", or maybe about jamming with musicians such as in a jam session. Perhaps, fewer people would think of a type of dance or rock climbing technique. This work is about the first type of jamming, where things get stuck.

We will not be interested in just anything getting stuck. Think of a ketchup tube. Sometimes ketchup also gets stuck. Jamming with ketchup will not directly be of interest in this thesis. The reason for this is that this medium is partly liquid and the molecules of it interact in a different way than salt in the salt shaker. We will concentrate on media resembling salt: granular media.

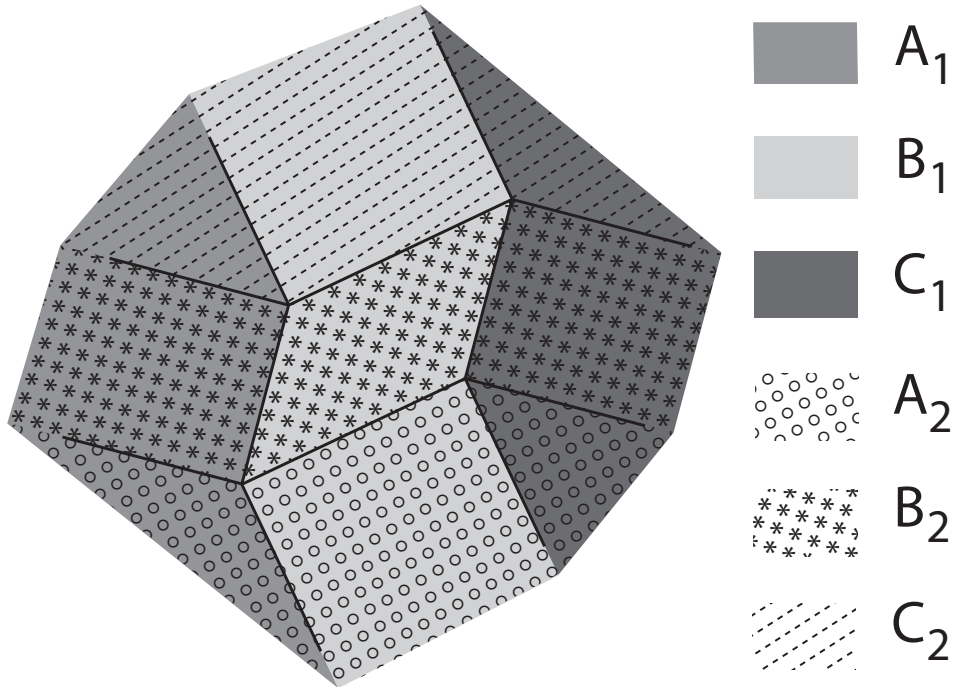
This gives an idea about the first part of the title of the thesis: Jamming in Granular Media. Here is for the second part of the title.

As it is often the case in physics, the central point is to work with models that explain and are able to predict the phenomenon. These models can be more or less precise. For example, one can model the individual grains in the salt shaker, giving an approximate position and radius for each salt grain. Or, one can be more global, measuring only the total weight of the salt grains, estimating the average angularity of the grains or measuring the hole size of the shaker. In one main part this thesis, we carry out an experimental test of a certain type of fine-scale modeling, the distinct-element-method (DEM). The goal being to find out how good this method is in predicting the microstructure, i.e. positions and radii, of a granular medium. In another main part of this thesis, we work with global models and on the relation between precise modeling and global modeling.

Organization of this report

Part 1 consists of Chapters 1 and 2 and presents the heritage of this thesis. In Chapter 1, we give a glimpse at the history of physics, survey previous research on granular media and jamming in granular media. In Chapter 2, we describe the distinct element method (DEM). Part 2 consists of Chapters 3 and 4 and presents an experimental test of 3D DEM. Chapter 3 describes how the experiments and 3D visualization of them with X-ray synchrotron tomography were carried out. Then, the computer processing and analysis of the 3D digital images is explained. Chapter 4 describes the 3D DEM simulations of the experiments. Part 3 consists of Chapters 5 to 8.

The subject of these chapters is extracting global models from fine-scale ones (see chapter 1 for the definition of global and fine-scale models). The fine-scale models used are simple models and 2D DEM. Chapter 5 is on combinatorics, it treats two recurrence sequences used in Chapter 6. Chapter 6 deals with simple models and the analytical derivation of global models. Chapter 7 deals with 2D DEM and studying by simulation (since analytical derivation is too complicated) how quantities related to jamming evolve as global parameters vary. In Chapter 8, simple models and 2D DEM are compared and related.



Part I

Heritage of this thesis

*To see a world in a grain of sand
and heaven in a wild flower;
Hold infinity in the palm of your hand
and eternity in an hour.
– William Blake*

Chapter 1

State of the art

1.1 A glimpse at the history of physics

The problem of formulating principles for nature, and the problem of predicting nature has roots in the Greek civilisation. Thoughts on the movement of bodies go back to Aristotle. After the decline of the ancient Greek civilisation until the Renaissance it is difficult to find works that stand out in physics. However, we may cite the works in optics of Alhazen (965-1039) in Cairo and those of Robert Grosseteste (1175-1253), Roger Bacon (1214-1294), Jean Buridan (1300?-1366?) and Nicolas Oresme (1323?-1382?) in the Universities of Oxford and Paris, precursors of experimental physics. On the contrary, the 16th and 17th centuries are known as the beginning of the "scientific revolution". In 1543, Nicolaus Copernicus (1473-1543) proposed heliocentrism in opposition to geocentrism that the ancient Greek philosophers believed in. At fairly the same time, new mathematics are developed. For example, Tartaglia and Cardano find the algebraic solutions to the cubic and quartic equations. A bit later, physics and mathematics join to better capture the "laws of nature": Galileo (1564-1642) proposes a precise law for the free fall of bodies submitted to earth's gravity. He also proposes the basic principle of relativity: the laws of mechanics are the same for all observers having a non-accelerating movement. He uses his telescope to observe the phases of Venus, thus formally excluding geocentrism.

Influenced by these works, Isaac Newton (1643-1727) formulates his laws of motion and the universal law of gravitation [Newton, 1687]. He proposes thus, a general theory capable of predicting many physical phenomena. Differential calculus invented by Newton and Gottfried Leibniz (1646-1716) allows a natural formulation of this theory. The successes of Newton's theory are many. Let us give a few examples. In 1801, Carl Friedrich Gauss (1777-1855) invented the least squares method and relocated the position of the planetoid Ceres that was lost to astronomers. In 1846, the planet Neptune is found not by observation but by the predictions of Sir George Airy (1801-1892) and Urbain Le Verrier (1811-1877). Note that even today, Newton's theory is still successful, since it allows space conquest.

When James Clerk Maxwell (1831-1879) presents his general theory of electromagnetism, the success of physics in predicting natural phenomena seems complete. However, at the turn between the 19th and 20th centuries, different observations are in contradiction with classical predictions.

In 1881, Albert Michelson (1852-1931) shows that the principle of relativity stated by Galileo does not apply to light. In 1905, Einstein with special relativity, proposes a theory that explains this observation. Newtonian physics is in fact a special case of Einstein's theory.

There is also another problem with classical mechanics that was noticed by physicists at the end of the 19th century: it cannot predict the intensity of black body radiation. In 1900, Planck proposes that electromagnetic radiation is quantified and finds a good prediction of this intensity. This is the beginning of quantum physics which deals with the physics of elementary particles. It is not the purpose here to survey quantum mechanics. However, we will evoke one property which is of interest to us. A fundamental idea in quantum physics is that it is impossible to dissociate the measuring instrument from the microscopic object we want to measure. The formal statement of this in quantum mechanics is Heisenberg's uncertainty theorem.

One more problem, observed at fairly the same moment, complicates things a bit more. Henri Poincaré (1854-1912) while dealing with the mathematical resolution of the 3-body problem, realized some solutions don't allow an asymptotic analysis. This is the cornerstone of chaos theory. The central point in this theory is that for certain mathematical problems, small differences in initial conditions can lead to large divergences over time. The first observation of this phenomenon came later on with Lorenz's treatment of hydrodynamic flow on a computer in 1963 [Lorenz, 1963].

These discoveries hinted that uncertainty is likely to take an important place in physics.

While many physicists were working on finding the adequate theories, a new subject emerged: statistical physics. The main idea behind statistical physics is to relate microscopic parameters of a system to some macroscopic parameters.

The roots of statistical physics go back to the development of the kinetic theory of gases. In 1738, Daniel Bernoulli (1700-1782) derived the Boyle-Mariotte law for ideal gases from Newton's laws of motion and the hypothesis of the random motions of the gas particles. A century later, the ideal-gas law was proved theoretically with the work of John Herapath (1798-1868) and James Prescott Joule (1818-1889). In 1859, by assuming independent random motions, James Clerk Maxwell found the velocity distribution of the molecules of a gas in equilibrium. In 1868, Ludwig Eduard Boltzmann (1844-1906) further studied this distribution but also found the statistical meaning of entropy, thus giving new insight into thermodynamics. We may also cite Rudolf Emmanuel Clausius (1822-1888), Josiah Willard Gibbs (1839-1903) and Max Planck (1858-1947) other participants in the first developments of statistical physics. Statistical physics is also applicable to quantum phenomena. Remarkable examples of quantum statistical physics are the Bose-Einstein statistics and the Fermi-Dirac statistics which give the distribution of bosons and fermions over energy states for a system in thermal equilibrium.

Among the modern derivatives of statistical physics one finds the mathematical fields of stochastic theory and ergodic theory but also in physics, the study of critical phenomena, hydrodynamics, or the theory of super fluids.

Although physics has since continued its progression, the pioneers cited in this glimpse have undoubtedly given a framework for physics, from which this thesis inherits.

The material in the section above is based on [Perdijon, 2008].

1.2 Granular media

In this thesis, we work with materials called granular media. Different definitions of a granular medium are possible. Here, we define a granular medium as a set of objects that we may suppose:

- 1) are not subject to thermal agitation
- 2) do not exert forces at distance on each other.

This definition excludes the objects of the atomic and mesoscopic scale subject to thermal agitation (atoms, for example) and the objects of the astronomical scale subject to forces at distance (planets). On earth, the size of objects that make a granular medium is roughly found in between $100 \mu\text{m}$ (a small sand grain) and 100 m (an iceberg). Examples of granular media are sands, cereals, pharmaceutical pills or snow.

Interesting phenomena, not yet well understood take place with granular media. These are for example: avalanches, segregation (when grains of different type separate under vibration), crystallization (when grains arrange into ordered configurations), pattern formation (when grains arrange into patterns, such as dunes or ripples) or jamming (when the flow of grains stops abruptly).

1.2.1 Why study granular media?

Above, we gave as examples of granular media, sands, cereals, pharmaceutical pills or snow. These few examples show how pervasive granular media are in nature and in daily life. Let us give a few examples of why better understanding granular media could be useful. A better understanding of avalanches could help avoid serious accidents caused each year by snow avalanches and rock slides. A better understanding of granular compaction could help in building better materials for the construction industry. In the food and the pharmaceutical industry, problems caused by grain segregation, compaction or jamming are common. Help would come with a better design of grain silos, containers and hoppers.

To tackle these problems, one must find the mathematical models capable of predicting the behavior of granular media. We will see a bit further the different types of models scientists already use. Some model each grain separately and others model more global parameters. The important question is how to find the most adequate model. One may for example, imagine a

model that is based on the molecular structure of each grain and try to predict the flow of the media through a hopper. Due to the large number of grains and the large number of calculations this supposes, such an attempt would be currently unfeasible. On the other hand, one may imagine modeling the media by global parameters such as its center of gravity or its viscosity. With such a model, one would probably miss important aspects of the contact between grains. Aside from the economic and industrial interest in studying granular media, understanding the way to handle its modeling has an importance in science.

1.2.2 Pioneers in the study of granular media

During the Renaissance, Leonardo da Vinci (1452-1519) devised experiments demonstrating the laws of dry friction. At the end of the 18th century, Charles de Coulomb (1736-1806) introduced a law of dry friction between solids. This may be considered as one of the cornerstones of the study of granular media, since the Coulomb's law gives a model of the contact between grains. In 1780, Ernst Chladni (1756-1827) noticed the difference in behavior between light granulars and heavier ones. He observed what is known as Chladni's complementary figures. Michael Faraday (1791-1867) studied how vibrations induced the formation of sandpiles. William Rankine (1820-1872) studied the theoretical implications of friction in granular media, work which led to Rankine's passive and active states. The problem of the equilibrium distribution of forces in a granular medium stored in a silo has been studied by I. Roberts, H. Janssen and John Strutt, Lord Rayleigh (1842-1919). Osborne Reynolds (1842-1912), also famous for his work in hydrodynamics, made some important contributions to the theory of granular media such as the concept of dilatancy.

The facts in the preceding paragraph can be found in [Duran, 2000].

1.2.3 Modern research on granular media

Since the beginning of the 20th century, the number of scientists and engineers studying granular media has increased rapidly. We give here an account of different problems that are still active research topics in the field. This should help the reader in grasping in what context this thesis lies.

1) Avalanches

The angle of repose is the maximum steepness that a heap of the material can have while being stable. When the heap is steeper, an avalanche occurs. In the 1950's, several authors have studied the angle of repose of granular materials [Neumann, 1953; Train, 1958; Rose and Tanaka, 1959]. The reader may refer to the bibliography in [Savage and Hutter, 1989] for contributions to avalanche study from the 1960's to the 1980's. Here are some examples of research on avalanches in the last 20 years or so. In [Tang and Bak, 1988]

and [Bak et al., 1988], the authors show how a cellular-automaton model of avalanche dynamics tends to a self-organized critical state. In [Savage and Hutter, 1989], the granular mass in an avalanche is treated as a frictional Coulomb-like continuum with a Coulomb-like basal friction law and numerical predictions are found in good agreement with the laboratory experiments of Huber [Huber, 1980]. In [Rajchenbach, 1990], Rajchenbach observes the transition from intermittent avalanches to a steady regime in the flow of granular materials. He establishes experimentally the relation between the current and the slope in the regime of steady flow. In [Evesque, 1991], Evesque studies experimentally glass-sphere avalanches in a drum and uses concepts and results from soil-mechanics to explain the results. In [Ancey et al., 2003], the authors propose a method to obtain the probability distribution of the frictional coefficient of avalanche models. In [Forterre and Pouliquen, 2003], Forterre and Pouliquen study the long-surface wave instability of a granular medium flowing down a rough inclined plane. Their theory based on the Saint-Venant equations is able to predict the stability threshold. In [Börzsönyi et al., 2008], Börzsönyi et al. study avalanche dynamics on a rough inclined plane experimentally and propose depth-averaged theoretical description that captures the dynamics, notably the two regimes of avalanche motion. For a survey of important results on the physics of avalanches, the reader may also refer to the preceding article and its bibliography.

2) Formation of dunes or ripples

The formation of dunes or ripples with granular materials is another subject which is still actively studied. There is interest in the topic already at the beginning of the 20th century [Hahmann, 1912]. R. A. Bagnold wrote a book on the subject, published in 1941, which has become a classic [Bagnold, 1941]. We give here some examples of articles on the subject of dunes that have been published in the last 50 years. In [Kennedy, 1963], Kennedy proposes an analytical model of free-surface flow over an erodible bed and predicts wavelengths of antidunes and ranges of wavelengths of dunes and conditions for change of bed configuration that are in good agreement with experimental data. In [Engelund, 1970], Engelund proposes a two-dimensional mathematical model based on the vorticity transport equation. The model takes account of the internal friction. In [Richards, 1980], Richards presents a theory that predicts the occurrence of two separate modes of instability postulated to correspond to the formation of ripples and dunes respectively. In [Fisher and Galdies, 1988], Fisher et Galdies present a computer model for barchan dune movement. In [Sauermann et al., 2000], Sauermann et al. study the shape of barchan dunes and propose a simple model that correctly explains the differences between barchans where the crest and the brink coincide and those where they do not. In [Herrmann and Sauermann, 2000], Herrmann and Sauermann present a model based on coupled differential equations that can describe the formation and evolution of dunes. The details do not agree with field measurements however the crescent shape of barchan dunes is reproduced by simulation. In [Andreotti et al., 2006], Andreotti et al. report an experimental investigation of aeolian sand ripples. They show that the initial and final wavelengths and the propagative speed of the ripples are linear functions of the wind velocity.

3) Segregation

When subject to vibrations, granular media tend to segregate, i. e. grains having different characteristics separate. In India, peasants use segregation to separate their harvest from other materials. The phenomenon is also well known in Brazil: during the transport of nuts on the rough roads, the larger nuts end up on top of the smaller ones. This has led segregation to be often called the "Brazil-nut effect". The effect was also well known by miners who used it to separate the wanted rocks, such as gold, from the rest. Among the first studies on segregation is Oyama's experiment in which two granular materials of same type but different size eventually segregate in a rotating drum [Oyama, 1939]. Other researchers are also interested in the problem at the time such as Brown who gives in [Brown, 1939] some principles of segregation. In 1987, Rosato et al. [Rosato et al., 1987] show how the Monte-Carlo method can reproduce segregation. Vanel et al. [Vanel et al., 1997] report experiments on the rise-time with frequency f of a large sphere in a vibrated bulk solid and deduce a law $f \sim d^{-\frac{1}{2}}$, where d is the diameter of the particles of the bed. In [Abreu et al., 2003], Abreu et al. study the influence of particle shape on segregation through Monte Carlo simulations using spherocylinders. They show that for a mixture of spheres and short spherocylinders, the spheres move upwards while for a mixture of spheres and long spherocylinders the opposite happens. In [Schnautz et al., 2005], Schnautz et al. show that "event-driven" computer simulations reproduce correctly the main aspects of experimental horizontal segregation. In [Ciamarra et al., 2006], Ciamarra present molecular dynamics simulations to study the influence of different properties on the Brazil nut effect and the reverse Brazil nut effect (where larger grains segregate towards the bottom). In [Ramaoli, 2008], Ramaoli compares segregation experiments of cereals in vibrated box with DEM simulations. He shows an overestimation of segregation by the simulations. Experimental shape segregation and simulations are presented and found in good agreement.

4) Crystallization

Another phenomenon of granular media which is of interest is the ordering of grains, when for example they flow or are subject to vibrations. The term crystallization is often used to describe this phenomenon since the grains tend toward ordered configurations that remind us of crystalline configurations.

In [Villarruel et al., 2000], Villarruel et al. report on the experimental ordering of rods under vertical vibrations. In [Pournin et al., 2005], Pournin et al. show that DEM computer simulations faithfully reproduce the phenomena. In [Galanis et al., 2006], Galanis et al. find density dependent isotropic-nematic transition of vertically vibrated granular materials confined to quasi-2D containers. In [Ramaoli et al., 2007], Ramaoli et al. study the influence of particle geometry and vibration acceleration on rod-ordering and propose a theory that explains simulation findings.

1.3 Jamming

We give here a survey on research on jamming in granular media and on the closely related problem of granular flows.

Lucretius, the natural philosopher in Rome already noted that "One can scoop up poppy seeds with a ladle as easily as if they were water and, when dipping the ladle, the seeds flow in continuous stream". It is this property of grains that allowed the invention of the hourglass, in the third century at Alexandria, it is said. The earliest known hourglass appears in the 1338-40 fresco Allegory of the Good Government by Ambrogio Lorenzetti. So, long before the industrial age people already noticed or used the properties of granular media and its flow.

It is possible that granular flows and jamming have been studied before the 20th century. However, with our bibliographic search, we have not found any information on this. It should be interesting to pursue bibliographic research on this. The book by Brown and Richards [Brown and Richards, 1970], which has become a classic gives a survey of the works on granular media in the 20th century up to 1970. Here, we give a summary of the sections that concern granular flows and jamming.

Brown and Richards first present different experimental methods to study flow patterns. One is to use a bin or hopper with a transparent wall containing alternate layers of colored and uncolored powder [Meldau and Stach, 1934; Kvapil, 1959]. Zenz and Othmer [Zenz and Othmer, 1960] propose a transparent wall with a slight static charge and dusted it with a colored powder that allowed to observe the flow. The different kinds of flows that have been studied are presented. In [Jenike, 1954], Jenike describes the pattern of discharge of powder from a cylindrical bin. In [Brown and Hawksley, 1947], Brown and Hawksley study the discharge of powder from a 2-dimensional "flat bin" and give the main characteristics of such flow. In [Brown and Richards, 1959a], Brown and Richards discuss the discharge of beads from a conical hopper. The flow of wet coals in closed chutes has been investigated by Wolf and von Hohenleiten [Wolf and von Hohenleiten, 1945, 1948]. The flow in presence of flow regulators has been studied by [Brown, 1950; Kvapil, 1959]. Discharge rates are discussed. Researchers in the first half of the 20th century have reported that the rate of discharge is independent of the head of material in the bin unless the vessel be nearly empty [Deming and Mehring, 1929; Bingham and Wikoff, 1931; Rausch, 1949; Franklin and Johanson, 1955]. Several researchers tried to correlate flow rate from flat-bottomed bins with material properties, using the bulk density as placed in the container [Rausch, 1949; Franklin and Johanson, 1955; Wieghardt, 1952]. However, as explained in [Brown and Richards, 1970] this method obscures the influence of material properties since the bulk density is a combination of particle density and initial packing characteristics. In [Rausch, 1949], The effect of a current of air passing upwards through the orifice was shown to be large.

Brown and Richards also evoke the obstruction of flow. In [Brown and Richards, 1959b] Brown and Richards measure blocked apertures of non-cohesive powders. In [Brown, 1961], Brown studies the largest aperture for which flow without assistance is not possible. He shows that larger particles obstruct the flow more than small particles, that moist particles obstruct the flow more than dry particles, that angular granules obstruct the flow more than spherical particles and that a consolidated bed of fine powder obstructs the flow more than loose one.

From the late 1960's to the late 1990's, several theories on granular flow through orifices and arching have been proposed. In [Beverloo et al., 1961], for example, Beverloo et al. propose an equation for the flow of seeds through a circular orifice. A whole category of papers deal with the problem of designing mass flow hoppers. In [Jenike, 1961], Jenike first proposed a theory of arching that can be applied to the problem. Different modifications to his initial theory have been proposed [Walker, 1966; Stainforth and Ashley, 1973; Enstad, 1975; Drescher et al., 1995a]. In [Drescher et al., 1995b], Drescher et al. experimentally determine the critical outlet size that prevents arching and compare the results with the existing theories. They show that these theories overestimate the outlet size. Many authors have proposed results on the determination of the flow properties, the reader can consult the bibliography in [Drescher et al., 1995a] for further information.

Since the end of the 1990's, there has been an increase of articles published on jamming in granular media as well as on the link between jamming in granular media and the glass transition in colloids and liquids.

Cates et al. first proposed that colloids and granular media might share the jamming phenomenon [Cates et al., 1998] and that both should belong to the new class of "fragile matter" because of their instability to stress. They limit their point of view to systems without attractive interactions and where there is no thermal motion. In [Liu and Nagel, 1998], Liu and Nagel pursue the thesis further, proposing that actually the jamming phenomenon is shared also by liquids when they are supercooled and become glasses. This phenomenon, known for millennia, is called the glass transition. They propose a jamming diagram that encompasses jamming for granular media, colloids and liquids. To et al. [To et al., 2001] studied the jamming of granular flow in a two-dimensional hopper. They show that the jamming probability decreases when the ratio, $d = \frac{R}{D}$, between hopper opening R and grain diameter D , increases. They also partly reproduce the jamming probability results by using a random walker model. In [Trappe et al., 2001], Trappe et al. study experimentally the fluid to solid transition of weakly attractive colloidal particles and find evidence that jamming is shared also by colloids. Silbert et al. study packings of frictionless and frictional spheres in three dimensions, found with molecular dynamics simulations [Silbert et al., 2002b]. They find that the packings of hard spheres are always isostatic (with six average contacts) and that frictional packings vary according to system parameters and construction history. This result is related to the subject of jamming since packings can be considered to be in jammed state. In [Silbert et al., 2002a], Silbert et al. study three-dimensional chute flow simulations of granular systems, and find more evidence of the analogy between granular jamming and the liquid-glass transition. In [To, 2002], To shows the influence of the hopper angle in granular jamming in a hopper. He shows the intuitive result that the jamming probability decreases when the steepness of the hopper decreases. In [O'Hern et al., 2003], O'Hern et al. study jamming at zero temperature and zero applied stress. They show some properties of this kind of jamming. Zuriguel et al. [Zuriguel et al., 2003], studying jamming in a container with outlet, find that the jamming probability decreases as the ratio between the orifice size and the radius of the beads is increased and propose to use a one-dimensional percolation model that reproduces correctly the relation between the mean avalanche size and the jamming probability. In [Donev et al., 2005], Donev et al. study how the pair correlation function is formed as jamming is approached for disordered and ordered hard-sphere packings. In [Zuriguel et al., 2005], Zuriguel et al. obtain experimental data on the number of grains that fall between consecutive jams in a silo with an outlet. They show that there is a power-law divergence of the mean avalanche size and critical radius beyond which no jamming can occur. They

also study the dependence of the arch formation probability on the material properties and shape of the grains. They find that while the former influences little the arch formation the latter does. In [To, 2005], To study experimentally metal disks flowing through two-dimensional hoppers and treats the states of the hopper as a Markov chain to find an equation for the dependence of the jamming probability on the exit size. In [Corwin et al., 2005], Corwin et al. find evidence for a structural signature of jamming, by measuring the contact-force distribution between particles in shearing experiments. In [Henkes and Chakraborty, 2005], Henkes and Chakraborty build a field theory of frictionless grain packings in two dimensions and show the existence of a critical point that corresponds to jamming. Silbert et al. simulate soft-sphere packings just above the onset of jamming [Silbert et al., 2006]. They find that the pair correlation function gives distinct signatures of the jamming transition. In [Majmudar et al., 2007], Majmudar et al. find a good agreement between their experiments and the simulation results found in [Silbert et al., 2002b; O’Hern et al., 2003]. They also find a reasonable agreement with the field theory of Henkes and Chakraborty [Henkes and Chakraborty, 2005]. In [Matchett, 2007], Matchett studies arch formation through continuum theories as proposed by Jenike and others. In [Keys et al., 2007], Keys et al. study spatially heterogeneous dynamics in a system of air-driven granular beads. This is a phenomenon seen in supercooled liquids and colloidal suspensions, where it is increasingly pronounced as the system reaches the glass transition [Ediger, 2000]. In [Pournin et al., 2007], Pournin et al. study distinct element method simulations and experiments of granular jamming and find a good agreement between the two. In [Lu et al., 2008], Lu et al. propose a thermodynamic model of granular jamming that successfully predicts the entropic data of five molecular glasses thus giving further evidence of the universality of the jamming concept. In [Ballesta et al., 2008], Ballesta et al. study dynamical heterogeneities in colloidal suspensions very close to the jamming transition. In [Longjas et al., 2009], the authors propose a theory that allows expressions for the jamming probability in a two-dimensional hopper and carry out experiments. They find a good agreement between theory and experiment. Mailman et al. study numerical packings of frictionless ellipses and find that jamming is different than for spherical particles [Mailman et al., 2009]. Mankoc et al. study experimentally the jamming of grains in a silo with orifice, when the silo is subject to vibrations [Mankoc et al., 2009]. They show that the breakage of blocking arches once they have been formed is responsible for the increase of flow in gently vibrated silos. In [Pournin et al., 2009], Pournin et al. study with distinct element simulations the influence of particle shape and friction on granular jamming.

1.4 Models of granular media

One may safely suppose that most of the subjects of physics, such as classical mechanics, quantum mechanics, statistical physics, that we hinted in section 1.1 are related in one way or another with the physics of granular media. Indeed, a granular medium is constituted of individual grains which are in their turn constituted of molecules, in their turn constituted of atoms, ...

It seems that we are a step away from seeing "a world in a grain of sand". However, in reality, scientific studies of granular media do not totally take this into account. To explain why, we repeat a simple example: should one want to design the shape of an industrial hopper, modeling each molecule of each grain is not feasible, even with a powerful computer, due to the excessive

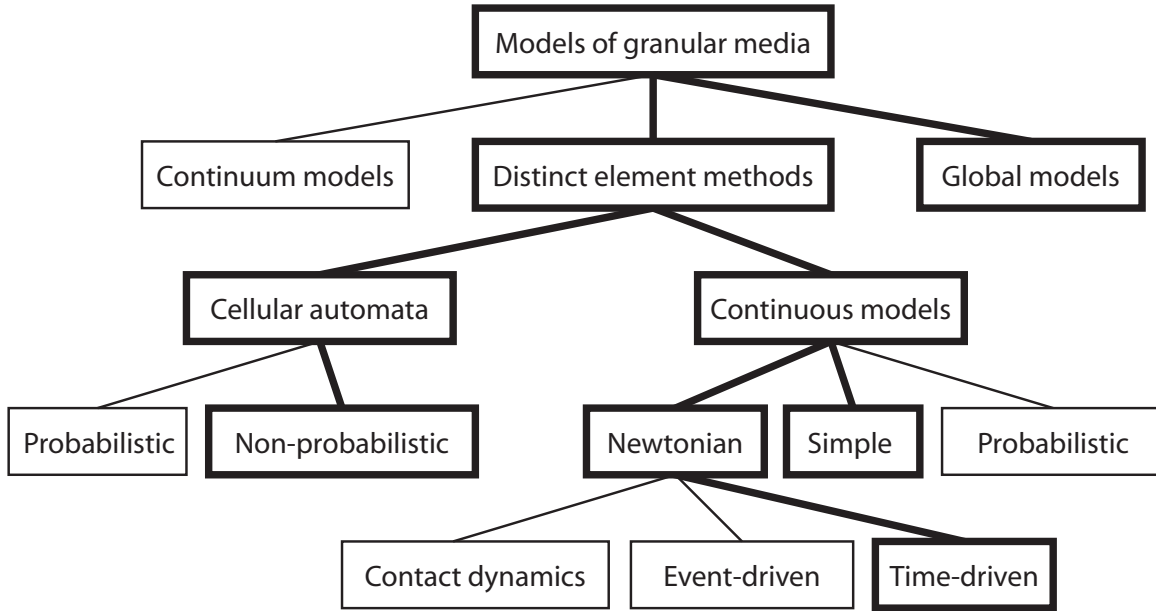


Figure 1.1: Classification of models of granular media. Types of models used in this thesis are highlighted.

number of calculations. We are limited to essential features of the grains.

In sections 1.2 and 1.3, we have surveyed different feasible ways of modeling granular media. In Fig. 1.1, we give a classification of these based on the classifications of [Hogue, 1993] and [Müller, 1996].

The models of granular media given in Fig. 1.1 enter three main categories: continuum models, where the medium is treated as a continuous object characterized at each point by parameters such as velocity or pressure, distinct element methods (which we also call fine-scale models), in which the medium is given by a description of individual grains and global models, where the medium is given by some parameters not specific to individual grains (such as the average angularity or average friction coefficient). Among the distinct element methods, cellular automata are models in which particles move on a discrete set of sites. The laws that control the movement of the particles can be deterministic or probabilistic. In continuous models the particles move on a continuous set of sites. Among them are Newtonian models: individual grains follow Newton's laws of motion and Newton's law of gravitation. In this thesis, we use time-driven Newtonian models in which, in opposition to event driven models where scheduling of the system is based on the contacts (events), scheduling of the events is based on the time step. Continuous models may also be probabilistic, for example Monte-Carlo methods. We introduce a new kind of continuous deterministic models: simple models. In our case, particles are non-interacting and an analytical treatment of the models is possible. In Fig. 1.1, the models that were used in this thesis are highlighted.

Depending on which phenomenon is studied, one or the other model may be used. For phenomena involving a huge quantity of grains like avalanches or dune formation, continuum models can be preferred. For phenomena visible already for small amounts of grains like segregation or crystallization distinct element modeling is usually preferred. Global models are also used

when the number of grains is large. Often, as it is done in this thesis global models are derived from fine-scale models. This derivation may be considered as a statistical physics approach.

Even if currently the modeling of granular media has a lower bound which is the grain, there are open questions. How good are the known models in predicting the behavior of granular media? How must one best use these models to predict its behavior? What are the relations between the different models? What will future models look like? In this thesis, we begin to answer these questions.

1.5 What is in this thesis?

In this thesis, we will present an experimental verification of the distinct element method (this is in fact the name given to a Newtonian method). This work will allow to understand better the limits of precise modeling and how to best use it to predict real experiments. We will also present two models of granular media, which may be seen as an extremely simple distinct element method and, as is often done in statistical physics, derive analytically, global models from them. This will require some mathematical studies, in particular on recurrence relations. We will also derive global models from the 2D distinct element method using results on the simple models.

I do not know what I may appear to the world; but to myself I seem to have been only like a boy playing on the seashore, and diverting myself in now and then finding a smoother pebble or a prettier shell than ordinary, whilst the great ocean of truth lay all undiscovered before me.

– Isaac Newton

Chapter 2

The distinct element method

The distinct element method (DEM) is used for simulating the behavior of granular media. It was originally developed by Cundall and Strack [Cundall and Strack, 1979] for spheres. The idea behind DEM is to follow the trajectory of each grain (hence the name distinct element method). Grains evolve obeying Newton's laws of motion, his law of gravitation and a given model of the contacts between grains, and grains and walls. Thus, this method is found in the category of Newtonian models described in section 1.4. Numerical integration of the laws of motion is used to implement DEM on a computer.

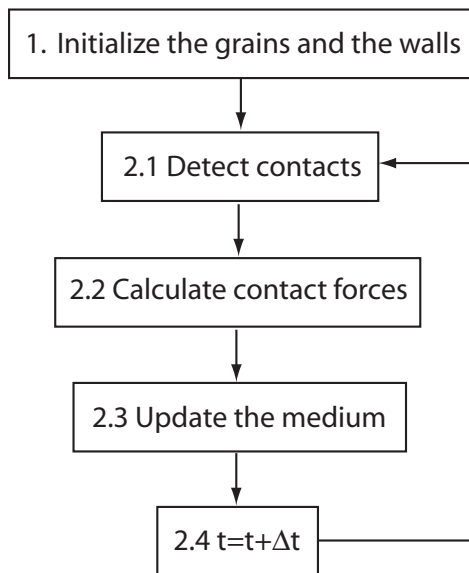


Figure 2.1: Flowchart showing the main steps in a distinct element method computer program

The philosophy behind DEM resides mainly in the modelisation, however other practical problems arise when implementing it, see section 2.3.

The flowchart in Fig. 2.1 shows the main steps in a DEM computer program. This flow chart highlights the essential ingredients of a DEM program which we will detail below.

2.1 Updating the medium

In [Newton, 1687], Newton formulates three laws of motion and a law of gravitation that allow to predict many physical phenomena. They provide the basis for the movement of grains in DEM.

1) First law:

If a body is at rest or moving at a constant speed in a straight line, it will remain at rest or keep moving in a straight line at constant speed unless it is acted upon by a force.

2) Second law:

The time rate of change of the momentum of a body is equal in both magnitude and direction to the force imposed on it.

3) Third law:

When two bodies interact, they apply forces to one another that are equal in magnitude and opposite in direction. The third law is also known as the law of action and reaction.

4) Law of gravitation:

Any particle of matter in the universe attracts any other with a force varying directly as the product of the masses and inversely as the square of the distance between them.

We state these laws as found in the Encyclopedia Britannica on the world wide web.

The second law describes the movement of a body in presence of influences called forces. It states that for a body with constant mass, its acceleration times its mass is equal to the sum of forces exerted on the body.

The third law describes an aspect of forces: two bodies exert forces opposite and of same magnitude on each other.

The magnitude of the gravitational force between the two point masses may be written as:

$$F = G \frac{m_1 m_2}{r^2}, \quad (2.1)$$

where G is the gravitational constant, m_1 is the mass of the first point mass, m_2 is the mass of the second point mass and r is the distance between the two point masses.

From Newton's laws one can derive the general laws of movement for a solid. For a solid of center of gravity \vec{g} , mass m , inertia matrix I at \vec{g} , velocity of center of gravity \vec{v} and spin vector $\vec{\omega}$, they read

$$\vec{F} = \frac{d\vec{p}}{dt}, \quad (2.2)$$

where $\vec{p} = m\vec{v}$ and \vec{F} is the total force acting on the solid, and

$$\vec{M} = \frac{d\vec{L}}{dt}, \quad (2.3)$$

where $\vec{L} = I\vec{\omega}$ and \vec{M} is the total momentum at \vec{g} .

The calculation of the grain inertia matrices is an important point in DEM. Let S be a homogeneous solid, of density ρ . The inertia matrix I of S with respect to its center of gravity and an orthonormal basis (x, y, z) is

$$I = \rho \int_V \begin{pmatrix} y^2 + z^2 & -xy & -xz \\ -xy & x^2 + z^2 & -yz \\ -xz & -yz & x^2 + y^2 \end{pmatrix} dx dy dz. \quad (2.4)$$

The reader can refer to [Pournin, 2005] for the calculations of inertia matrices of specific grains.

The general laws of movement for solids, Newton's third law and the law of gravitation are main ingredients for DEM: they predict how the grains move according to the forces present and the gravitational force present on earth. However, one main ingredient is missing. What is the force exerted by one grain on another? In DEM, this contact force is modeled as explained below.

2.2 DEM contact force model

In recent years, the model originally developed by Cundall and Strack for spheres has been extended to non-spherical particles. In [Pournin et al., 2005], Pournin et al. extend DEM to spherocylinders. In [Pournin, 2005] and [Pournin and Liebling, 2009], Pournin et al. extend the DEM contact model to spheropolyhedra. We give here a description of this model.

A spheropolyhedron is the Minkowski sum of a polyhedron and a ball. Let $P(s, r)$ be the spheropolyhedron, that is the Minkowski sum of the polyhedron s and the ball $B(0, r) = \{x \in \mathbb{R}^2 : \|x\| \leq r\}$. We say s is the skeleton of P and r its radius. If s is reduced to a point, then P is a sphere of radius r , if s is a line segment then P is a spherocylinder, if s is a triangle then P is a spherotriangle, etc. (see Fig. 2.2). Note that for a given skeleton, the smaller r , the more P will resemble the original polytope with its sharp edges and corners, whereas for growing r , P will become smoother and smoother and less and less distinguishable from a ball.

Here is how the contact between two spheropolyhedral grains is modeled by Pournin et al.

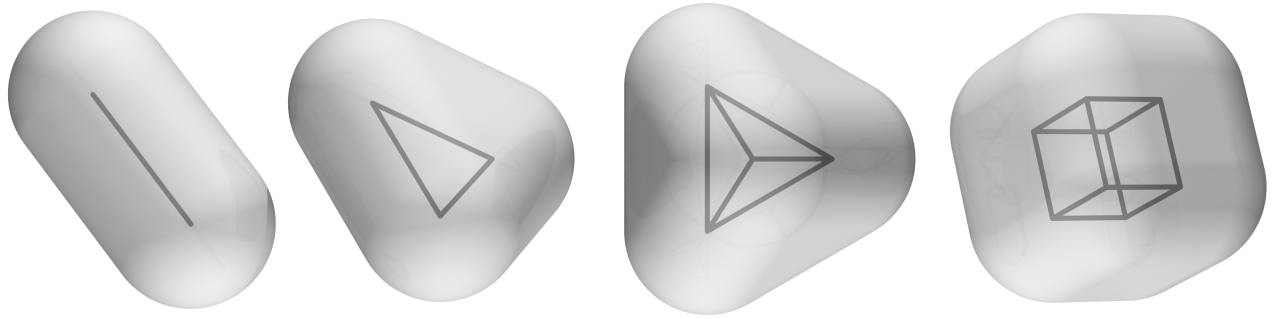


Figure 2.2: From left to right, a spherocylinder, a spherotriangle, a spherotetrahedron, and a spherocube. The skeletons of those spheropolyhedra are represented as solid lines.

2.2.1 Contact force model

Two grains $P(s_P, r_P)$ and $Q(s_Q, r_Q)$ are in contact whenever they overlap, that is if $P \cap Q \neq \emptyset$, see Fig. 2.3.

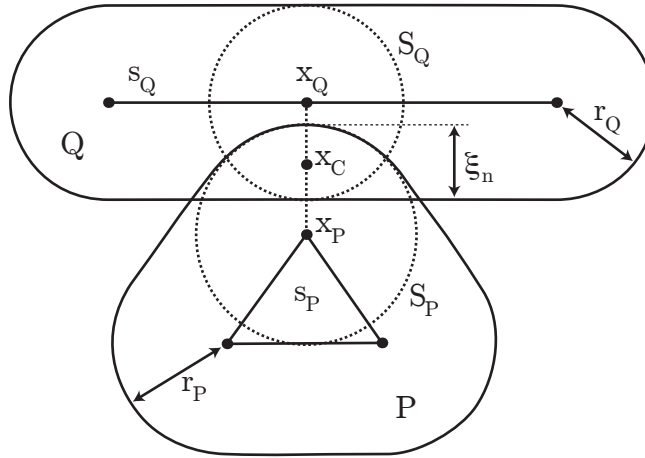


Figure 2.3: Scheme of the contact model between two spheropolyhedral grains

When this is true, the contact force is modeled as follows.

\vec{x}_P and \vec{x}_Q are defined as the barycenters of sets $m_P = \{\vec{y}_P \in s_P : d(\vec{y}_P, s_Q) = d(s_P, s_Q)\}$ and $m_Q = \{\vec{y}_Q \in s_Q : d(\vec{y}_Q, s_P) = d(s_Q, s_P)\}$ respectively. Let

$$\vec{u}_n = \frac{\vec{x}_Q - \vec{x}_P}{\|\vec{x}_Q - \vec{x}_P\|}.$$

Call Π the plane containing the intersection of the sphere of center \vec{x}_P and radius r_P and the sphere of center \vec{x}_Q and radius r_Q . Let \vec{x}_C be the intersection of Π and segment joining \vec{x}_P and \vec{x}_Q .

$$\vec{v}_r = \dot{\vec{x}}_{C/Q} - \dot{\vec{x}}_{C/P}$$

is defined as the velocity of point \vec{x}_C on Q relative to the velocity of point \vec{x}_C on P .

The overlap is defined by $\vec{\xi} = -\vec{v}_r$ and $\vec{\xi} = 0$ when the contact begins. The normal and tangential overlaps are defined as $\xi_n = \vec{\xi} \cdot \vec{u}_n$ and $\xi_t = \vec{\xi} - \xi_n \vec{u}_n$.

The contact force is modeled by

$$\vec{f} = \phi_n(\xi_n, \dot{\xi}_n) \vec{u}_n + \vec{\phi}_t^C(\vec{\xi}_t, \dot{\vec{\xi}}_t), \quad (2.5)$$

Coulomb friction μ is taken into account such as

$$\vec{\phi}_t^C(\vec{\xi}_t, \dot{\vec{\xi}}_t) = \min(\mu \phi_n(\xi_n, \dot{\xi}_n), \|\vec{\phi}_t(\vec{\xi}_t, \dot{\vec{\xi}}_t)\|) \vec{u}_t, \quad (2.6)$$

where

$$\vec{u}_t = \begin{cases} \frac{\vec{\phi}_t(\vec{\xi}_t, \dot{\vec{\xi}}_t)}{\|\vec{\phi}_t(\vec{\xi}_t, \dot{\vec{\xi}}_t)\|} & \text{if } \vec{\phi}_t(\vec{\xi}_t, \dot{\vec{\xi}}_t) \neq \vec{0} \\ \vec{0} & \text{if } \vec{\phi}_t(\vec{\xi}_t, \dot{\vec{\xi}}_t) = \vec{0} \end{cases}. \quad (2.7)$$

The two most commonly used force models are the viscoelastic force model and the Walton force model [Walton and Braun, 1986]. The former, proposed by Cundall and Strack acts like a combination of a spring and a dashpot (see [Cundall and Strack, 1979]). The contact force is a combination of elastic and viscous terms. Energy is dissipated by the viscous term. The linear expression of the force is:

$$\phi_n(\xi_n, \dot{\xi}_n) = k_n \xi_n + c_n \dot{\xi}_n \quad (2.8)$$

$$\vec{\phi}_t(\vec{\xi}_t, \dot{\vec{\xi}}_t) = k_t \vec{\xi}_t + c_t \dot{\vec{\xi}}_t. \quad (2.9)$$

Non-linear versions have been investigated [Kuwabara and Kono, 1987].

2.2.2 Tuning DEM with real experiments

The coefficients k_n , c_n , k_t , and c_t of the viscoelastic model are parameters that can be tuned so that the predicted behavior is as realistic as possible. The case is similar for the Walton force model. The reader may refer to [Pournin et al., 2002] for an explanation on how DEM can be tuned using as reference experiment, the collision of two grains with no initial spin. In this experiment, three measurable quantities, the duration of the contact t_c and the normal and tangential restitution coefficients

$$\begin{cases} e_n = -\dot{\xi}_n^f / \dot{\xi}_n^i \\ e_t = -\|\dot{\vec{\xi}}_t^f\| / \|\dot{\vec{\xi}}_t^i\| \end{cases} \quad (2.10)$$

where i and f denote the quantities before and after the collision, are used to determine force model coefficients.

2.3 Implementation details

2.3.1 Numerical integration of the motion laws

In DEM, the movement of the grains is found by numerical integration of the motion laws for a solid given by equations (2.2) and (2.3). In the DEM codes used for this thesis the forward Euler method and a fixed time step are used for numerical integration. As is usual, the smaller the time step, the more the resolution of the equations of movement will be precise. However, in counterpart, the smaller the time step, the longer the simulation will take. The time step must be chosen smaller than the contact time t_c defined in 2.2.2.

2.3.2 Detection of contacts

The detection of contacts has two underlying problems. One is, given the position of the two grains, to decide whether they are in contact or not. The other is to find ways to limit the number of pairs of grains to be tested for contact.

2.3.2.1 Detection of all contacts

The most straightforward way to find all pairs of grains that are in contact is to test each pair. It is possible, however, to accelerate contact detection by maintaining lists of neighboring grains for each grain. The advantage being that only grains that are neighbors can be in contact. One neighborhood technique is grid subdivisions. The simulation area is divided into cells and track is kept of the grains in each cell. This allows to check for contacts between grains in the same or adjacent cells. For populations of multiple sized grains, adaptive subdivisions like quadtrees of the simulation area can be used. Müller [Müller, 1996] proposed to use weighted Delaunay triangulations to keep track of neighbor grains in two dimensions. The Delaunay triangulation constructed on the centers of a set of disc-shaped grains and weighted by the squares of the radii of the discs has the property that two discs that are in contact are joined by an edge of the triangulation. This allows the average complexity of contact detection to be reduced from quadratic to linear with a slight overhead for the maintenance of the triangulation. This effective method was generalized to three dimensions by Ferrez [Ferrez and Liebling, 2002]. It was further generalized to spheropolyhedra by Pournin et al. [Pournin et al., 2005; Pournin, 2005; Pournin and Liebling, 2009]. The idea is to cover the spheropolyhedra with spheres, then the weighted Delaunay triangulation is constructed on the covering spheres, and two spheropolyhedra are in contact only if spheres of their coverings are in contact. This happens only if some of the covering spheres are joined by an edge in the weighted Delaunay triangulation. These methods allow to find quickly potential contacts, however one must still verify if such a potential contact is really a contact. We will see how in the next section.

2.3.2.2 Detection of the contact between two grains

The method used to determine whether two grains are in contact depends on the shape of the grains. We give here a method to determine if two spherocylinders intersect.

Let $P(s_P, r_P)$ and $Q(s_Q, r_Q)$ be two spherocylinders, i.e. two spheropolyhedra whose skeletons are segments.

$$P \cap Q \neq \emptyset \text{ iff } d(s_P, s_Q) \leq r_P + r_Q,$$

where $d(s_P, s_Q) = \inf\{\|x_P - x_Q\|, x_P \in s_P, x_Q \in s_Q\}$.

The main problem is to calculate $d(s_P, s_Q)$ the distance between two segments.

Let us write $s_P = \{\vec{x}_1 + s\vec{a}_1 | s \in [-l_1/2, l_1/2]\}$ and $s_Q = \{\vec{x}_2 + t\vec{a}_2 | t \in [-l_2/2, l_2/2]\}$ where \vec{a}_1 and \vec{a}_2 are unitary vectors.

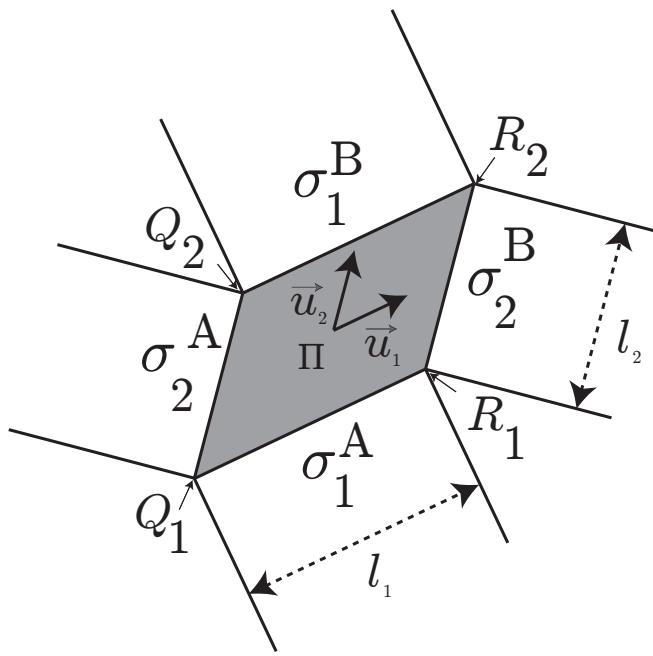
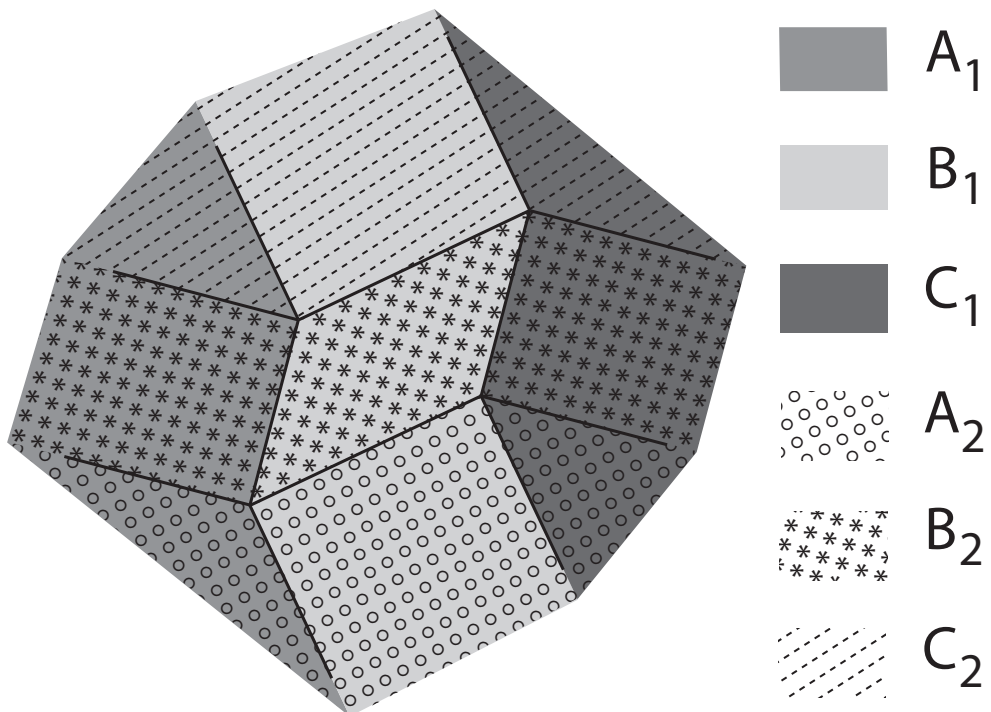
$$(\bar{s}, \bar{t}) = \operatorname{argmin}\{\|\vec{x}_1 + s\vec{a}_1 - \vec{x}_2 - t\vec{a}_2\|^2, (s, t) \in [-l_1/2, l_1/2] \times [-l_2/2, l_2/2]\} \quad (2.11)$$

are the values of s and t that give the closest points on s_P and s_Q .

We notice that the problem is to find the point on the parallelogram $\{s\vec{a}_1 - t\vec{a}_2 | (s, t) \in [-l_1/2, l_1/2] \times [-l_2/2, l_2/2]\}$ closest to $\vec{x}_1 - \vec{x}_2$. To solve this problem, we propose the following algorithm. Lumelsky [Lumelsky, 1985] proposes the same algorithm with another proof. Other ways of finding the closest points on two segments exist [Vega and Lago, 1994].

Algorithm for finding the point of a parallelogram Π closest to a point P in 3D

- Input: parallelogram $\Pi = \{s\vec{u}_1 + t\vec{u}_2 | (s, t) \in [-l_1/2, l_1/2] \times [-l_2/2, l_2/2]\}$, where \vec{u}_1 and \vec{u}_2 are unitary, and point P having coordinates $\vec{x} = (x, y, z)$
- Output: the point of Π the closest to point P
 - Step 1: Calculate \bar{s} , the first coordinate of P in the basis $\{\vec{u}_1, \vec{u}_2, \vec{u}_1 \wedge \vec{u}_2\}$
 - * If $\bar{s} \in [-l_1/2, l_1/2]$, $s' = \bar{s}$
 - * If $\bar{s} < -l_1/2$, $s' = -l_1/2$
 - * If $\bar{s} > l_1/2$, $s' = l_1/2$
 - Step 2: $\bar{t} = (\vec{x} - s'\vec{u}_1) \cdot \vec{u}_2$
 - * If $\bar{t} \in [-l_2/2, l_2/2]$, STOP $s'\vec{u}_1 + \bar{t}\vec{u}_2$ is the point of Π the closest to point P
 - * If $\bar{t} < -l_2/2$, $t' = -l_2/2$
 - * If $\bar{t} > l_2/2$, $t' = l_2/2$
 - Step 3: Find $s'' = (\vec{x} - t'\vec{u}_2) \cdot \vec{u}_1$
 - * If $s'' \in [-l_1/2, l_1/2]$, $s''' = s''$
 - * If $s'' < -l_1/2$, $s''' = -l_1/2$

Figure 2.4: Parallelogram Π represented in the plane containing Π Figure 2.5: Separation of the plane containing Π into regions (1st figure)

- * If $s'' > l_1/2$, $s''' = l_1/2$
- * STOP $s''' \vec{u}_1 + t' \vec{u}_2$ is the point of Π the closest to P

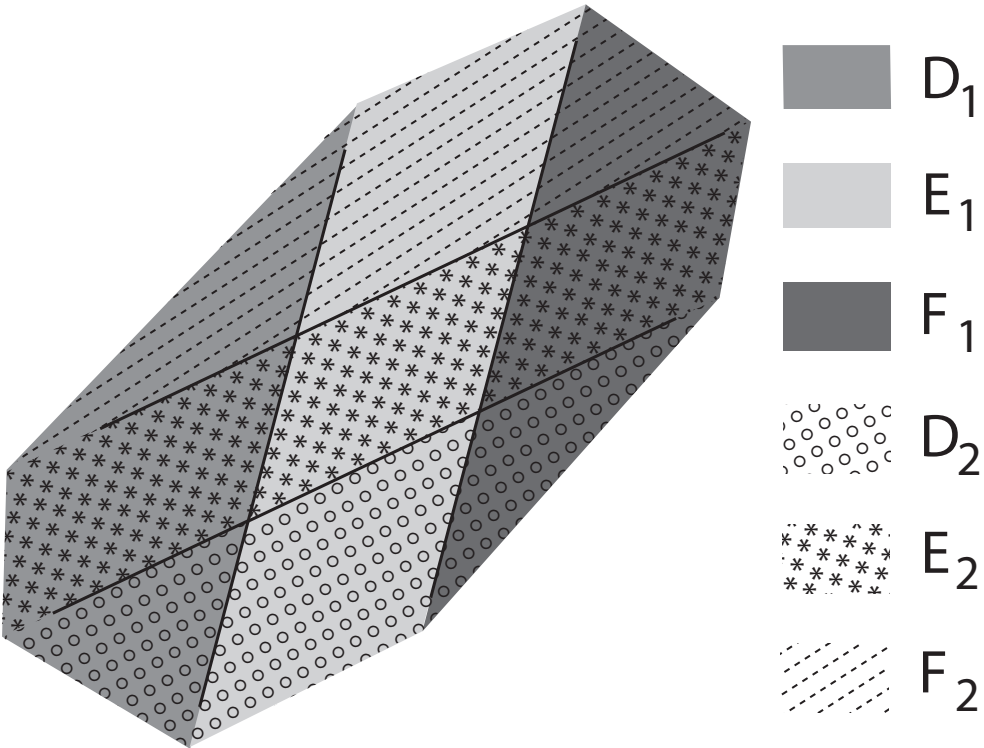


Figure 2.6: Separation of the plane containing Π into regions (2nd figure)

Justification of the algorithm

Consider figures 2.4 and 2.5. Let us write $\psi(P, S)$ the point of a convex set S closest to P and P' the point of Π closest to P . We accept the following lemma without proof:

Lemma 1

$P \in A_1 \cap A_2 \Rightarrow P' = Q_1$	$P \in A_1 \cap B_2 \Rightarrow P' = \psi(P, \sigma_2^A)$	$P \in A_1 \cap C_2 \Rightarrow P' = Q_2$
$P \in B_1 \cap A_2 \Rightarrow P' = \psi(P, \sigma_1^A)$	$P \in B_1 \cap B_2 \Rightarrow P' = P$	$P \in B_1 \cap C_2 \Rightarrow P' = \psi(P, \sigma_1^B)$
$P \in C_1 \cap A_2 \Rightarrow P' = R_1$	$P \in C_1 \cap B_2 \Rightarrow P' = \psi(P, \sigma_2^B)$	$P \in C_1 \cap C_2 \Rightarrow P' = R_2$

We now show that the algorithm gives the correct answer for any instance of the input when P is in the plane containing Π . The general case can be shown similarly by projecting P on this plane. Notations are as in figures 2.4, 2.5 and 2.6 .

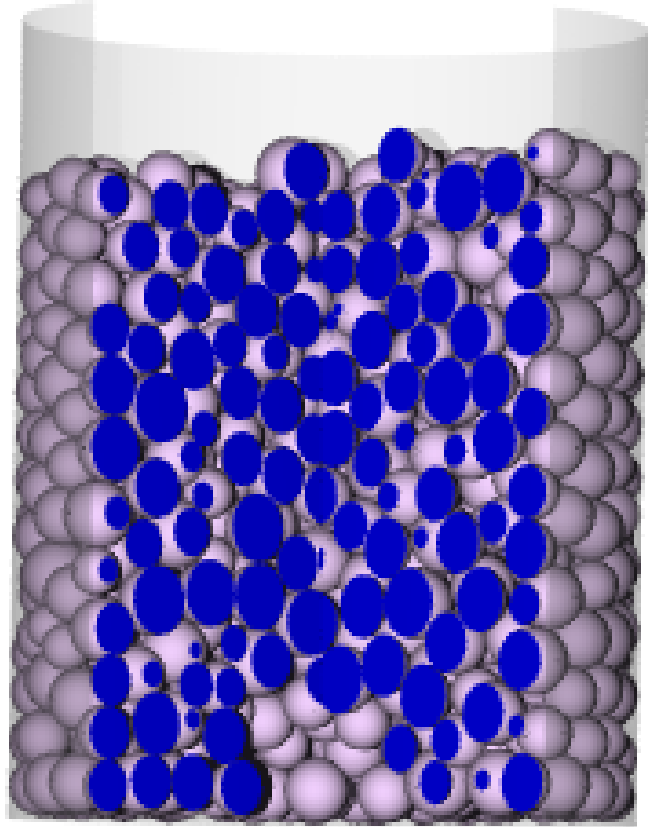
Consider the 3 following cases:

- Suppose that at step 1 of the algorithm $\bar{s} \in [-l_1/2, l_1/2]$, then $P \in E_1$.

Consider the 3 following cases:

- Suppose at step 2, $\bar{t} \in [-l_2/2, l_2/2]$, then $P \in E_1 \cap E_2$. According to lemma 1, $P' = P$. The algorithm returns $s'\vec{u}_1 + \bar{t}\vec{u}_2$ which is also equal to P . The answer is correct in this case.

- Suppose at step 2, $\bar{t} < -l_2/2$, then $P \in E_1 \cap A_2 \subset A_2$. According to lemma 1, $P' = \psi(P, \sigma_1^A)$. The algorithm goes on to step 3 and returns $s''' \vec{u}_1 + t' \vec{u}_2$ which is also equal to $\psi(P, \sigma_1^A)$. The answer is correct in this case.
- Suppose at step 2, $\bar{t} > l_2/2$, a similar argument to the one used when $\bar{s} \in [-l_1/2, l_1/2]$ and $\bar{t} < -l_2/2$ shows that the answer is correct in this case.
- Suppose that at step 1 of the algorithm $\bar{s} < -l_1/2$, then $P \in D_1$. Consider the 3 following cases:
 - Suppose at step 2, $\bar{t} \in [-l_2/2, l_2/2]$, then $P \in D_1 \cap B_2$. According to lemma 1, $P' = \psi(P, \sigma_2^A)$. The algorithm returns $s' \vec{u}_1 + \bar{t} \vec{u}_2$ which is also equal to $\psi(P, \sigma_2^A)$. The answer is correct in this case.
 - Suppose at step 2, $\bar{t} < -l_2/2$, then $P \in D_1 \cap A_2 \subset A_2$. According to lemma 1, $P' = \psi(P, \sigma_1^A)$. The algorithm goes on to step 3 and returns $s''' \vec{u}_1 + t' \vec{u}_2$ which is also equal to $\psi(P, \sigma_1^A)$. The answer is correct in this case.
 - Suppose at step 2, $\bar{t} > l_2/2$, a similar argument to the one used when $\bar{s} < -l_1/2$ and $\bar{t} < -l_2/2$ shows that the answer is correct in this case.
- Suppose that at step 1 of the algorithm $\bar{s} > l_1/2$, similar arguments to the ones used when $\bar{s} < -l_1/2$ show that the answer is correct in this case.



Part II

Fine-scale modeling

Clouds are not spheres, mountains are not cones, coastlines are not circles and bark is not smooth nor does lightning travel in a straight line.
– Benoît Mandelbrot

Chapter 3

Synchrotron tomography of jamming experiments

3.1 Introduction

The material in the two following chapters has been published in [Tsukahara et al., 2008].

Until recently, it was difficult to observe what was going on inside granular media. At best, it was possible to observe 2D experiments through transparent walls or disassemble 3D experiments [Bernal, 1959; Bernal and Mason, 1960; Scott, 1960; Finney, 1970]. With the advent of 3D tomography, inside observation of granular media became possible.

In this chapter we will present results on the X-ray synchrotron tomography of jamming experiments. In these experiments, a cylindrical receptacle is filled with glass beads and after settlement a circular hole is opened at the bottom. Tomographs of the media are taken before opening the hole and after jamming. We present the effective computerized strategy we used to extract the positions and radii of the beads. The experiments were carried out by Slobodan Mitrovic and Vincent Gajdosik of the Laboratory of Physics of X-Rays at the EPFL. The analysis of the tomographs was carried out by the author.

Tomography was invented by radiologist Alessandro Vallebona in the 1930's. The main idea behind it is to measure a physical quantity in an object through projections. Different physical phenomena such as X-rays, gamma rays, electrons are used for this purpose. The measurements must then be combined to extract an image of inside the object, using tools such as the Radon transform. Since the number of measurements can be very large, it is with the development of computers and image reconstruction software that tomography really became feasible. The first commercial computed tomography scanner (a type of tomography using X-rays) was built at the end of the 1960's by Sir Godfrey Hounsfield at EMI Central Research Laboratories. Many different types of tomography exist today and while it was first used for medical purposes, the technique is now used in many domains such as archaeology, biology or geology.

In recent years, 3D imaging was used to investigate the geometrical properties of void space for a better insight into the flow properties of fluids in a material [Spanne et al., 1994; Baldwin et al., 1996; Lindquist et al., 1996; Sederman et al., 2001; Al-Raoush and Willson, 2005], granular media packing [Seidler et al., 2000; Richard et al., 2003; Aste et al., 2004; Saadatfar et al., 2005; Fu et al., 2006] or foam structure [Lambert et al., 2005]. Seidler et al. [Seidler et al., 2000] identified the central positions and local connectivity of 2,000 monodisperse glass spheres from X-ray microtomography data using edge location and the Hough transform. Richard et al. [Richard et al., 2003] found the size and location of 15,000 glass beads by X-ray microtomography while analyzing granular systems undergoing compaction. Aste et al. [Aste et al., 2004] analyzed two 150,000-beads samples and four 35,000-beads samples by X-ray computed tomography and a convolution method. Fu et al. [Fu et al., 2006] investigated 2,000 particles using X-ray microtomography and a watershed-based segmentation algorithm and showed that packing systems generated by DEM are consistent with the structural measurements made by X-ray microtomography. Despite these significant advances, extracting efficiently from tomographic images the microscopic geometric information such as the sizes of voids or the grain radii and positions still constitutes a challenge.

3.2 The experiment

Edge-enhanced X-ray micro-tomography using broadband synchrotron radiation is a powerful nondestructive tool for research on packing and jamming in granular systems. Standard absorption tomography is based on the 3D determination of the linear attenuation coefficient and is related only to the imaginary part of the complex refraction index. Thanks to the high spatial coherence of the synchrotron X-rays we can use effects based on the real part of refraction index to enhance the edge visibility [Tsai et al., 2003]. In X-rays beam glass beads act as weak divergent lenses and phase effects are visible on the glass/air interface of each sphere as concentric white bands (Fig.3.1). Even with polychromatic X-ray radiation this effect contributes remarkably to absorption contrast and could be optimized by simple changing propagation (sample to detector) distance. On the contrary the air defects inside the glass enhance themselves by focusing - acting as weak convergent lenses.

All tomography experiments were performed on the white-light imaging beamline BLO1A at the National Synchrotron Research Center, Hsinchu, Taiwan as described in [Baik et al., 2004]. Bending-magnet synchrotron radiations with a continuous spectrum (photon energy 5-20 keV) were used in a lensless configuration (Fig. 3.2).

After passing through the sample, the X-rays were converted to visible light by a CdWO₄ scintillating crystal. The image was then magnified with an optical microscope and captured by a CCD camera. This approach gets advantage of entire beam size and makes possible imaging millimeter-size specimens with micron lateral resolution. By adjusting the sample-detector distance for a limited edge-enhancement 3D volume, tomographic reconstruction based on a sequence of projection images taken at different angles is feasible without introducing serious artifacts. A common filtered back projection implemented in IDL (Interactive Data Language) was used for this reconstruction. Nine different experiments (Table 3.1) were conducted on

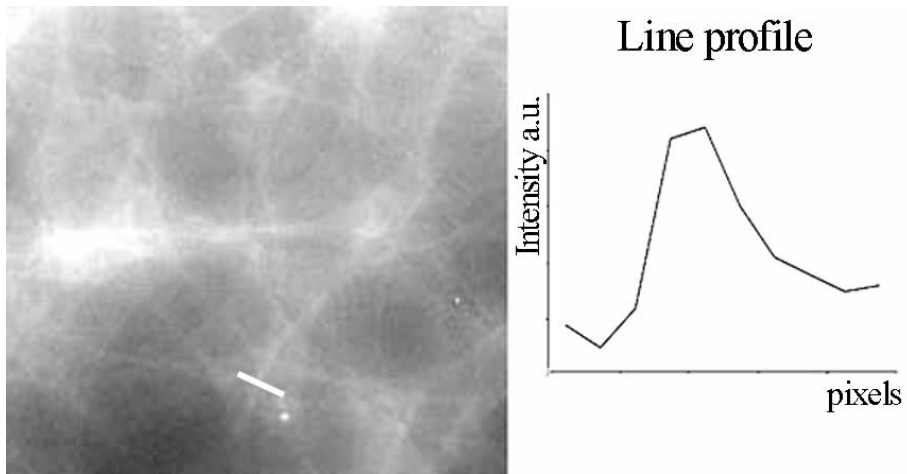


Figure 3.1: Tuning the sample-detector distance for optimal contrast enhancement in 2D projection: the line intensity profile (white mark) through the glass-air interface shows a peak of higher intensity corresponding to the refraction-based effects

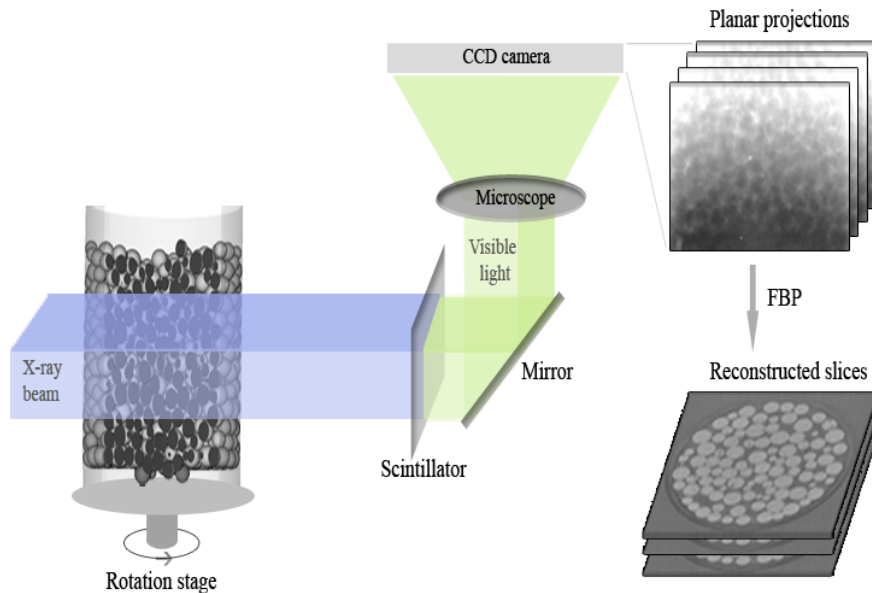


Figure 3.2: Scheme of the synchrotron microtomography imaging setup

two sets of spherical glass beads (Assistent-Precision, Germany). Set #1 contained mixed size individually selected beads avoiding aspherical shapes and other fabrication artifacts. Set #2 underwent the same procedure and was sieved, keeping only particles with radii within the range $0.2 - 0.25\text{ mm}$. For both sets, the size of the beads was not known.

A boron nitride cylindrical container was selected because of its resistance to radiation damage (Fig. 3.3). The container had two interchangeable circular openings with diameters $B = 1.5$ and 2.0 mm . The bottom of the opening was equipped with a paper sheet shutter which was positioned under an interchangeable bottom piece in offset $C = 1.0\text{ mm}$ to the receptacle bottom.

Table 3.1: Description of the experimental setup. Exp: Experiment label (first number indicates if hole radius is ~ 3 or 4 times the average bead radius, letter b indicates sieved bead experiments, second number indicates experiment number), BS: Bead sizes (1: mixed; 2: sieved), $\langle r \rangle$: Average radius, SD: Standard deviation, HR: Hole radius

Exp	BS	$\langle r \rangle [\mu m]$	SD [μm]	HR [mm]
3_1	1	275	27	0.75
3_2	1	275	27	0.75
3_3	1	275	27	0.75
4_5	1	275	27	1.0
3b_1	2	230	16	0.75
3b_3	2	230	16	0.75
4b_1	2	230	16	1.0
4b_2	2	230	16	1.0
4b_3	2	230	16	1.0

Projection images were first taken with the bottom aperture closed to obtain the initial conditions for DEM simulations. Then the shutter was opened letting the beads flow. A second projection image set was acquired after the bead flow jammed and an arch was formed. All tomography sets were obtained for three adjacent vertical positions and merged to cover a volume that contained around 1000 particles for set #1 and 2000 particles for set #2.

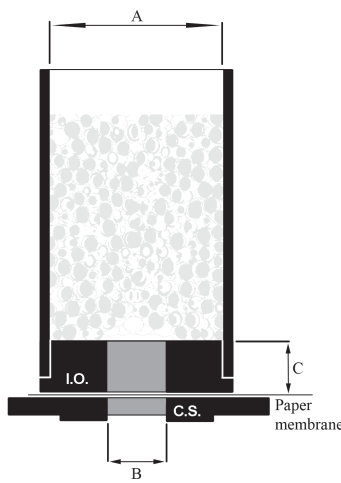


Figure 3.3: The container (diameter A = 6.0 mm) was drilled from one block of Boron Nitride and has interchangeable openings - I.O (diameter B = 1.5 mm and 2.0 mm). A paper shutter was positioned under the container in offset C = 1.0mm from its bottom. The container was mounted on the top of a metal sample holder- C.S

3.3 Image analysis

3.3.1 The processing procedure

We now describe our procedure to obtain the positions and radii of the various observed particles from the raw tomography images. The raw tomograph (Fig. 3.4a) had 1,599 pixels in the x and y horizontal directions and approximately 1,985 pixels in the z direction, occupying nearly 5 GB of computer memory. Each pixel corresponds to a cube size $4 \times 4 \times 4 \mu\text{m}^3$. Hence, the field of view is of size $6.396 \times 6.396 \times 7.94 \text{ mm}^3$. The large amount of data is one of the complicating factors of the image analysis along with other problems such as

1. low contrast: the void (air) and the glass beads have similar X-ray absorption factors, on a scale of 256 grey tones, the average void grey is 145 while that of the beads is 160
2. noise: the CNR (Contrast-to-Noise Ratio) is typically 0.56 dB, thus very poor
3. Newton rings (Fig. 3.4b)
4. splashes (Fig. 3.4c)
5. air bubbles in the beads (Fig. 3.4e)
6. non uniformity of the intensity along the z-axis.

Furthermore, in spite of our efforts to select spherical beads, some non-spherical particles were still present (Fig. 3.4d). Our objective here was to obtain accurate estimates of the positions and radii of all observed beads. Since standard image-analysis software cannot treat beads in the above problematic conditions, we had to develop our own procedure with algorithms and the corresponding software, as described below.

The main processing steps are: pre-processing of the raw images, preliminary detection of spheres that fit the beads (sphere-fittings) using 3D watershed and third, optimization of the preliminary sphere-fittings. A multi-resolution approach was chosen, i.e. the size of the images was varied so that the computer could handle the memory requirements of the different processes.

The pre-processing consisted in smoothing the images to reduce the noise and in applying an adaptative thresholding procedure along the z-layers (Fig. 3.5a). The threshold value was independently computed for every layer to compensate the non-uniformities along the z-axis. However, this treatment was not sufficient to free the images of the traces of Newton rings and air bubbles – and manual corrections as well as image processing morphological operations (dilation, erosion) were applied to further clean the images of artifacts (Fig. 3.5b). This pre-processing was applied to the original images reduced by 50% in x,y and z directions.

The detection step consisted in segmenting the binary volume data set into regions and then fitting spheres to the found regions. Watershed by immersion was used for this segmentation. This algorithm introduced for 2D images by Vincent and Soille [Vincent and Soille, 1991] has been

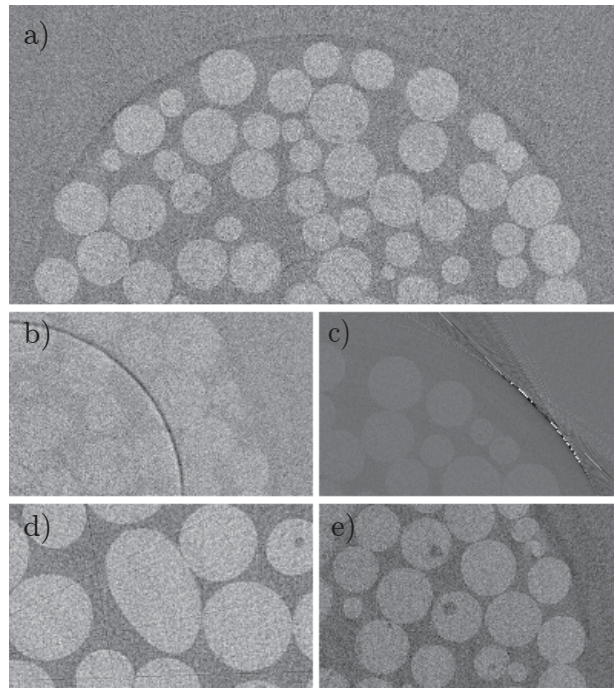


Figure 3.4: Raw tomograph (and artefacts) used as input for image analysis: a) Half of a horizontal cut (z-layer) b) Newton ring c) Splashes d) Asphericity e) Air bubbles

employed in various domains including powder and granular matter [Al-Thyabat and Miles, 2006; Fu et al., 2006]. Here, we have developed and implemented its extension to the 3D case. Specifically, we first created a distance map transform (Fig. 3.5c) of the binary volume by applying successive erosions. The result of the distance map transform is an image where the gray-level is the distance from the closest boundary pixel. We then applied the immersion algorithm to obtain regions as shown in Fig. 3.5d.

The result of the watershed segmentation was good for a large portion of the spheres. However, segmentation by the watershed algorithm is affected by three types of errors: (1) two or more regions can be found for only one bead (over-segmentation); (2) one region can be found for two or more beads (under-segmentation); (3) the boundary between two beads is badly estimated (bad-cut). The first error can be corrected algorithmically since the regions of an over-segmentation interpenetrate each other so that the corresponding sphere-fittings have large overlaps. It is thus possible to merge the sphere-fittings so that the final sphere is a correct estimation of the bead.

Correcting for under-segmentation and bad-cut errors is much trickier and we therefore resorted to manually editing these. For the computer processing of the other beads, the sphere-fitting radius was defined as the radius of a sphere with the same volume as the watershed region of the bead. The sphere-fitting position was defined as the average location of pixels in that region.

The watershed algorithm being demanding as far as computer memory is concerned, the detection stage was applied to images reduced in size by 75% with respect to the original images in the x, y and z directions. This causes a certain loss of information: it was indeed necessary to return to 50% reduced images for more precise sphere-fitting. To achieve this, starting from the sphere-fitting found in the detection stage and the 50% reduced binary images obtained after pre-processing, an optimization program was implemented. We looked for the largest sphere contained in the bead. Since the beads are not far from being spherical this is reasonable. The

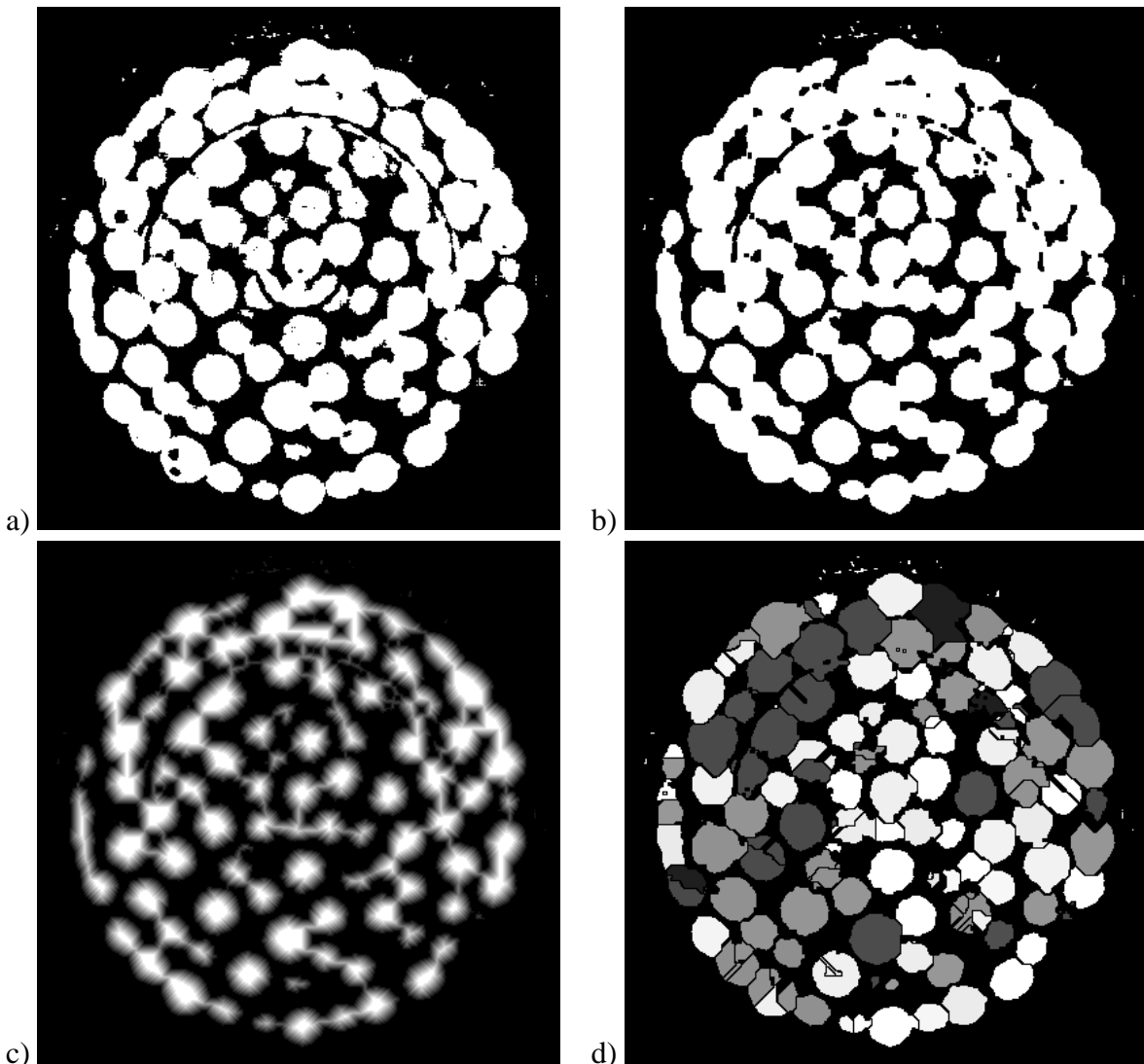


Figure 3.5: a) Z-layer after thresholding b) Z-layer after cleaning of artifacts c) Distance map of Z-layer d) Z-layer after watershed

optimum sphere was found by an ad-hoc gradient method. Fig.3.6 shows a comparison of sphere-fittings before and after the optimization.

3.3.2 Results and validation of the image processing procedure

We implemented the whole process as a plugin series for ImageJ [Rasband, 2006], a general purpose image-processing software (public domain licence) and ran the software on a Mac computer. 3D tomographic images corresponding to initial and final configurations were processed for seven of the nine experiments detailed in Table 3.1. For experiments 4b_1 and 4b_2, for which instant jamming did not take place, only the initial configurations were processed entirely.

Estimates for the number of beads detected by the watershed algorithm, the number of beads detected by merging sphere-fittings corresponding to over-segmentations as well as the number

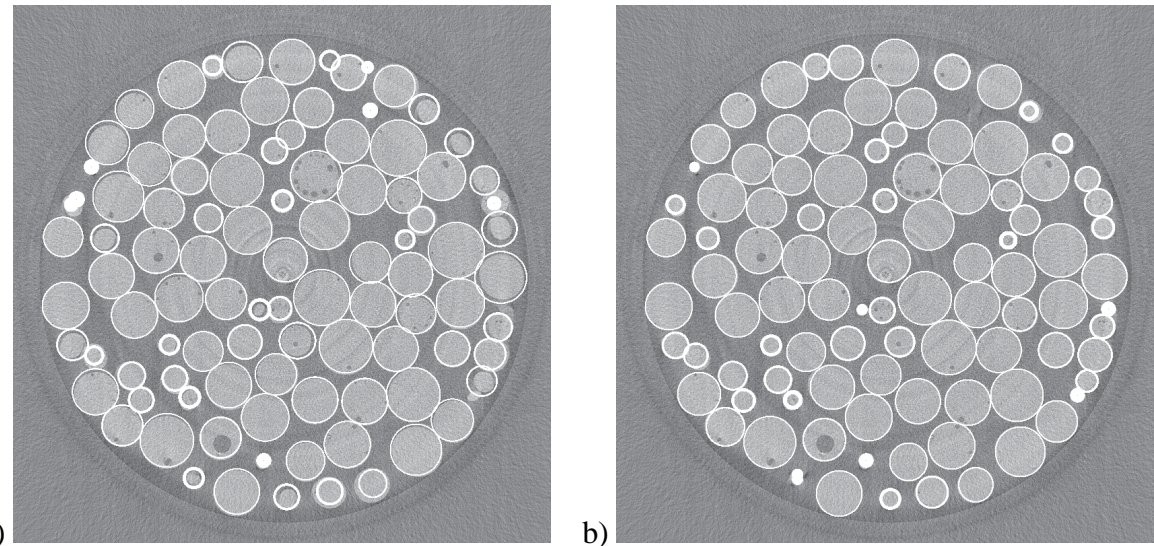


Figure 3.6: Sphere-fittings (white circles) superimposed to the original tomographs after: a) detection b) optimization

of beads detected by the user were calculated (Fig. 3.7). 98.5% of the beads were detected by our procedure and the remaining 1.5% were estimated only by manual detection. After user correction 100% of the beads in the field of view were detected for all 3D images treated.

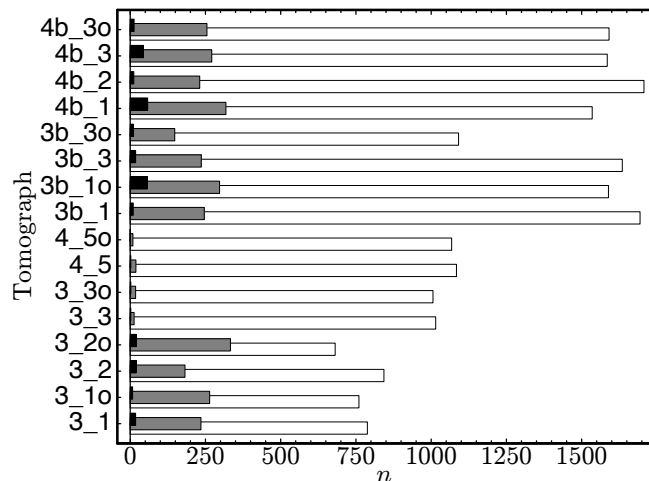


Figure 3.7: Results of the detection: n , number of beads; white, correct detection; gray, automatically corrected for over-segmentation; black, corrected manually for under-segmentation and bad cuts. Letter o indicates an image taken after the hole has been opened.

The total time needed to treat one 3D tomography image was approximately 20 hours, of which 25% corresponds to user work and the other 75% to computer calculations.

To estimate how precise the final sphere-fittings (after optimization) are, a 3D binary rendition of the sphere-fittings was created. This image was subtracted from the binary image obtained after pre-processing. The symmetric difference (Fig. 3.8) between these two images is an approximate measure of the total volume discrepancy between the beads and their sphere-fittings.

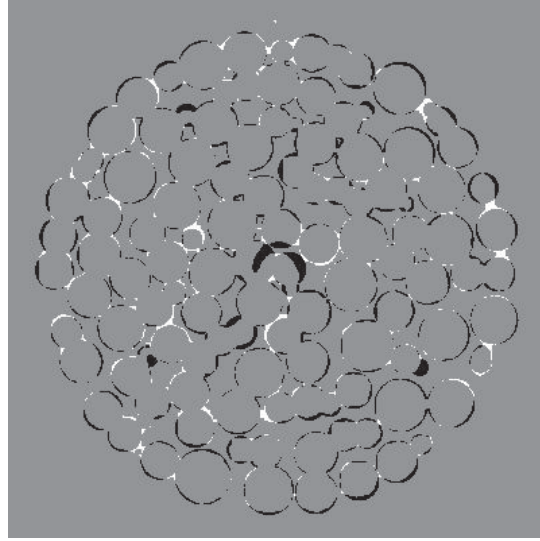


Figure 3.8: Error estimation: symmetric difference of fitted spheres and preprocessed image (white shapes, particles in the preprocessed image absent in the sphere-fittings; black shapes, opposite case)

Dividing this measure of discrepancy by the number of beads gives an approximate average for the volumic error, $\langle \Delta V \rangle$, affecting a bead sphere-fitting. The corresponding results for different tomographs are reported in Fig. 3.9a. The average bead volume is around $7 \times 10^7 \mu\text{m}^3$, thus the volumic error affecting a bead is found between 15% and 20% of the average bead volume.

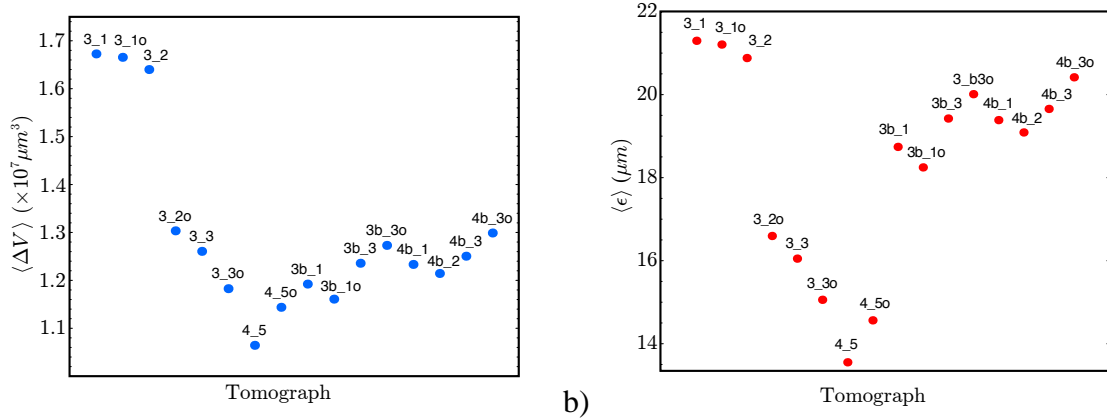


Figure 3.9: a) Average volumic symmetric difference between a real bead and its sphere-fitting b) Average fitting error on positions and radii

It is interesting, assuming that the real beads are spherical, to evaluate the error made while estimating their radii and positions. For an approximate assessment, we can assume that the real beads are spherical and that, as a starting point, there is no error for the positions. Then the volumic discrepancy is

$$\Delta V = \left| \frac{4}{3}\pi r_{SF}^3 - \frac{4}{3}\pi r_B^3 \right| \quad (3.1)$$

where r_{SF} and r_B are respectively the radii of the sphere-fitting and the real bead.

When r_{SF} and r_B are close, the right-hand side of (3.1) is close to $4\pi|r_{SF} - r_B|r_{SF}r_B$ so that

$$|r_{SF} - r_B| \simeq \frac{1}{4\pi r_{SF} r_B} \Delta V. \quad (3.2)$$

Taking r_{SF} and r_B equal to the average bead radius, r_a ($\simeq 250\mu m$), on the right-hand side of (3.2), the average error made on the bead radii can be estimated by $\langle \epsilon \rangle = \frac{1}{4\pi r_a^2} \Delta V$. We found that the error on the distance between the centers of real beads and their sphere-fittings can also be roughly estimated as $\langle \epsilon \rangle = \frac{1}{4\pi r_a^2} \Delta V$. Values for this approximate average error measure are shown in Fig. 3.9b. It shows that the average error on the positions and the radii is found in between 5% and 10% of the average radius.

It is important to note that in this error estimation the final sphere-fittings were compared to the images of the beads as found on the pre-processed images. The pre-processed images do not give an image of the real beads as correct as the original images do. Thus the error estimation given here is probably an over-estimation of the real sphere-fitting error.

3.3.3 Reconstructing the exact shape and position of the container

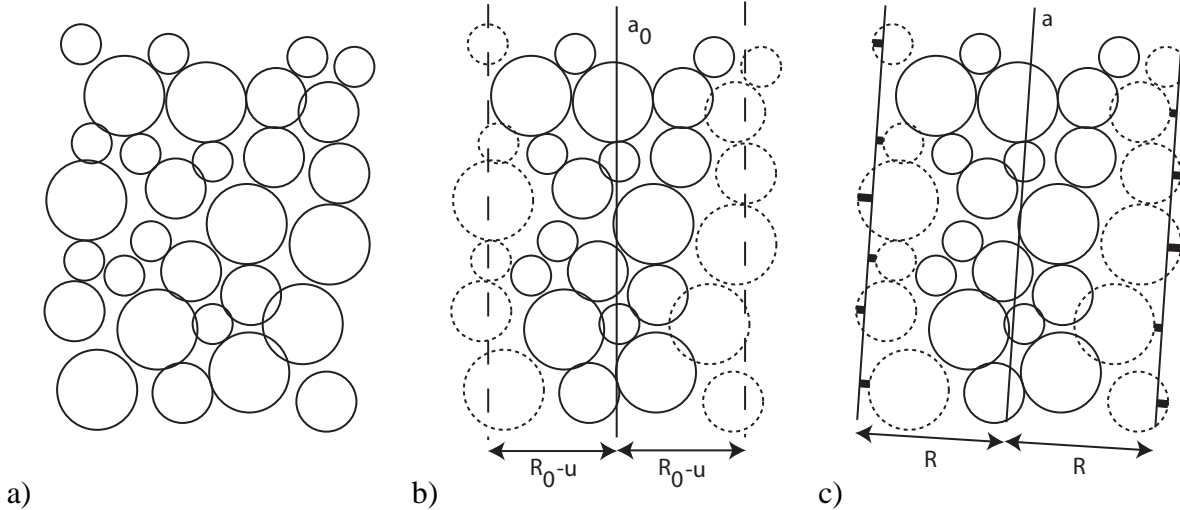


Figure 3.10: Two-dimensional illustration of the method for finding cylinder axis and radius: a) Sphere-fittings b) Finding the beads (in dashed lines) that were probably touching the cylinder c) Estimations, a and R , of the real cylinder's axis and radius found by minimizing the squares of the lengths showed in thick lines

Due to manipulations between experiments the cylinder position varied and the bottom moved with respect to the cylinder. Also, the cylinder was not available at the time of the reconstruction for measurements. As a consequence, to simulate as realistically as possible the experiments, the axis and radius of the cylinder and the position of receptacle bottom had to be estimated. For this, the cylinder and its position were set to be the solution to an optimization problem. To limit the calculations, we found the beads that were most probably touching the cylinder in

the real experiments. This was done by starting with rough estimations, a_0 and R_0 , of cylinder axis and radius, choosing a small $u > 0$ and detecting spheres $E = \{S_1, \dots, S_n\}$ that are outside of the cylinder of axis a_0 and radius $R_0 - u$ (Fig. 3.10b). For each sphere S_i , we call its center c_i and its radius r_i . We solved the following optimization problem:

$$\begin{aligned} \text{minimize} \quad & \sum_{S_i \in E} \xi_i^2 \\ \text{under constraints} \quad & \xi_i = d(c_i, a) + r_i - R \\ & R \in \mathbb{R}_+^* \\ & a \text{ line in } \mathbb{R}^3 \end{aligned} \tag{3.3}$$

to find an estimations, a and R , of the real cylinder's axis and radius. In other words, we found the cylinder for which a measure of the distance between a sphere-fitting and the cylinder (given by ξ_i^2) is essentially small for all sphere-fittings ($\sum \xi_i^2$ is small), see Fig. 3.10c.

A similar procedure was applied to estimate the receptacle bottom. Mathematica optimization functions were used for these steps. The values found for the angles between cylinder axis and the tomographic images vertical direction as well the angles between the cylinder axis and the receptacle bottom normal varied between 0.1° and 1.4° . Not only did the cylinder axis-Oz angle vary but the receptacle bottom angle too. This is consistent with the fact that in the real experiment these two elements are separate pieces.

The observer, when he seems to himself to be observing a stone, is really, if physics is to be believed, observing the effects of the stone upon himself.
– Bertrand Russell

Chapter 4

Experimental validation of 3D DEM

4.1 Introduction

The main question behind this part of this thesis is the following. How good is DEM and its fine-scale modeling in predicting the outcome of real experiments with granular media? We will study this question by putting DEM to the test. Our strategy here is to use the initial data (fitted spheres along with the estimated cylindric receptacle) corresponding to the hourglass experiments described in chapter 3 as the starting point of DEM simulations. A preliminary DEM run starting from this situation is carried out to allow the system to settle before opening the shutter. Appropriate DEM model parameters are found by trial and error, as will be explained. Once equilibrium is reached, a second DEM with the opened shutter is run and the final situation is compared to the corresponding fitted final images from the physical experiment. How realistic is this coupled Tomo-DEM technique? Can it reproduce the jamming and how closely can it predict the measured final configurations of the experiments? The objective of this study was to address these important questions.

4.2 Numerical Hourglass Experiment Simulations with DEM

4.2.1 Procedure

In the first place, the DEM parameters had to be set to suit the needs of our simulation. The main parameters are the normal and tangential restitution coefficients, normal and tangential contact times, Coulomb friction coefficient and simulation time step (see Chapter 2). The present study was performed with glass beads for which the Coulomb friction coefficient is about 0.95. Furthermore, a realistic value for the restitution coefficient is approximately 0.96 and for the contact time a realistic value would be about $1\mu s$. However, for simulation coherence, the simulation time step must be smaller than the contact time. Since small time steps like $1\mu s$ lead to

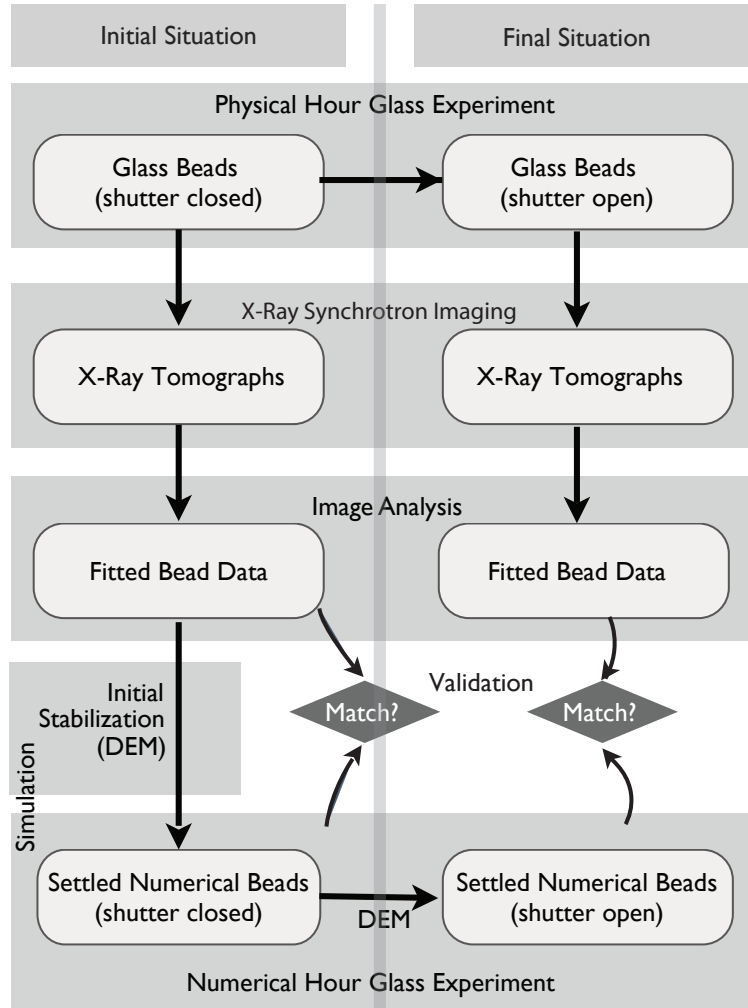


Figure 4.1: Combining synchrotron x-ray tomography and DEM: an overview

lengthy calculation times, the used contact time could not be selected to be realistic. Another difficulty was the limited precision in bead radii and position estimates. Overlaps between beads or between beads and the receptacle caused by this lack of precision could possibly lead to unrealistic ejection at contact points. As a first step, we decided to pass over realism in the choice of individual DEM parameters in favor of a more realistic general behavior of the medium.

We used a dichotomic method on one experiment to find the restitution coefficient and contact time for which the movement of the beads in their initial rearrangement was realistically small. This procedure led to a restitution coefficient of 0.0011 and a contact time of 0.7ms. As pointed out above, these values do not correspond to realistic modeling of glass beads, and would better fit beads of a much softer material.

The experiment setup was not entirely within the field of view, beads below the level of the receptacle bottom and at the top of the setup were not estimated. As discussed in section 3.2, the hole opening in the real experiments was located not at the receptacle bottom level, but at the bottom of the smaller cylinder linked to the receptacle hole. In the simulations beads below the receptacle bottom level were immobilized during the first phase of the procedure (closed

shutter) to model the setup as realistically as possible. Opening the hole was then simulated by freeing these beads.

4.2.2 Results and discussion of the experiment simulations with DEM

Table 4.1 shows the parameters for ten of the performed simulations. Films of the simulations as well as of DEM-experiment comparisons may be accessed at [Tsukahara, 2009]. In all of them, the time step was $10\mu\text{s}$. The hole was opened at 0.07s of simulation time.

Table 4.1: Simulation characteristics: Name (S followed by the name of corresponding experiment, followed by letter when necessary); Number n of beads; Hole radius $\tau (= B/2)$; Normal restitution coefficient e_n ; Normal contact time t_n ; Coulomb friction coefficient μ .

Name	n	τ (mm)	e_n	t_n (s)	μ
S3_1	1041	0.75	0.0011	0.0007	0.95
S3_2	1045	0.75	0.0011	0.0007	0.95
S3_3	1030	0.75	0.0011	0.0007	0.95
S4_5	1105	1.0	0.001	0.0004	0.95
S3b_1	1950	0.75	0.0011	0.0007	0.95
S3b_3	1889	0.75	0.0011	0.0007	0.95
S4b_1	1911	1.0	0.0011	0.0007	0.95
S4b_2	1950	1.0	0.0011	0.0007	0.95
S4b_3_a	1899	1.0	0.0011	0.0007	0.95
S4b_3_b	1899	1.0	0.0011	0.0007	1.35

Fig. 4.2 shows snapshots of simulation S4_5. Immobilized beads are shown in red. In the first 15ms , a rearrangement of the beads takes place. This is the initial stabilization.

Opening the shutter leads to a small flow of beads. However, the flow stops and at 0.3s the medium is at rest. Most beads move only slightly from their initial positions as shown in Fig.4.3.

Results of this kind were obtained for simulations S3_1, S3_2, S3_3, S4_5, S3b_1, S3b_3 and S4b_3_b. In those cases, the jammed configurations produced by DEM are close to the real experiments, see Fig. 4.4a and Fig. 4.4b.

However, this only works if jamming occurs upon slight motions of the beads.

For experiment 4b_3, the simulation with $\mu = 0.95$ (i.e. S4b_3_a) does not jam. In order to reproduce jamming, the friction has to be increased (simulation S4b_3_b). This indicates that the accuracy of the simulation procedure can change from case to case. Additional evidence for this point is provided by simulation S3b_3 where the simulated final configuration differs from the measured final configuration more than in the other six near-equilibrium simulations. See also section 4.3.

As to cases not near equilibrium, simulations S4b_1 and S4b_2 yield results quite different from

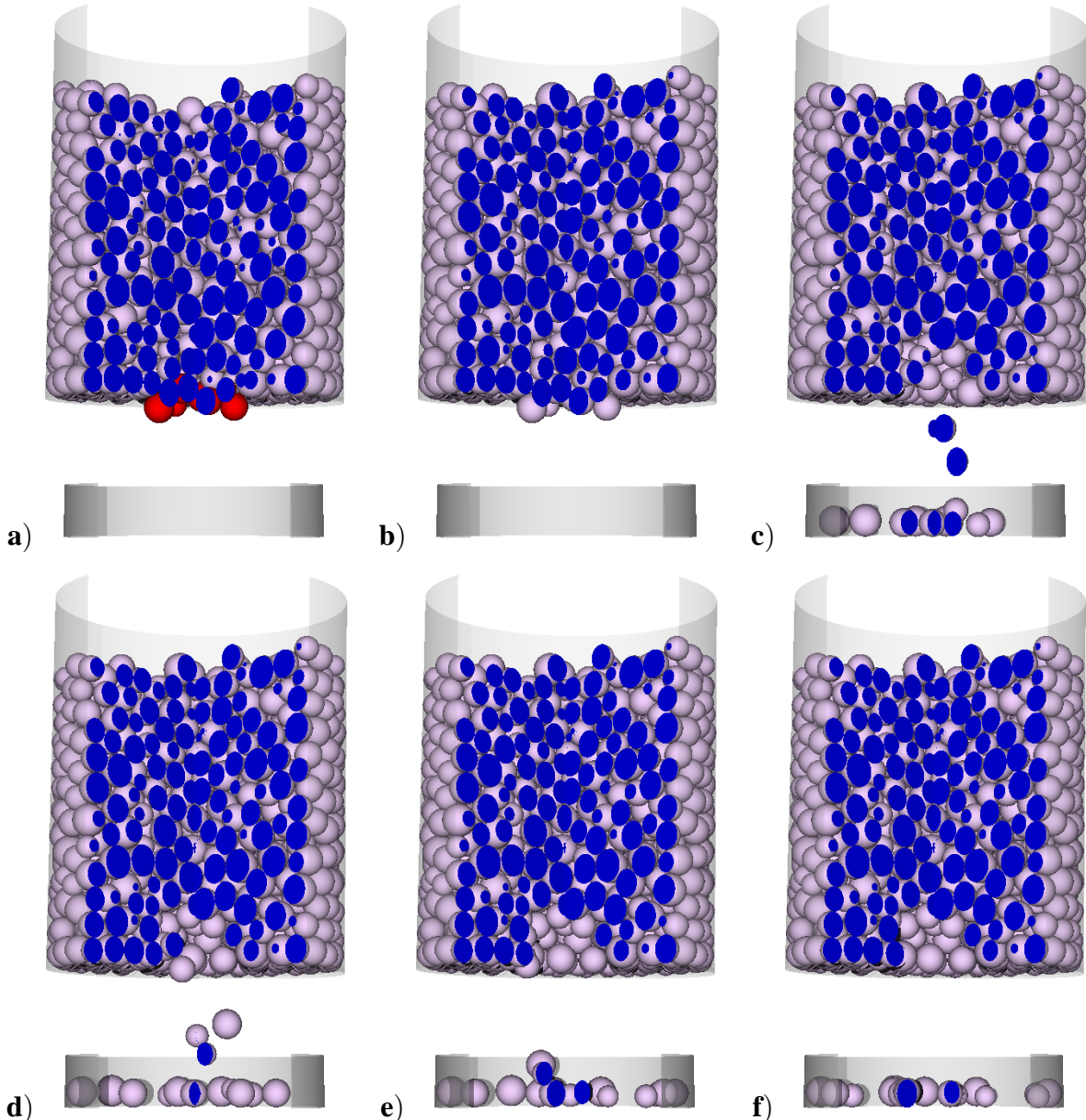


Figure 4.2: Snapshots of simulation S4_5 at times: a) 0.0s (shutter closed) b) 0.07s (opening of hole) c) 0.1s d) 0.13s e) 0.16s f) 0.19s (arched configuration)

those above. The tomographs show that jamming did not occur with only small movement of the beads but with a substantial flow. In these two cases, we did not manage to reconcile the final simulated configurations with the experimental findings. More details on this problem will be given in the following section.

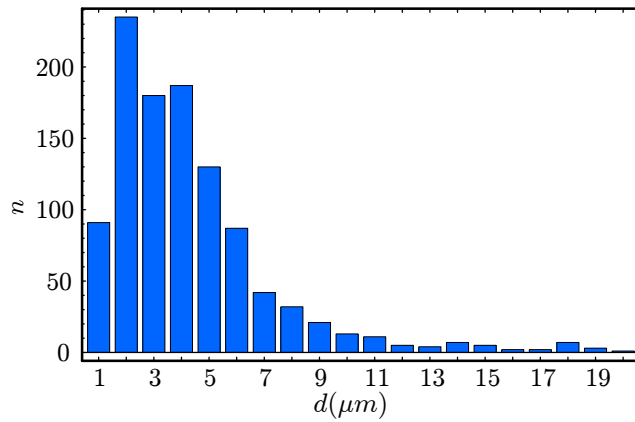


Figure 4.3: Histogram of bead displacements between 0.05s and 0.4s for simulation S4_5, outliers not shown

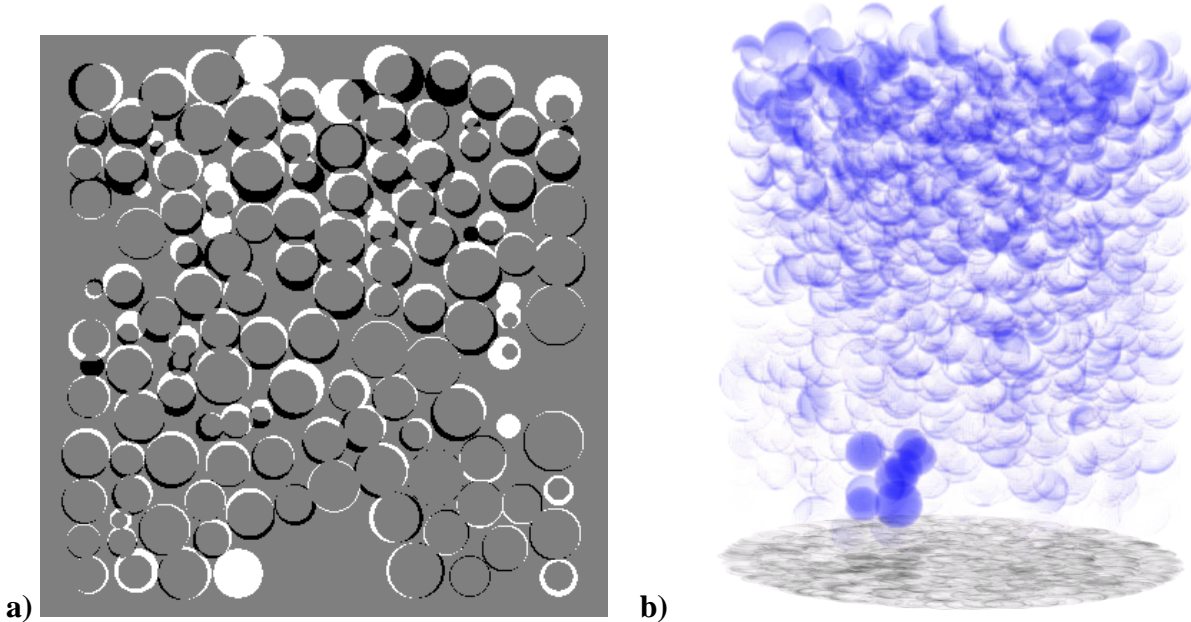


Figure 4.4: a) Vertical cut highlighting the deviation between physical experiment 4_5 and simulation S4_5: white shapes, bead traces in the simulation not coinciding with their physical experiment counterparts; black shapes, opposite case b) 3D rendered volume of the deviation between physical experiment 4_5 and simulation S4_5: beads traces in the physical experiment not coinciding with their simulation counterparts

4.3 Sensitivity analysis

To get a better idea about the scope of the presented approach an analysis of sensitivity to random data perturbations was carried out for all DEM simulations reported in Table 4.1.

The initial estimated bead data of the various hourglass experiments as provided by tomogra-

phy and image analysis, were successively subjected to three types –I, II, and III– of random perturbations of varying intensities, the first two concentrating on bead sizes and the third on their positions. As a measure of the perturbation intensity we used the square root ϵ of the mean square deviation of the radius, respectively of the center position of the beads, whichever applied. In Type I and Type II perturbations, we add independent and identically distributed (i.i.d.) Gaussian random values $\rho_i \sim N(\mu, \sigma^2)$ to the radii of the fitted beads (mean μ and variance σ^2). The mean square error of the perturbation becomes

$$\epsilon^2 = E[\rho_i] = \sigma^2 + \mu^2 \quad (4.1)$$

According to the parameter values chosen, such a perturbation may change the average sphere volumes. For a typical sphere of radius r_i this change computes as follows:

$$\begin{aligned} \langle \Delta V_i \rangle &= \frac{4}{3}\pi(E(r_i + \rho_i)^3 - r_i^3) \\ &= \frac{4}{3}\pi(3r_i^2E(\rho_i) + 3r_iE(\rho_i^2) + E(\rho_i^3)) \\ &= \frac{4}{3}\pi(3r_i^2\mu + 3r_i(\mu^2 + \sigma^2) + \mu^3 + 3\mu\sigma^2). \end{aligned} \quad (4.2)$$

For a given set of beads with radii r_1, \dots, r_n , the average change of volume is

$$\langle \Delta V \rangle = \frac{4}{3}\pi(3\langle r^2 \rangle\mu + 3\langle r \rangle(\mu^2 + \sigma^2) + \mu^3 + 3\mu\sigma^2). \quad (4.3)$$

where $\langle r \rangle$ and $\langle r^2 \rangle$ are the mean, respectively the mean squared radius of the original bead set.

In Type I perturbations, we set $\mu = 0$, thus there is no bias in the radius perturbations, which results in a mean volume increase $\langle \Delta V \rangle = 4\pi\langle r \rangle\sigma^2$.

In Type II perturbations we introduce a bias $\mu < 0$ in order to correct for this volume increase. Thus, for a given intensity $\epsilon^2 = E(\rho_i^2)$ we choose μ and σ^2 solving

$$\begin{aligned} \langle \Delta V \rangle &= -2\mu^3 + 3(\langle r^2 \rangle + \epsilon^2)\mu + 3\langle r \rangle\epsilon^2 = 0 \\ \epsilon^2 &= \mu^2 + \sigma^2. \end{aligned}$$

Finally, Type III (pure position) perturbations consist in adding i.i.d Gaussian random vectors $\gamma_i \sim N(0, \sigma^2 I)$ (with uncorrelated coordinates of means 0 and variances σ^2) to the fitted spheres' center coordinate vectors c_i . Here we use $\epsilon = \sqrt{E(\|\gamma\|^2)} = \sqrt{3}\sigma$ as a measure for the center perturbation intensity.

4.3.1 Perturbation experiments

For each simulation from Table 4.1 except simulations *S4b_1* and *S4b_3_a*, perturbations of Types I, II and III were run in succession, in each case varying the intensity ϵ between $10\mu\text{m}$ and $100\mu\text{m}$, in steps of $5\mu\text{m}$. Two replications of each perturbation were run.

In each case the simulations proceeded exactly as in the unperturbed case, see section 4.2.1. That is, each set of perturbed data was stabilized by first running the DEM simulation for 0.07 s with the hole closed. The DEM simulation was then continued for 0.23 more seconds with the hole opened. The final configuration, after a total 0.3 s simulation time, was recorded. For each experiment, the parameters for the simulation model were the same as in the unperturbed case, according to Table 4.1. The difference in behavior between perturbed and non-perturbed simulations at time t is measured using η_t , given by the following norm

$$\eta_t = \sqrt{\sum_{i=1}^n \|\mathbf{x}_{t,i}^P - \mathbf{x}_{t,i}^R\|^2}, \quad (4.4)$$

where $\{\mathbf{x}_{t,i}^P\}_{i=1}^n$ are the center positions of the beads in the perturbed simulation at time t and $\{\mathbf{x}_{t,i}^R\}_{i=1}^n$ are the center positions of the reference non-perturbed simulation at time t . Measurements of η_t have been obtained after the initial settling ($t = 0.07$ s) and for the final situation ($t = 0.3$ s).

4.3.2 Discussion of the sensitivity analysis

Fig. 4.5 represents results for experiments 3_1, 4b_2 and 4b_3. We omit depicting the corresponding graphs for the remaining simulations since they are very similar to Fig. 4.5a.

Sensitivity to size perturbations is very pronounced indeed. One can see that already with an intensity $\epsilon = 10\mu\text{m}$, which is just slightly above the resolution of the image analysis, cf. section 3.3.2, the perturbed settled system differs markedly from the unperturbed system. For size perturbation intensities $\epsilon \geq 30$ the deviation $\eta_{0.3s}$ between perturbed and unperturbed settled systems grows by several orders of magnitude. On the other hand, the sensitivity to position perturbations is much smaller. Here data perturbations of intensity up to $\epsilon = 100\mu\text{m}$ lead to essentially the same stabilized images as unperturbed data.

How can this very different response to size and location perturbations be explained?

Perturbing data can be thought of performing a certain amount of work, that is storing *perturbation energy* in the system. In the DEM model, changing positions or sizes amounts to changing the spring forces acting between the spheres and between these and the receptacle walls. Fig. 4.6 shows the amount of energy furnished by the data perturbations of the three types to the system.

Observe that the energy from size perturbations is large for type I where there is a mean volume increase. As expected, perturbations of the same intensity increasing the average volume require much more work than size perturbations keeping the volume constant. The latter turn out to require much the same work as position perturbations of an equivalent amount, which is what a simple geometric reasoning would lead one to surmise.

But this means that the large difference between the response to size perturbations and that to position perturbations cannot be explained by a difference in the amount of perturbation energy stored in the system. Now observe that, when perturbing data, the new system will develop forces driving it in a direction opposite to the perturbations. In case of position perturbations

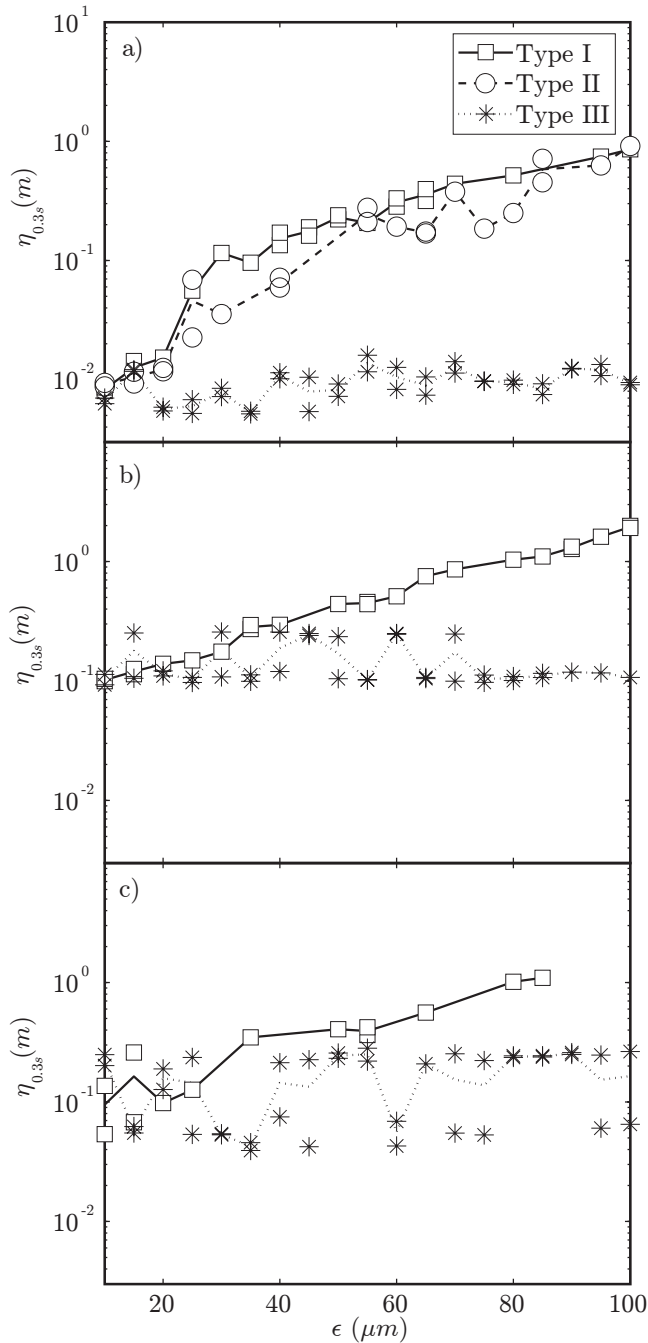


Figure 4.5: Sensitivity analysis results showing the dominating effect of size vs. position perturbations; $\eta_{0.3s}(\epsilon)$ is given for experiments: a) 3_1, b) 4b_2, c) 4b_3. Type II perturbations were only carried out for experiment 3_1. Lines represent the average value of the corresponding replications. Note that plots of type I and II coincide and dominate the plot of type III.

the system will develop restitutive forces driving it back to the unperturbed situation provided the perturbation is not too large. On the other hand, whenever sizes are perturbed, there is normally no equilibrium configuration for the new spheres in the vicinity of their old positions. Hence the stored deformation energy cannot drive the system back to the old set of positions, but will drive the system to a new equilibrium.

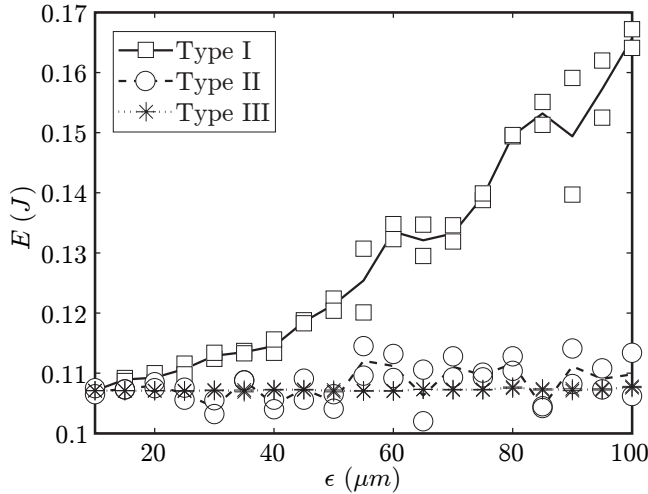


Figure 4.6: Plots of $E(\epsilon)$, energy furnished to the system as a function of perturbation size for experiment 3_1. Lines represent the average value of the corresponding replications. Note that the plot of type I dominates the coinciding plots of type II and III.

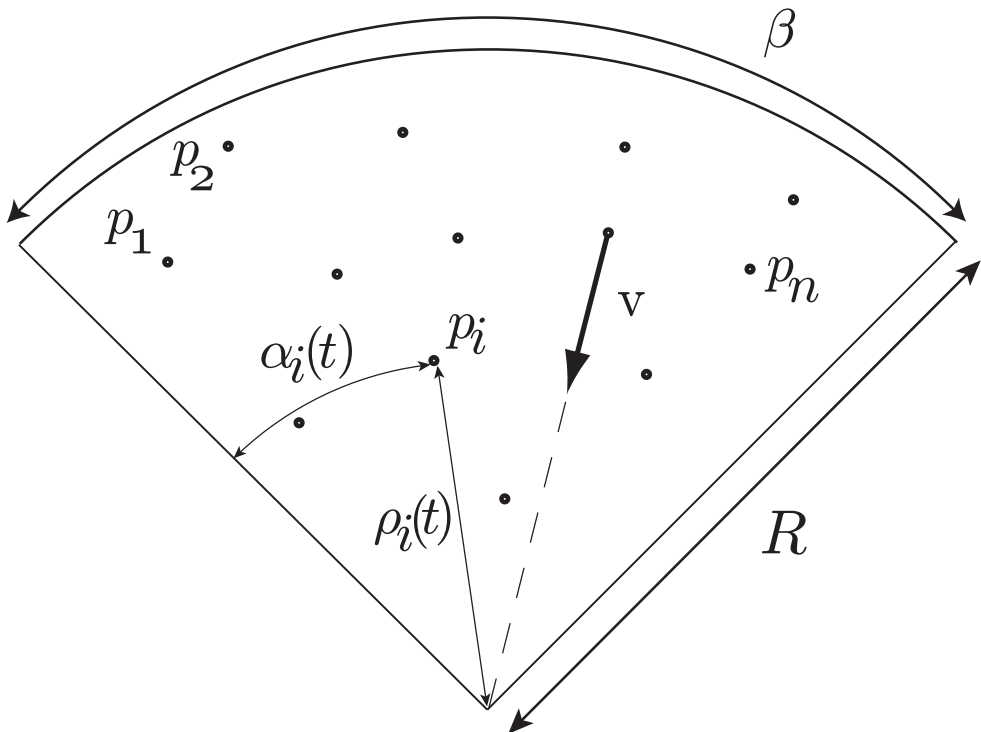
Fig. 4.5b shows sensitivity to perturbations for experiment 4b_2 for which jamming took place after a substantial flow. Such a flow occurred also for the corresponding non-perturbed and perturbed simulations and sensitivity to perturbations is approximately 10 times higher than for instant-jamming experiments even for small perturbations ($\sim 10\mu m$). This shows that correctly simulating the experiment, with its substantial flow, is not possible with the means at hand. In this case, simulations show a chaotic behavior, i.e. a high sensitivity to small data perturbations.

A large flow of beads also occurred for perturbed simulations of experiment 4b_3 (Fig. 4.5c). These two cases showed a very high sensitivity, not only to size but also to location perturbations. This fact indicates that the associated initial configurations are unstable. For such cases, where the motion quickly becomes chaotic, Tomo-DEM presently attains its limit.

4.4 Ensemble forecasting

Experiments of jamming with beads have been presented in this chapter. X-ray synchrotron tomography has allowed us to take 3D snapshots of the experiments. The tomographs obtained were analyzed to estimate the positions and radii of the beads, before and after opening the hole. Simulations were run to test if DEM can reproduce the experiments. Through this study, we have found evidence that DEM enables accurate estimates of the jammed configurations. We go one step further than recent DEM validations that study how DEM can reproduce "global" phenomena (see chapter 1). However, we have also noticed that the precision of our predictions varies from case to case. Even in certain cases, our attempts to predict jamming are wrong: the DEM model predicts jamming while in reality flow occurs or vice versa. This is not without reminding what happens in meteorology where atmospheric models can forecast tomorrow's weather while there is a non-negligible probability that the forecast be quite false. Today's meteorologists use ensemble forecasting to limit the probability of giving a false forecast. Briefly, given a forecasting method, ensemble forecasting consists in using the method on

a set of initial conditions to lessen the forecasting error. Ensemble forecasting has its roots in the work of Laplace who first suggested to combine two methods of forecasting to lessen the error [Laplace, 1818]. Gibbs introduced the notion of an ensemble in statistical physics as a set of states of a system. In [Sanders, 1963], Sanders proposed to use probability forecasting in meteorology. In [Geisser, 1965], Geisser gave what appears to be the earliest Bayesian approach to combining estimates. However, most forecasters consider that the foundations for ensemble forecasting was given by Bates and Granger [Bates and Granger, 1969]. Since then, ensemble forecasting has been applied to many domains such as economics, management, psychology, climatology or ecology. The reader can find more information on the different applications of ensemble forecasting in [Clemen, 1989; Araújo and New, 2006]. In that our predictions of jamming are uncertain, it may be interesting to apply ensemble forecasting to this problem. It is in our plans to test this in future work. The idea would be to apply perturbations as was done in the preceding sensitivity analysis but with smaller perturbations, nearer to size of the error made when estimating the positions and radii. Note that even though the sensitivity analysis carried out in this chapter concerned positions and radii, the sensitivity of other parameters of DEM such as friction, restitution coefficient, or contact time could be similarly analyzed in future work on ensemble forecasting.



Part III

Simple modeling, statistical physics and global modeling

It has been said that 'the human mind has never invented a labor-saving machine equal to algebra.' If this be true, it is but natural and proper that an age like our own, characterized by the multiplication of labor-saving machinery, should be distinguished by the unexampled development of this most refined and most beautiful of machines.

– Josiah Willard Gibbs

Chapter 5

Two bi-indexed recurrence sequences

5.1 Introduction

In this chapter we study two kinds of bi-indexed recurrence sequences (sequences of numbers given by a recurrence relation and doubly indexed) that we name $G^{(u)}$ and $F^{(u)}$. $F^{(u)}$ will appear in an analytical formula developed in chapter 6 giving the jamming probability for a simple model of granular flow in a hopper (model SPM-C). We will see that $G^{(u)}$ is closely tied to $F^{(u)}$. We shall also see that there exist different ways to calculate values of these sequences, and that depending on which values are wanted, one or the other way can be more efficient. Before entering the study of $G^{(u)}$ and $F^{(u)}$, let us first briefly introduce the topic of recurrence relations.

One of the most simple number sequences given by a recurrence relation is the geometric progression defined (in \mathbb{N}) by the start value $a_0 \in \mathbb{N}$, the ratio $r \in \mathbb{N}$ and the recurrence relation $a_n = ra_{n-1}$.

There is recorded trace of such progressions in the Seleucid civilisation (312-64 BC). A number sequence defined by a bit more complicated recurrence relation was studied around 200 BC by the writer Pingala of ancient India. While working on mathematical concepts of prosody, he discovered the bi-indexed sequence of what are now called the binomial coefficients and that can be presented in what is now called Pascal's triangle. Another sequence has received much interest by Pingala, Viranhanka, the Indian prosodist, Gopāla, the Indian mathematician and around 1150 AD, the Jain writer Hemachandra. This sequence of numbers is defined by the start values $a_0, a_1 = 1$, and the recurrence relation $a_n = a_{n-1} + a_{n-2}$.

These numbers were also presented by Leonardo of Pisa also named Fibonacci (c. 1170- c. 1250), the mathematician of the Middle Ages. He modeled the growth of an idealized rabbit population with these numbers. The sequence is now known as the Fibonacci sequence.

These are the cornerstone works on sequences defined by recurrence relations, also called recurrence sequences. Since the 17th century much work has been done on such sequences. For

a thorough survey on recurrence sequences from the 17th century to the beginning of the 20th century the reader can consult [Dickson, 1971]. For a more recent account on the problem the reader can consult [Everest et al., 2003]. We give here some important facts on recurrence sequences to give the reader some ideas on the subject.

First, let us enumerate some important recurrence sequences.

In the 18th century, Leonhard Euler (1707-1783), while trying to count the number of ways of dividing a polygon into triangles, presented the now called Catalan numbers that can be defined by

$$C_0 = 1 \text{ and } C_{n+1} = \sum_{i=0}^n C_i C_{n-i} \text{ for } n > 0 \quad (5.1)$$

or

$$C_n = \frac{1}{n+1} \binom{2n}{n}. \quad (5.2)$$

They arise often in counting problems.

In the 18th century, James Stirling (1692-1770) presented two types of number sequences: the Stirling numbers of the first kind obeying the recurrence relation

$$s(n+1, m) = s(n, m-1) - ns(n, m), \quad (5.3)$$

which count the number of permutations of n elements with k permutation cycles, and the Stirling numbers of the second kind obeying the recurrence relation

$$S(n, m) = S(n-1, m-1) + kS(n-1, m), \quad (5.4)$$

which count the number of ways partitioning a n -element set into k nonempty subsets.

Other sequences such as the Narayana numbers, the Pell numbers, the Lucas sequences or the Padovan sequence have also been much studied.

Studying the general resolution of certain types of recurrence relations is also an important problem. A pioneering result in this sense is the work of Joseph-Louis Lagrange (1736-1813) and G. F. Malfatti (1731-1807) that has allowed writing explicit expressions for linear homogeneous recurrence relations with constant coefficients. Such a relation is of the form

$$a_n = c_1 a_{n-1} + \cdots + c_d a_{n-d}, \quad (5.5)$$

where the c_i , $i = 1, \dots, d$ are constant coefficients. See [Lucas, 1961] and [Dickson, 1971] for more information on the subject.

Everest et al. [Everest et al., 2003] describe in their introduction "the modern study of the arithmetic of recurrence sequences as having been given essential impetus by the remarkable work of François Édouard Anatole Lucas (1842-1891)". Modern study of recurrence relations concerns diverse domains such as cryptography, coding theory, pseudo-random number generators, fractals, graph theory, orthogonal polynomials, numerical analysis or cellular automata. Anecdotically, linear recurrence sequences had a part in the proof of Hilbert's Tenth Problem.

In this chapter, we give some results on two specific recurrence sequences defined by bi-indexed linear homogeneous relations with constant coefficients. Such a relation has the form

$$\sum_{i=0}^d \sum_{j=0}^e c_{i,j} a_{n-i, m-j} = 0. \quad (5.6)$$

5.2 Placing balls into fixed-size urns

5.2.1 An introductory example

One way of defining the usual binomial coefficient $\binom{n}{k}$ for $n \in \mathbb{N}^+$, $k \in \mathbb{Z}$ is:

$$\binom{n}{k} = \binom{n-1}{k} + \binom{n-1}{k-1}, \quad n > 0 \quad (5.7)$$

where boundary conditions are

$$\binom{0}{k} = \begin{cases} 1 & k = 0 \\ 0 & k \neq 0 \end{cases}. \quad (5.8)$$

Let us consider now the coefficient defined for $n \in \mathbb{N}^+$, $k \in \mathbb{Z}$ given by

$$G(n, k) = G(n-1, k) + G(n-1, k-1) + G(n-1, k-2), \quad n > 0 \quad (5.9)$$

which is similar to (5.7), and the same boundary conditions as in (5.8).

$$G(0, k) = \begin{cases} 1 & k = 0 \\ 0 & k \neq 0 \end{cases}. \quad (5.10)$$

It can be shown from the preceding definitions that

$$\binom{n}{k} = G(n, k) = \begin{cases} 1 & k = 0 \\ 0 & k < 0 \end{cases}, \quad \forall n \geq 0. \quad (5.11)$$

So, the coefficients are equal for $k \leq 0$.

We also find that

$$\begin{aligned} G(n, 1) &= G(n-1, 1) + G(n-1, 0) + G(n-1, -1) \\ &= G(n-1, 1) + G(n-1, 0), \quad n > 0 \end{aligned} \quad (5.12)$$

using (5.11).

Hence, we notice that for $k = 1$, G is given by a recurrence relation with only 2 terms on the right-hand side, thus resembling the binomial coefficients. In fact, the coefficients are also equal for $k = 1$.

As to the case when $k \geq 2$, we notice that

$$\begin{aligned} \binom{n}{k} &= \binom{n-1}{k} + \binom{n-1}{k-1} \\ &= \binom{n-2}{k} + \binom{n-2}{k-1} + \binom{n-1}{k-1} \\ &\quad \cdot \\ &\quad \cdot \\ &\quad \cdot \\ &= \binom{0}{k-1} + \cdots + \binom{n-1}{k-1} \end{aligned} \quad (5.13)$$

$\forall n > 0, k \in \mathbb{Z}$ and

$$\begin{aligned} G(n, k) &= G(n-1, k) + G(n-1, k-1) + G(n-1, k-2) \\ &= G(n-2, k) + G(n-2, k-1) + G(n-2, k-2) \\ &\quad + G(n-1, k-1) + G(n-1, k-2) \\ &\quad \cdot \\ &\quad \cdot \\ &= G(0, k-1) + G(0, k-2) + G(1, k-1) + G(1, k-2) \\ &\quad + \cdots + G(n-1, k-1) + G(n-1, k-2) \end{aligned} \quad (5.14)$$

Taking $k = 2$ in (5.14), we notice that $G(n, 2) = \binom{n}{2} + \binom{n}{1}$. Further scrutiny shows that $\forall n \in \mathbb{N}^+, \forall k \in \mathbb{Z}$, $G(n, k)$ can be written as

$$G(n, k) = \sum_{l=0}^k \binom{l}{k-l} \binom{n}{l}. \quad (5.15)$$

We will prove a more general result a bit further. Comparing the definition we gave of G and equation (5.15) we start getting the idea that there are different ways of calculating $G(n, k)$.

5.2.2 Definition of recurrence sequence $G^{(u)}(n, k)$

Consider $u \geq 1$. Let $G^{(u)} : \mathbb{Z} \times \mathbb{Z} \longrightarrow \mathbb{N}$ be the generalization of the binomial coefficient defined by the following three equations

$$G^{(u)}(n, k) = 0 \text{ if } n < 0, k \in \mathbb{Z} \quad (5.16)$$

$$G^{(u)}(n, k) = \begin{cases} 1 & \text{if } n \geq 0, k = 0 \\ 0 & \text{if } n \geq 0, k < 0 \end{cases} \quad (5.17)$$

$$\begin{aligned} G^{(u)}(n, k) = & \\ G^{(u)}(n-1, k) + G^{(u)}(n-1, k-1) + \cdots + G^{(u)}(n-1, k-u+1), & n \geq 0, k > 0. \end{aligned} \quad (5.18)$$

Tables 5.1 and 5.2 show the values of $G^{(u)}(n, k)$ for $n \leq 10, k \leq 10$ and $u = 3, 4$. In table 5.1, the values highlighted in black and with a solid line are tied by the recurrence relation (5.18) for $u = 3, n = 6$ and $k = 6$.

$n \setminus k$	0	1	2	3	4	5	6	7	8	9	10
0	1	0	0	0	0	0	0	0	0	0	0
1	1	1	1	0	0	0	0	0	0	0	0
2	1	2	3	2	1	0	0	0	0	0	0
3	1	3	6	7	6	3	1	0	0	0	0
4	1	4	10	16	19	16	10	4	1	0	0
5	1	5	15	30	45	51	45	30	15	5	1
6	1	6	21	50	90	126	141	126	90	50	21
7	1	7	28	77	161	266	357	393	357	266	161
8	1	8	36	112	266	504	784	1016	1107	1016	784
9	1	9	45	156	414	882	1554	2304	2907	3139	2907
10	1	10	55	210	615	1452	2850	4740	6765	8350	8953

Table 5.1: Some numerical values of $G^{(u)}(n, k)$ for $u = 3$

5.2.3 Interpretation of recurrence sequence $G^{(u)}(n, k)$

Call $\hat{G}^{(u)}(n, k)$ the number of ways of placing k undistinguishable balls in n distinguishable urns, where each urn can hold $u - 1$ balls. It is shown in this section that $G^{(u)}(n, k)$ and $\hat{G}^{(u)}(n, k)$ are identical.

$n \setminus k$	0	1	2	3	4	5	6	7	8	9	10
0	1	0	0	0	0	0	0	0	0	0	0
1	1	1	1	1	0	0	0	0	0	0	0
2	1	2	3	4	3	2	1	0	0	0	0
3	1	3	6	10	12	12	10	6	3	1	0
4	1	4	10	20	31	40	44	40	31	20	10
5	1	5	15	35	65	101	135	155	155	135	101
6	1	6	21	56	120	216	336	456	546	580	546
7	1	7	28	84	203	413	728	1128	1554	1918	2128
8	1	8	36	120	322	728	1428	2472	3823	5328	6728
9	1	9	45	165	486	1206	2598	4950	8451	13051	18351
10	1	10	55	220	705	1902	4455	9240	17205	29050	44803

Table 5.2: Some numerical values of $G^{(u)}(n, k)$ for $u = 4$

Let us call $H(n, k, l)$ the number of ways of placing k undistinguishable balls in n distinguishable urns, where each urn can hold $u - 1$ balls knowing that in the first urn there are l balls.

Then $\hat{G}^{(u)}(n, k) = H(n, k, 0) + \dots + H(n, k, \max(u - 1, k))$.

We also have $H(n, k, 0) = \hat{G}^{(u)}(n - 1, k)$, ..., $H(n, k, \max(u - 1, k)) = \hat{G}^{(u)}(n - 1, k - \max(u - 1, k))$.

So

$$\hat{G}^{(u)}(n, k) = \hat{G}^{(u)}(n - 1, k) + \dots + \hat{G}^{(u)}(n - 1, k - \max(u - 1, k)). \quad (5.19)$$

Furthermore, there is one way to place 0 undistinguishable balls in n distinguishable urns, where each urn can hold $u - 1$. Thus, $G^{(u)}(n, k)$ and $\hat{G}^{(u)}(n, k)$ are equal for $k = 0$ and $n = 0$. Then, by equation (5.19), $G^{(u)}(n, k)$ and $\hat{G}^{(u)}(n, k)$ are equal for $k \geq 0$ and $n \geq 0$.

We will now prove some new recurrence relations for these generalizations of the binomial coefficients. The results will be illustrated in tables 5.1 and 5.2.

5.2.4 A first theorem for $G^{(u)}(n, k)$

Theorem 1

$$G^{(u)}(n, k) = \sum_{l=0}^k G^{(u-1)}(l, k-l) \binom{n}{l}, \forall u \geq 2, \forall n, k \in \mathbb{Z} \quad (5.20)$$

Proof

- 1) Suppose $n < 0$, $G^{(u)}(n, k) = 0$ and $\sum_{l=0}^k G^{(u-1)}(l, k-l) \binom{n}{l} = 0$, the theorem holds in this case.
- 2) Suppose $k < 0$ and $n \geq 0$, a simple recurrence shows that $G^{(u)}(n, k) = 0$ and $\sum_{l=0}^k G^{(u-1)}(l, k-l) \binom{n}{l} = 0$, the theorem holds in this case.
- 3) Suppose $k = 0$ and $n \geq 0$, a simple recurrence shows that $G^{(u)}(n, k) = 1$ and $\sum_{l=0}^k G^{(u-1)}(l, k-l) \binom{n}{l} = 1$, the theorem holds in this case.
- 4) Suppose $k > 0$ and $n \geq 0$. We have just seen that the theorem holds for $k = 0$, $n \geq 0$, we take the recurrence hypothesis that the theorem holds for $n \geq 0$ up to $k - 1$.

By the definition of $G^{(u)}$,

$$\begin{aligned}
G^{(u)}(n, k) &= G^{(u)}(n-1, k) + G^{(u)}(n-1, k-1) + \cdots + G^{(u)}(n-1, k-u+1) \\
&= G^{(u)}(n-2, k) + G^{(u)}(n-2, k-1) + \cdots + G^{(u)}(n-2, k-u+1) \\
&\quad + G^{(u)}(n-1, k-1) + \cdots + G^{(u)}(n-1, k-u+1) \\
&\quad \cdot \\
&\quad \cdot \\
&\quad \cdot \\
&= G^{(u)}(0, k) + G^{(u)}(0, k-1) + \cdots + G^{(u)}(0, k-u+1) \\
&\quad + G^{(u)}(1, k-1) + \cdots + G^{(u)}(1, k-u+1) \\
&\quad + \cdots \\
&\quad + G^{(u)}(n-1, k-1) + \cdots + G^{(u)}(n-1, k-u+1).
\end{aligned}$$

It can be shown that $G^{(u)}(0, k) = 0$, $k > 0$.

Knowing this and introducing our recurrence hypothesis, we find that

$$\begin{aligned}
G^{(u)}(n, k) &= \sum_{l=0}^{k-1} G^{(u-1)}(l, k-1-l) \binom{0}{l} + \cdots \\
&\quad + \sum_{l=0}^{k-u+1} G^{(u-1)}(l, k-u+1-l) \binom{0}{l} \\
&\quad + \cdots \\
&\quad + \sum_{l=0}^{k-1} G^{(u-1)}(l, k-1-l) \binom{n-1}{l} + \cdots \\
&\quad + \sum_{l=0}^{k-u+1} G^{(u-1)}(l, k-u+1-l) \binom{n-1}{l}.
\end{aligned}$$

Since $\binom{0}{l} + \cdots + \binom{n-1}{l} = \binom{n}{l+1}$,

$$\begin{aligned} G^{(u)}(n, k) &= \sum_{l=0}^{k-1} G^{(u-1)}(l, k-1-l) \binom{n}{l+1} \\ &\quad + \dots \\ &\quad + \sum_{l=0}^{k-u+1} G^{(u-1)}(l, k-u+1-l) \binom{n}{l+1}. \end{aligned}$$

By shifting l , we find,

$$\begin{aligned} G^{(u)}(n, k) &= \sum_{l=1}^k G^{(u-1)}(l-1, k-l) \binom{n}{l} \\ &\quad + \dots \\ &\quad + \sum_{l=1}^{k-u+2} G^{(u-1)}(l-1, k-u+2-l) \binom{n}{l}, \end{aligned}$$

which can be written

$$\begin{aligned} G^{(u)}(n, k) &= \sum_{l=1}^k G^{(u-1)}(l-1, k-l) \binom{n}{l} \\ &\quad + \dots \\ &\quad + \sum_{l=1}^k G^{(u-1)}(l-1, k-u+2-l) \binom{n}{l}, \end{aligned}$$

since $G^{(u-1)}(l-1, k'-l) = 0$ for $k' > k-u+2$.

Furthermore, we notice that by the definition of $G^{(u-1)}$,

$$G^{(u-1)}(l, k-l) = G^{(u-1)}(l-1, k-l) + \dots + G^{(u-1)}(l-1, k-u+2-l) \quad (5.21)$$

which shows that

$$G^{(u)}(n, k) = \sum_{l=1}^k G^{(u-1)}(l, k-l) \binom{n}{l}$$

and finally

$$G^{(u)}(n, k) = \sum_{l=0}^k G^{(u-1)}(l, k-l) \binom{n}{l}. \quad \blacksquare$$

The unique value highlighted in Table 5.2 is tied by relation (5.20) to the values highlighted in blue (long dashes) in Table 5.1.

5.2.5 A second theorem for $G^{(u)}(n, k)$

Theorem 2

$$G^{(u)}(n, k) = \frac{n}{k} \sum_{l=1}^{u-1} l G^{(u)}(n-1, k-l), \forall u \geq 1, \forall n \geq 0, k \geq 1$$

Proof

We give a combinatorial proof of this theorem.

As we have seen, $G^{(u)}(n, k)$ can be seen as the number of ways of placing k undistinguishable balls in n distinguishable urns, where each urn can hold $u - 1$ balls.

We suppose the urns are numbered from 1 to n . Let us consider the following experience consisting of $u - 1$ steps:

- Step 1: we place a ball in urn 1, place the $k - 1$ remaining balls in the $n - 1$ remaining urns in all possible ways, writing a mark for each of these ways. We do the same for urns 2 to n .
- Step 2: we place 2 balls in urn 1, place the $k - 2$ remaining balls in the $n - 1$ remaining urns in all possible ways, writing 2 marks for each of these ways. We do the same for urns 2 to n .
- ...
- Step $u-1$: we place $u-1$ balls in urn 1, place the $k - u + 1$ remaining balls in the $n - 1$ remaining urns in all possible ways, writing $u - 1$ marks for each of these ways. We do the same for urns 2 to n .

Now we consider one given way of placing k balls in the n urns. This placement has appeared in our experience several times and a total of exactly k marks have been written while it was the current configuration. From this we conclude that

$$k G^{(u)}(n, k) \tag{5.22}$$

marks have been written at the end of the experience.

Also, within step l , $nl G^{(u)}(n-1, k-l)$ marks have been written. So,

$$\sum_{l=1}^{u-1} nl G^{(u)}(n-1, k-l) \tag{5.23}$$

marks have been written at the end of the experience.

By equating (5.22) and (5.23), we prove the theorem. ■

5.2.6 A lemma generalizing theorem 2

Lemma 2 If $\omega_{n,k}$ is a bi-indexed sequence of integers that satisfies

- 1) $\omega_{n,k} = \omega_{n-1,k} + \dots + \omega_{n-1,k-u+1}, \forall n > 0, k \geq 0,$
- 2) $\omega_{n,k+1} = \gamma_1(n, k)\omega_{n-1,k} + \dots + \gamma_{u-1}(n, k)\omega_{n-1,k-u+2}, \forall n > 0, k \geq 0$ where $\gamma_i : \mathbb{N}^* \times \mathbb{N} \mapsto \mathbb{R}_+, i = 1, \dots, u-1,$
- 3) $\omega_{n,k+\alpha} = \beta_1(n, k)\omega_{n-1,k} + \dots + \beta_{u-1}(n, k)\omega_{n-1,k-u+2}, \forall n > 0, k \geq 0$ where $\beta_i : \mathbb{N}^* \times \mathbb{N} \mapsto \mathbb{R}_+, i = 1, \dots, u-1, \text{ for some } \alpha > 0$

then,

$\exists \delta_i : \mathbb{N}^* \times \mathbb{N} \mapsto \mathbb{R}, i = 1, \dots, u-1$ such as $\omega_{n,k+\alpha+1} = \delta_1(n, k)\omega_{n-1,k} + \dots + \delta_{u-1}(n, k)\omega_{n-1,k-u+2}, \forall n > 0, k \geq 0.$

Proof

Let $n > 0$ and $k \geq 0$. Multiplying condition 1) of the lemma by $\beta_1(n, k)$ and subtracting the resulting equation from condition 3) yields

$$\omega_{n,k+\alpha} - \beta_1(n, k)\omega_{n,k} = (\beta_2(n, k) - \beta_1(n, k))\omega_{n-1,k-1} + \dots + (\beta_{u-1}(n, k) - \beta_1(n, k))\omega_{n-1,k-u+2} - \beta_1(n, k)\omega_{n-1,k-u+1}.$$

Replacing k by $k+1$ in this last equation yields

$$\begin{aligned} \omega_{n,k+\alpha+1} - \beta_1(n, k+1)\omega_{n,k+1} &= (\beta_2(n, k+1) - \beta_1(n, k+1))\omega_{n-1,k} + \\ &\quad \dots + (\beta_{u-1}(n, k+1) - \beta_1(n, k+1))\omega_{n-1,k-u+3} \\ &\quad - \beta_1(n, k+1)\omega_{n-1,k-u+2}. \end{aligned}$$

Adding $\beta_1(n, k+1)$ times condition 2) of the lemma to this last equation yields

$$\begin{aligned} \omega_{n,k+\alpha+1} &= (\beta_1(n, k+1)(\gamma_1(n, k) - 1) + \beta_2(n, k+1))\omega_{n-1,k} + \\ &\quad \dots + (\beta_1(n, k+1)(\gamma_{u-2}(n, k) - 1) + \beta_{u-1}(n, k+1))\omega_{n-1,k-u+3} \\ &\quad + (\beta_1(n, k+1)(\gamma_{u-1}(n, k) - 1))\omega_{n-1,k-u+2}. \end{aligned}$$

Writing $\delta_1(n, k) = \beta_1(n, k+1)(\gamma_1(n, k) - 1) + \beta_2(n, k+1), \dots, \delta_{u-2}(n, k) = \beta_1(n, k+1)(\gamma_{u-2}(n, k) - 1) + \beta_{u-1}(n, k+1)$ and $\delta_{u-1}(n, k) = \beta_1(n, k+1)(\gamma_{u-1}(n, k) - 1)$, the theorem is proven. ■

Corollary 1 According to theorem 2, $\forall u \geq 1$, $G^{(u)}$ is a bi-indexed sequence of integers that satisfies the conditions of lemma 2 for $\alpha = 1$. By applying recursively lemma 2 we find that

- 1) there are functions $\xi_1^{(1)}, \dots, \xi_{u-1}^{(1)} : \mathbb{N}^* \times \mathbb{N} \mapsto \mathbb{R}_+$ such that

$$G_{n,k+1}^{(u)} = \xi_1^{(1)}(n, k)G_{n-1,k}^{(u)} + \dots + \xi_{u-1}^{(1)}(n, k)G_{n-1,k-u+2}^{(u)}, \forall n > 0, k \geq 0$$

2) there are functions $\xi_1^{(2)}, \dots, \xi_{u-1}^{(2)} : \mathbb{N}^* \times \mathbb{N} \mapsto \mathbb{R}_+$ such that

$$G_{n,k+2}^{(u)} = \xi_1^{(2)}(n, k) G_{n-1,k}^{(u)} + \dots + \xi_{u-1}^{(2)}(n, k) G_{n-1,k-u+2}^{(u)}, \forall n > 0, k \geq 0$$

.

.

.

u-1) there are functions $\xi_1^{(u-1)}, \dots, \xi_{u-1}^{(u-1)} : \mathbb{N}^* \times \mathbb{N} \mapsto \mathbb{R}_+$ such that

$$G_{n,k+u-1}^{(u)} = \xi_1^{(u-1)}(n, k) G_{n-1,k}^{(u)} + \dots + \xi_{u-1}^{(u-1)}(n, k) G_{n-1,k-u+2}^{(u)}, \forall n > 0, k \geq 0,$$

and

$$\begin{cases} \xi_j^{(i)}(n, k) = \xi_1^{(i-1)}(n, k+1) (\xi_j^{(1)}(n, k) - 1) + \xi_{j+1}^{(i-1)}(n, k+1), & i = 1, \dots, u-2 \\ \xi_{u-1}^{(i)}(n, k) = \xi_1^{(i-1)}(n, k+1) (\xi_{u-1}^{(1)}(n, k) - 1) \end{cases} . \quad (5.24)$$

In Table 5.1, the values highlighted with a red line (short dashes) are tied by the recurrence relations given in corollary 1 for $u = 3$, $n = 9$, and $k = 3$. Note that in this case, there are two recurrence relations. In Table 5.1 the first relation corresponds to the red rectangles (short dashes) and the second to the red ovals (short dashes).

5.2.7 How to calculate values of $G^{(u)}(n, k)$

Consider the following 3 problems:

- $P_1(u, n, k)$: calculate $G^{(r)}(p, q)$ for $r = u$, $p = 1, \dots, n$ and $q = 1, \dots, k$
- $P_2(u, n, k)$: calculate $G^{(r)}(p, q)$ for $r = 1, \dots, u$, $p = n$ and $q = 1, \dots, k$
- $P_3(u, n, k)$: calculate $G^{(r)}(p, q)$ for $r = u$, $p = n$ and $q = k$.

For each problem, we give here three different algorithms for its resolution. We call the algorithms $\mu_{i,j}$ where i refers to problem and j gives the number of the method.

We give the calculation for $u \geq 1$, $n > 0$ and $k > 0$ since the cases for $n < 0$ and $k \leq 0$ are given in the definition, and for $n = 0$ and $k > 0$, $G^{(u)}(n, k) = 0$.

Note that we write $\vec{\xi}^{(i)}(n, k) = \begin{pmatrix} \xi_1^{(i)} \\ \vdots \\ \cdot \\ \vdots \\ \xi_{u-1}^{(i)} \end{pmatrix}$, $i = 1, \dots, u-1$ where $\xi_1^{(i)}, \dots, \xi_{u-1}^{(i)}$ are as in corollary 1.

$\mu_{P_1(u,n,k), 1}$	<ul style="list-style-type: none"> For $p = 1, \dots, n$ For $q = 1, \dots, k$ $G^{(u)}(p, q) = G^{(u)}(p, q-1) - G^{(u)}(p-1, q-1-u+1) + G^{(u)}(p-1, q)$
$\mu_{P_2(u,n,k), 2}$	<ul style="list-style-type: none"> Notice that $G^{(1)}(n, k) = \begin{cases} 1 & \text{if } n \geq 0 \text{ and } k = 0 \\ 0 & \text{otherwise} \end{cases}$ Calculate $G^{(2)}(p, q) = \binom{p}{q}, p = 1, \dots, \max\{n, k\}, q = 1, \dots, \max\{n, k\}$ using $\mu_{P_2(2, \max\{n, k\}, \max\{n, k\}), 2}$ For $r = 3, \dots, u-1$ <ul style="list-style-type: none"> For $q = 1, \dots, k$ For $p = 1, \dots, k+1-q$ $G^{(r)}(p, q) = \sum_{l=0}^q G^{(r-1)}(l, q-l) \binom{p}{l}$ For $r = 3, \dots, u$ <ul style="list-style-type: none"> For $q = 1, \dots, k$ $G^{(r)}(n, q) = \sum_{l=0}^q G^{(r-1)}(l, q-l) \binom{n}{l}$
$\mu_{P_3(u,n,k), 3}$	<ul style="list-style-type: none"> Calculate $M = \lfloor \frac{k-1}{u-1} \rfloor$ For $m = 0, \dots, M$ <ul style="list-style-type: none"> For $r = 1, \dots, u-1$ <ul style="list-style-type: none"> For $s = 0, \dots, u-1-r$ <ul style="list-style-type: none"> Calculate $\bar{\xi}^{(r)}(n-1-m, (M-m)(u-1)+s)$ using theorem 2 if $r = 1$ or (5.24) otherwise For $m = 0, \dots, M$ <ul style="list-style-type: none"> For $w = 1, \dots, u-1$ <ul style="list-style-type: none"> Calculate $G^{(u)}(n-M+m, m(u-1)+w)$ using corollary 1
$\mu_{P_1(u,n,k), 2}$	<ul style="list-style-type: none"> Apply $\mu_{P_2(u,1,k), 2}, \dots, \mu_{P_2(u,n,k), 2}$
$\mu_{P_1(u,n,k), 3}$	<ul style="list-style-type: none"> Apply $\mu_{P_3(u,1,k), 3}, \dots, \mu_{P_3(u,n,k), 3}$
$\mu_{P_2(u,n,k), 1}$	<ul style="list-style-type: none"> Apply $\mu_{P_1(1,n,k), 1}, \dots, \mu_{P_1(u,n,k), 1}$
$\mu_{P_2(u,n,k), 3}$	<ul style="list-style-type: none"> Apply $\mu_{P_3(1,n,k), 3}, \dots, \mu_{P_3(u,n,k), 3}$
$\mu_{P_3(u,n,k), 1}$	<ul style="list-style-type: none"> Same as $\mu_{P_1(u,n,k), 1}$
$\mu_{P_3(u,n,k), 2}$	<ul style="list-style-type: none"> Same as $\mu_{P_2(u,n,k), 2}$

These preceding algorithms are directly inspired by equation (5.18), theorem 1 and lemma 2.

Theorem 3 *The number of operations needed for $\mu_{P_i(u,n,k),j}$ are given by the following table*

$\mu_{P_1(u,n,k),1}$	$2nk$
$\mu_{P_2(u,n,k),1}$	$2unk$
$\mu_{P_3(u,n,k),1}$	$2nk$
$\mu_{P_1(u,n,k),2}$	$nk^2 + nu\frac{k}{6}(k^2 + 15k + 19) - n\frac{k}{2}(2k^2 + 13k + 15), k > n$ $\frac{1}{3}n(n+1)(2n+1) + nu\frac{k}{6}(k^2 + 15k + 19) - n\frac{k}{2}(2k^2 + 13k + 15), k \leq n$
$\mu_{P_2(u,n,k),2}$	$2\max\{n, k\}^2 + u\frac{k}{6}(k^2 + 15k + 19) - \frac{k}{2}(2k^2 + 13k + 15)$
$\mu_{P_3(u,n,k),2}$	$2\max\{n, k\}^2 + u\frac{k}{6}(k^2 + 15k + 19) - \frac{k}{2}(2k^2 + 13k + 15)$
$\mu_{P_1(u,n,k),3}$	$n(M+1)(\frac{3}{2}u^3 - \frac{3}{2}u^2 - 5u + 7)$
$\mu_{P_2(u,n,k),3}$	$(M+1)\frac{1}{8}(u^4 + 2u^3 - 23u^2 + 34u)$
$\mu_{P_3(u,n,k),3}$	$(M+1)(\frac{3}{2}u^3 - \frac{3}{2}u^2 - 5u + 7)$

Proof $\mu_{P_1(u,n,k), 1}$

2 simple operations are needed to calculate

$$G^{(u)}(p, q) = G^{(u)}(p, q-1) - G^{(u)}(p-1, q-1-u+1) + G^{(u)}(p-1, q), p = 1, \dots, n, q = 1, \dots, k.$$

Hence, $\mu_{P_1(u,n,k), 1}$ requires $2nk$ simple operations. $\mu_{P_2(u,n,k), 2}$

The first point in $\mu_{P_2(u,n,k), 2}$ doesn't require any simple operations. The second point requires $2\max\{n, k\}^2$ simple operations. $2q+1$ simple operations are needed to calculate $G^{(r)}(p, q) = \sum_{l=0}^q G^{(r-1)}(l, q-l) \binom{p}{l}$ for a certain $q = 1, \dots, k$ and $p = 1, \dots, k+1-q$. Hence, the third point requires $(u-3)\sum_{q=1}^k (k+1-q)(2q+1)$ simple operations. $2q+1$ simple operations are needed to calculate $G^{(r)}(n, q) = \sum_{l=0}^q G^{(r-1)}(l, q-l) \binom{n}{l}$ for a certain $r = 3, \dots, u$ and $q = 1, \dots, k$. Hence, the fourth point requires $(u-2)\sum_{q=1}^k (2q+1)$. The total number of simple operations needed for $\mu_{P_2(u,n,k), 2}$ is $2\max\{n, k\}^2 + (u-3)\sum_{q=1}^k (k+1-q)(2q+1) + (u-2)\sum_{q=1}^k (2q+1) = 2\max\{n, k\}^2 + u\frac{k}{6}(k^2 + 15k + 19) - \frac{k}{2}(2k^2 + 13k + 15)$

 $\mu_{P_3(u,n,k), 3}$

The first point in $\mu_{P_3(u,n,k), 3}$ requires 1 simple operation. Calculating $\vec{\xi}^{(1)}(n-1-m, (M-m)(u-1)+s)$ for a certain m and $s = 0, \dots, u-2$ using theorem 2 requires $2(u-1)(u-1)$ simple operations. Calculating $\vec{\xi}^{(r)}(n-1-m, (M-m)(u-1)+s)$ for a certain m and $s = 0, \dots, u-1-r$ requires for $r = 2, \dots, u-1, 3(u-2)(u-r) + 2(u-2)$ simple operations. Hence, the second point requires $(M+1)[2(u-1)^2 + \sum_{r=2}^{u-1} (3(u-2)(u-r) + 2(u-2))]$ simple operations. Calculating $G^{(u)}(n-M+m, m(u-1)+w)$ using corollary 1 for a certain $m = 0, \dots, M$ and $w = 1, \dots, u-1$ requires $(2u-3)$ simple operations. Hence, the third point requires $(M+1)(u-1)(2u-3)$ simple operations. The total number of simple operations needed for $\mu_{P_3(u,n,k), 3}$ is $(M+1)(2(u-1)^2 + \frac{3}{2}(u-2)^2(u-1) + 2(u-2)^2 + (u-1)(2u-3)) = (M+1)(\frac{3}{2}u^3 - \frac{3}{2}u^2 - 5u + 7)$.

 $\mu_{P_1(u,n,k), 2}$

The number of simple operations needed for $\mu_{P_1(u,n,k), 2}$ is n times the number of operations needed for $\mu_{P_2(u,n,k), 2}$ if $\max\{n, k\} = k$, i.e. $nk^2 + nu\frac{k}{6}(k^2 + 15k + 19) - n\frac{k}{2}(2k^2 + 13k + 15)$. Otherwise it is $2\sum_{m=1}^n m^2 + nu\frac{k}{6}(k^2 + 15k + 19) - n\frac{k}{2}(2k^2 + 13k + 15) = \frac{1}{3}n(n+1)(2n+1) + nu\frac{k}{6}(k^2 + 15k + 19) - n\frac{k}{2}(2k^2 + 13k + 15)$.

 $\mu_{P_1(u,n,k), 3}$ The number of simple operations needed for $\mu_{P_1(u,n,k), 3}$ is n times the number of operations

needed for $\mu_{P_3(u,n,k)}, 3$.

$\mu_{P_2(u,n,k)}, 1$

The number of simple operations needed for $\mu_{P_2(u,n,k)}, 1$ is u times the number of operations needed for $\mu_{P_1(u,n,k)}, 1$.

$\mu_{P_2(u,n,k)}, 3$

The number of simple operations needed for $\mu_{P_2(u,n,k)}, 3$ is $\sum_{r=1}^u (M+1)(\frac{3}{2}r^3 - \frac{3}{2}r^2 - 5r + 7) = (M+1)\frac{1}{8}(u^4 + 2u^3 - 23u^2 + 34u)$. ■

We notice, observing theorem 3 that to solve problem $P_1(u,n,k)$, of $\mu_{P_1(u,n,k)}, 1$, $\mu_{P_1(u,n,k)}, 2$ and $\mu_{P_1(u,n,k)}, 3$, $\mu_{P_1(u,n,k)}, 1$ is the most efficient method of the three. Also, to solve problem $P_2(u,n,k)$, all three available methods can be the most efficient depending on the values of u, n and k . To solve problem $P_3(u,n,k)$, the most efficient method is either $\mu_{P_3(u,n,k)}, 1$ or $\mu_{P_3(u,n,k)}, 3$ depending on the values of u, n and k .

5.3 Subsets without consecutive elements in an ordered set

$n \setminus k$	0	1	2	3	4	5	6	7	8	9	10
0	1	0	0	0	0	0	0	0	0	0	0
1	1	1	0	0	0	0	0	0	0	0	0
2	1	2	1	0	0	0	0	0	0	0	0
3	1	3	3	1	0	0	0	0	0	0	0
4	1	4	6	4	0	0	0	0	0	0	0
5	1	5	10	10	3	0	0	0	0	0	0
6	1	6	15	20	12	2	0	0	0	0	0
7	1	7	21	35	31	12	1	0	0	0	0
8	1	8	28	56	65	40	10	0	0	0	0
9	1	9	36	84	120	101	44	6	0	0	0
10	1	10	45	120	203	216	135	40	3	0	0

Table 5.3: Some numerical values of $F^{(u)}(n, k)$ for $u = 4$

5.3.1 Definition of recurrence sequence $F^{(u)}(n, k)$

Let $F^{(u)} : \mathbb{Z} \times \mathbb{Z} \longrightarrow \mathbb{N}$ be the recurrence sequence defined for $u \geq 1$ by

$$F^{(u)}(n, k) = \binom{n}{k}, \quad n < u \text{ or } k < u \text{ and} \quad (5.25)$$

$$F^{(u)}(n, k) = F^{(u)}(n-1, k) + F^{(u)}(n-2, k-1) + \cdots + F^{(u)}(n-u, k-u+1), \quad n \geq u, k \geq u. \quad (5.26)$$

Table 5.3 shows the values of $F^{(4)}(n, k)$ for $n \leq 10, k \leq 10$. The values highlighted are tied by the recurrence relation (5.26) for $u = 4, n = 9$ and $k = 5$.

5.3.2 Interpretation of $F^{(u)}(n, k)$

Call $\hat{F}^{(u)}(n, k)$ the number of subsets of cardinality k , in an ordered set of n elements, that do not have u consecutive elements. It is shown in this section that $F^{(u)}(n, k) = \hat{F}^{(u)}(n, k)$ for $n \in \mathbb{Z}, k \in \mathbb{Z}$. This is true for $n < u$ or $k < u$, since in those cases, it is not possible to have u consecutive elements and thus $\hat{F}^{(u)}(n, k) = \binom{n}{k}$. Furthermore, if we write $K_1(n, k, p)$ for the number of subsets of cardinality k that include the first $p - 1$ elements, do not include the p^{th} element and do not have u consecutive elements, and $K_2(n, k, p)$ for the number of subsets of cardinality k that include the first p elements and do not have u consecutive elements, we have successively:

$$\begin{aligned} \hat{F}^{(u)}(n, k) &= K_1(n, k, 1) + K_2(n, k, 1) \\ &= K_1(n, k, 1) + K_1(n, k, 2) + K_2(n, k, 2) \\ &\quad \cdot \\ &\quad \cdot \\ &\quad \cdot \\ &= K_1(n, k, 1) + K_1(n, k, 2) + \cdots + K_1(n, k, u) + K_2(n, k, u). \end{aligned}$$

Since $K_2(n, k, u) = 0$,

$$\hat{F}^{(u)}(n, k) = K_1(n, k, 1) + K_1(n, k, 2) + \cdots + K_1(n, k, u).$$

Note that $\hat{F}^{(u)}(n-i, k-i+1) = K_1(n, k, i)$, $i = 1, \dots, u$, thus:

$$\hat{F}^{(u)}(n, k) = \hat{F}^{(u)}(n-1, k) + \hat{F}^{(u)}(n-2, k-1) + \cdots + \hat{F}^{(u)}(n-u, k-u+1).$$

Since $F^{(u)}(n, k)$ and $\hat{F}^{(u)}(n, k)$ have same boundary conditions and follow the same recurrence relation, they are identical.

5.3.3 Relating $G^{(u)}(n, k)$ and $F^{(u)}(n, k)$

Theorem 4

$$F^{(u)}(n, k) = G^{(u)}(n-k+1, k), \quad \forall u \geq 1, n \geq 0, k \geq 0 \quad (5.27)$$

Proof 1) Let $n \geq 1$ and $k \geq 0$ such as $n+k < u+1$ or $k < u$.

$$\begin{aligned} G^{(u)}(n, k) &= G^{(u)}(n-1, k) + \cdots + G^{(u)}(n-1, k-u+1) \\ &= G^{(u)}(n-1, k) + \cdots + G^{(u)}(n-1, k-u+1) + G^{(u)}(n-1, k-u) \end{aligned}$$

Indeed, we note that if $k < u$, then $G^{(u)}(n-1, k-u) = 0$ and if $n+k < u+1$, then $u-k > n-1$ and $G^{(u)}(n-1, k-u) = 0$ also.

Thus,

$$G^{(u)}(n, k) = G^{(u)}(n-1, k) + G^{(u)}(n, k-1). \quad (5.28)$$

Let $H(n, k) = G^{(u)}(n-k+1, k)$, then $H(n-1, k) + H(n-1, k-1) = G^{(u)}(n-k, k) + G^{(u)}(n-k+1, k-1)$.

By equation (5.28), if $n \geq k, k \geq 0$ and $n < u$ (which can be written $n-k+1+k < u+1$) or $k < u$,

$$H(n, k) = H(n-1, k) + H(n-1, k-1). \quad (5.29)$$

Furthermore, for $n < k$, $\binom{n}{k} = 0$ and $G^{(u)}(n-k+1, k) = 0$

So $G^{(u)}(n-k+1, k) = \binom{n}{k}$ for $n \geq 0, k \geq 0$ and $n < u$ or $k < u$.

2)

Also, for $n \geq u$ and $k \geq u$,

$$\begin{aligned} &H(n, k) \\ &= G^{(u)}(n-k+1, k) \\ &= G^{(u)}(n-k, k) + \cdots + G^{(u)}(n-k, k-u+1) \\ &= H(n-1, k) + \cdots + H(n-u, k-u+1). \end{aligned}$$

We finally find that $F^{(u)}(n, k) = H(n, k) = G^{(u)}(n-k+1, k)$ ■

5.3.4 How to calculate values of $F^{(u)}(n, k)$

Using theorem 4, the problem of calculating $F^{(u)}(n, k)$ is transformed into the problem of calculating $G^{(u)}(n, k)$ by one subtraction and one addition.

5.4 Conclusion

We have studied two kinds of bi-indexed recurrence sequences $G^{(u)}$ and $F^{(u)}$. We have shown that there are several ways of calculating values of these recurrence sequences. Depending on which values are wanted one or the other way is more efficient. In chapter 6, we will be interested in calculating the jamming probability for a simple model of granular flow in a hopper (model SPM-C). The recurrence sequence $F^{(u)}$ will be necessary in this calculation. The work done in this chapter and the next one is a step towards understanding how to study efficiently the jamming behavior for less simple models, one may think of DEM for example.

If there is a problem you can't solve, then there is an easier problem you can solve: find it.
– George Pólya

Chapter 6

Simple models

6.1 Introduction

In practice, for complex systems like those simulated with DEM, it is difficult even to approximate the jamming probability or other quantities related to jamming as functions of global parameters. We resort, in chapter 7, to studying some such quantities by simulation. In this chapter we study some more simple models. After defining the models, we calculate analytically the jamming probability or the average time before jamming when jamming occurs, something that would be very difficult to accomplish for DEM. The simple models will be of two kinds: discrete and continuous, kinds in which the particles move respectively on a discrete and continuous set of sites. These particle models are non-interacting as opposed to DEM, in which grains interact. In chapter 8, we will compare the jamming behavior of these simple models and of DEM.

6.2 Model SPM-D

6.2.1 Description

In model SPM-D (discrete version), the hopper, a grid of sites, has $M - \tau$ horizontal lines, indexed $\tau + 1, \dots, M$ from bottom to top. The number of sites in a line is equal to its index. τ is called the hole size (see Fig. 6.1a). Initially, a random number of particles are placed on the grid, each site having probability $\frac{n}{m}$ of receiving a particle, where m is the number of sites and n a given integer. Note that the initial placement of a particle on a site is a Bernoulli variable. Consequently, the number of particles has a binomial distribution with average n . The flow is defined as follows: at each iteration, if a line is not totally filled, the particles on it move to a site, chosen randomly, on the line below (see Figures 6.1b, 6.1c, 6.1d) except for line $\tau + 1$, the lowest line, where the particles exit the grid, (see Figures 6.1c, 6.1d). If a line is totally filled, all the particles on the grid cease to move and we say that jamming takes place (Fig. 6.1d).

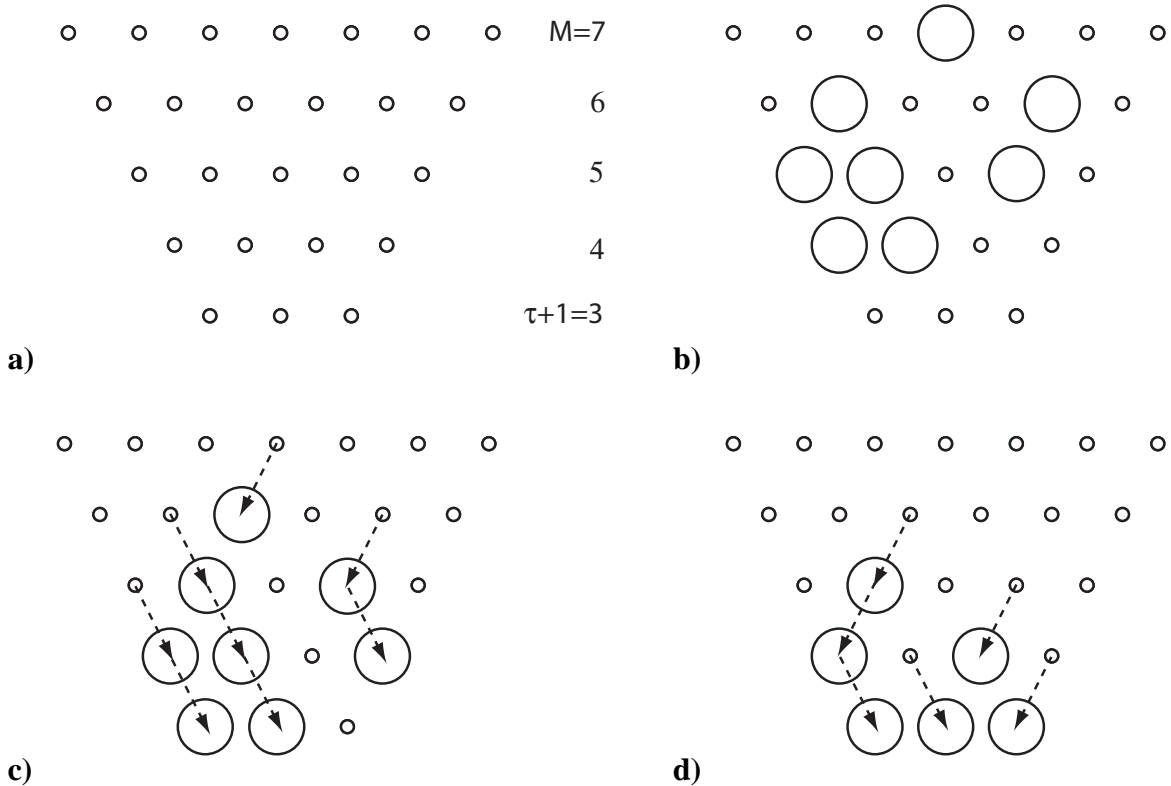


Figure 6.1: An example for model SPM-D: a) Grid b) Iteration 0 (initial configuration) c) Iteration 1 d) Iteration 2 (jammed configuration); arrows show the movement from the precedent configuration

6.2.2 Jamming probability

Lemma 3 *In model SPM-D, an initial configuration will lead to jamming if and only if it has a line with strictly more than τ particles.*

Proof

If the initial configuration has a line with more than τ particles, either jamming does take place before these particles reach line $\tau + 1$ or jamming takes place when they are on line $\tau + 1$. If all the lines in the initial configuration have less than $\tau + 1$ particles, then all the lines have less than $\tau + 1$ particles at all iterations and jamming does not take place. ■

In the following, we name F_j^i the event that there are initially j particles on line i and $F_{\leq j}^i$ the event that there are initially no more than j particles on line i . We call J the event that jamming takes place.

Theorem 5 *For model SPM-D,*

$$P\{F_j^i\} = \binom{i}{j} \left(\frac{n}{m}\right)^j \left(1 - \frac{n}{m}\right)^{i-j}$$

and the probability that the system will jam is

$$P\{J\} = 1 - \prod_{i=\tau+1}^M \sum_{j=0}^{\tau} P\{F_j^i\}.$$

Proof

$P\{J\} = 1 - P\{J^c\}$ where J^c is the event that jamming does not take place. $P\{J^c\} = P\{\cap_{i=\tau+1}^M F_{\leq \tau}^i\} = \prod_{i=\tau+1}^M P\{F_{\leq \tau}^i\}$ since $\{F_{\leq \tau}^i\}_{i=\tau+1}^M$ is independent. $P\{F_{\leq \tau}^i\} = P\{\cup_{j=0}^{\tau} F_j^i\} = \sum_{j=0}^{\tau} P\{F_j^i\}$ since $\{F_j^i\}_{j=0}^{\tau}$ is disjoint. $P\{F_j^i\} = \binom{i}{j} \left(\frac{n}{m}\right)^j \left(1 - \frac{n}{m}\right)^{i-j}$ since there are $\binom{i}{j}$ ways of placing j particles on line i and such a configuration appears with probability $\left(\frac{n}{m}\right)^j \left(1 - \frac{n}{m}\right)^{i-j}$. ■

6.2.3 Average time before jamming when jamming occurs

In the following, we name Y the random variable that gives the iteration at which the system jams.

Theorem 6 *The probability that the system will not jam before iteration y is*

$$P\{Y \geq y\} = \prod_{i=\tau+1}^M P\{F_{\leq \max\{i-y, \tau\}}^i\}.$$

Proof

The system will not jam before y iif $\forall i = \tau + 1, \dots, M$, there are at most $\max\{i - y, \tau\}$ particles on line i .

Suppose for each line i there are at most $\max\{i - y, \tau\}$ particles and that the system jams before y . Then, there is a full line $i^* > \tau$ at iteration $l < y$. At iteration 0, there were i^* particles on line $i_2 = i^* + l$, or $i_2 - l$ particles on line i_2 . Since $l < y$, there are more than $i_2 - y$ particles in line i_2 at iteration 0. Since $i^* > \tau$ there are more than τ particles on line i_2 at iteration 0. Then, there are more than $\max\{i_2 - y, \tau\}$ on line i_2 at iteration 0 which contradicts our assumption.

Suppose the system will not jam before y . If there are more than $\max\{i - y, \tau\}$ particles on a line i , then the system will jam, which contradicts our supposition. ■

Corollary 2 *The probability that the system will jam at y is*

$$\begin{aligned} P\{Y = y\} \\ = \prod_{i=\tau+1}^M P\{F_{\leq \max\{i-y, \tau\}}^i\} - \prod_{i=\tau+1}^M P\{F_{\leq \max\{i-(y+1), \tau\}}^i\} \end{aligned}$$

Proof

Proof results from the preceding theorem and that $P\{Y = y\} = P\{Y \geq y\} - P\{Y \geq y+1\}$. ■

6.3 Model SPM-C

6.3.1 Description

We define model SPM-C as follows: the hopper is a circular sector of radius R and internal angle β , see FIG. 6.2.

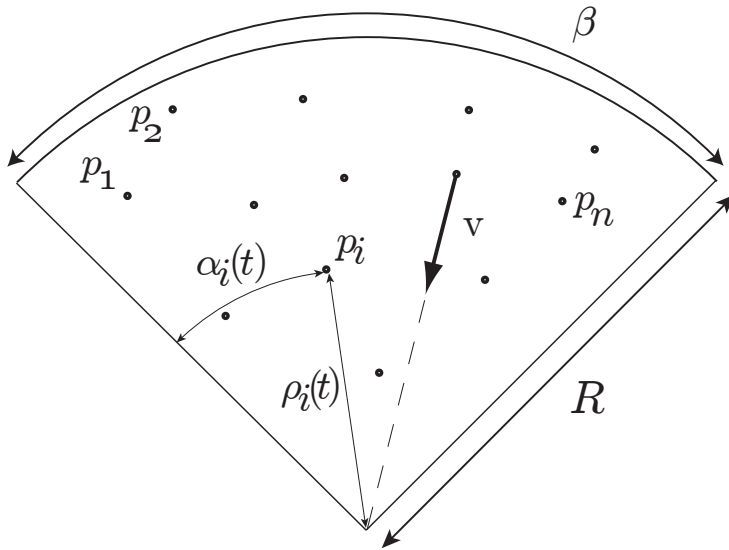


Figure 6.2: Model SPM-C

Two versions of the insertion of particles are considered. There are n point particles $\{p_1, p_2, \dots, p_n\}$ to be inserted in the hopper. In the first version, the particles are placed uniformly in the hopper (this version will only be used in Chapter 8). In the second, for each particle an angle $\alpha_i(0)$ and a radius $\rho_i(0)$ are chosen uniformly in $[0, \beta]$ and $[0, R]$. The particle is placed at the position in the hopper with polar coordinates $(\alpha_i(0), \rho_i(0))$ with respect to the hopper, see FIG. 6.2. Particles move with constant velocity \vec{v}_i toward the center of the hopper. All particles have the same speed v , i.e. $\|\vec{v}_i\| = v, \forall i = 1, \dots, n$. A positive integer τ is chosen to represent the hole size. Let us give the position at time t of a particle p_i by its polar coordinates, angle $\alpha_i(t)$ and radius $\rho_i(t)$, with respect to the disc containing the hopper. Let $\{q_1(t), \dots, q_n(t)\}$ be the radii $\{\rho_1(t), \dots, \rho_n(t)\}$ ordered increasingly. We say that the system jams at time \bar{t} , the smallest time for which $\tau + 1$ grains simultaneously try to exit, more precisely

$$\bar{t} = \inf\{t \mid \exists k \mid q_k(\bar{t}) = 0 \text{ and } q_{i+1}(\bar{t}) - q_i(\bar{t}) \leq \epsilon \forall i = k, \dots, k + \tau - 1\} \quad (6.1)$$

where ϵ is a parameter in $[0, 1]$. The jamming probability increases with ϵ . Thus, ϵ may be thought of as representing friction.

6.3.2 Order statistics

The initial placement of particles in model SPM-C, is equivalent to placing points uniformly on a interval. The jamming condition involves ordering the points according to their distance to the center of the circular sector. The subject that deals with placing points randomly on an interval is order statistics, the name indicating that the points are ordered. In order statistics, problems that are dealt with are, for example: finding the statistical distribution of certain functions of the points or the gaps, or spacings, between the points, finding the moments of these quantities, the asymptotic analysis of these results or also the applications of order statistic theories. We give here a choice of works on order statistics. A complete survey of the subject here is unrealistic. Indeed, MathSciNet, the mathematical articles search engine reports some 1000 papers on the subject in the last ten years. According to Moran [Moran, 1947], the theory of distributions related with the random division of an interval goes back to the 19th century. Lévy [Lévy, 1939] studied the smallest and largest gap. Garwood [Garwood, 1940] discussed an application of order statistics to vehicular-controlled traffic signals. Greenwood [Greenwood, 1946] pointed out the interest of sum of the squares of the gaps in the statistical study of infectious diseases. This problem has been discussed by Moran [Moran, 1947]. Now, consider v_1, \dots, v_{n+1} the gaps induced by placing n points uniformly on an interval. Sherman [Sherman, 1950] studied the statistic

$$\omega_n = \frac{1}{2} \sum_{i=1}^{n+1} \left| v_i - \frac{1}{n+1} \right|. \quad (6.2)$$

Darling [Darling, 1953] studied the statistic

$$W_n = \sum_{j=1}^{n+1} h_j(v_j) \quad (6.3)$$

for quite arbitrary functions h_j . Weiss studied the limiting joint distribution of the largest and smallest gaps [Weiss, 1959] and the joint distribution of the k -smallest sample spacings [Weiss, 1969]. Holst [Holst, 1980] gives new proofs of old results and some new results. This review can not be considered complete, further bibliographic research, in particular concerning more recent articles, is left to the interested reader. One can refer to [David, 1981] and [Arnold et al., 1992] for a thorough treatment of the basics of order statistics.

6.3.3 Jamming probability

We have the analog of lemma 3 for SPM-C which describes the initial conditions that will lead to jamming. In the following, we write $v_i = q_{i+1}(0) - q_i(0)$, $i = 1, \dots, n-1$.

Lemma 4 *In SPM-C with the second version of the insertion of grains, an initial configuration will lead to jamming if and only if $\exists i \in \{1, \dots, n-\tau\} \mid v_i \leq \varepsilon, \dots, v_{i+\tau-1} \leq \varepsilon$.*

Proof

Since the speed of the particles is constant $\exists t \geq 0, i = 1, \dots, n-1 \mid q_{i+1}(t) - q_i(t) \leq \varepsilon$ iff $\exists i = 1, \dots, n-1 \mid q_{i+1}(0) - q_i(0) \leq \varepsilon$ ■

Lemma 5 Let A_1, \dots, A_{n-1} be subsets of $[0, R]$ and σ a permutation of $\{1, \dots, n-1\}$. We have

$$\begin{aligned} P\{v_1 \in A_1, \dots, v_{n-1} \in A_{n-1}\} &= \\ P\{v_{\sigma(1)} \in A_1, \dots, v_{\sigma(n-1)} \in A_{n-1}\} &. \end{aligned}$$

Proof

Let ρ_1, \dots, ρ_n be the ordered initial distances between the particles and the center of the circular sector. Consider the change of variables defined by

$$v_0 = \rho_1, v_1 = \rho_2 - \rho_1, \dots, v_{n-1} = \rho_n - \rho_{n-1}.$$

Note that the Jacobian J of this change of variables is 1.

$$\begin{aligned} &P\{v_1 \in A_1, \dots, v_{n-1} \in A_{n-1}\} \\ &= P\{\rho_2 - \rho_1 \in A_1, \dots, \rho_n - \rho_{n-1} \in A_{n-1}\} \\ &= \frac{1}{R^n} \int_{\rho_2 - \rho_1 \in A_1, \dots, \rho_n - \rho_{n-1} \in A_{n-1}} d\rho_1 \dots d\rho_n \quad (\rho_i \sim U[0, R]) \\ &= \frac{1}{R^n} \int_{v_1 \in A_1, \dots, v_{n-1} \in A_{n-1}} dv_1 \dots dv_{n-1} \quad (J = 1) \\ &= \frac{1}{R^n} \int_{v_{\sigma(1)} \in A_1, \dots, v_{\sigma(n-1)} \in A_{n-1}} dv_1 \dots dv_{n-1} \\ &= P\{v_{\sigma(1)} \in A_1, \dots, v_{\sigma(n-1)} \in A_{n-1}\} \end{aligned}$$

■

Lemma 6 Consider SPM-C with the second version of the insertion of grains and $k \in \{0, \dots, n-1\}$. Call $P_k(n, \varepsilon, R)$ the probability $P\{v_1 \leq \varepsilon, \dots, v_k \leq \varepsilon, v_{k+1} > \varepsilon, \dots, v_{n-1} > \varepsilon\}$. We have

$$P_k(n, \varepsilon, R) = (-1)^k \frac{1}{R^n} \sum_{l=0}^k \binom{k}{l} (-1)^l (R - (n-1-l)\varepsilon)^n.$$

Proof

Let $A_k = \{v_{k+1} > \varepsilon, \dots, v_{n-1} > \varepsilon\}$.

$$\begin{aligned} P\{A_k\} &= P\{A_k \cap \bigcup_{\sigma \in \mathcal{P}_n} \{\rho_{\sigma(1)} \leq \rho_{\sigma(2)} \leq \dots \leq \rho_{\sigma(n)}\}\} \\ &= \sum_{\sigma \in \mathcal{P}_n} P\{A_k \cap \{\rho_{\sigma(1)} \leq \rho_{\sigma(2)} \leq \dots \leq \rho_{\sigma(n)}\}\} \end{aligned}$$

(the sets of $\{\{\rho_{\sigma(1)} \leq \rho_{\sigma(2)} \leq \dots \leq \rho_{\sigma(n)}\}\}_{\sigma \in \mathcal{P}_n}$ have null measure intersections)

$$\begin{aligned} &= n! P\{A_k \cap \{\rho_1 \leq \rho_2 \leq \dots \leq \rho_n\}\} \\ &= n! P\left\{ \{\rho_1 \leq \rho_2 \leq \dots \leq \rho_n\} \cap \{\rho_{i+1} - \rho_i > \varepsilon \ \forall i = k+1, \dots, n-1\} \right\} \\ &= n! \int_0^{R-(n-k-1)\varepsilon} \int_{\rho_1}^{R-(n-k-1)\varepsilon} \dots \int_{\rho_k}^{R-(n-k-1)\varepsilon} \int_{\rho_{k+1}+\varepsilon}^{R-(n-k-2)\varepsilon} \dots \int_{\rho_{n-2}+\varepsilon}^{R-\varepsilon} \int_{\rho_{n-1}+\varepsilon}^R \frac{1}{R^n} d\rho_n \dots d\rho_1 \end{aligned}$$

To calculate this last integral expression, we first prove by induction that

$$I_i = \int_{\rho_i+\varepsilon}^{R-(n-i-1)\varepsilon} \dots \int_{\rho_{n-2}+\varepsilon}^{R-\varepsilon} \int_{\rho_{n-1}+\varepsilon}^R d\rho_n \dots d\rho_{i+1} = \frac{1}{(n-i)!} (R - (\rho_i + (n-i)\varepsilon))^{n-i}, \quad (6.4)$$

$\forall i = k+1, \dots, n-1$.

- The induction proposition is true for $i = n-1$: $\int_{\rho_{n-1}+\varepsilon}^R d\rho_n = R - (\rho_{n-1} + \varepsilon)$.
- We suppose the induction proposition true for i and show that it is then true for $i-1$:

$$\begin{aligned} I_{i-1} &= \int_{\rho_{i-1}+\varepsilon}^{R-(n-i)\varepsilon} I_i d\rho_i \\ &= \int_{\rho_{i-1}+\varepsilon}^{R-(n-i)\varepsilon} \frac{1}{(n-i)!} (R - (\rho_i + (n-i)\varepsilon))^{n-i} d\rho_i \\ &= \frac{-1}{(n-i+1)!} (R - (\rho_i + (n-i)\varepsilon))^{n-i+1} \Big|_{\rho_{i-1}+\varepsilon}^{R-(n-i)\varepsilon} \\ &= \frac{1}{(n-i+1)!} (R - (\rho_{i-1} + (n-i+1)\varepsilon))^{n-i+1}. \end{aligned}$$

Secondly, we prove by induction that

$$\begin{aligned} I'_i &= \int_{\rho_i}^{R-(n-k-1)\varepsilon} \dots \int_{\rho_k}^{R-(n-k-1)\varepsilon} \int_{\rho_{k+1}+\varepsilon}^{R-(n-k-2)\varepsilon} \dots \int_{\rho_{n-2}+\varepsilon}^{R-\varepsilon} \int_{\rho_{n-1}+\varepsilon}^R \frac{1}{R^n} d\rho_1 \dots d\rho_{i+1} \\ &= \frac{1}{(n-i)!} (R - (\rho_i + (n-k-1)\varepsilon))^{n-k-1}. \end{aligned} \quad (6.5)$$

- The induction proposition is true for $i = k$, indeed:

$$\text{Equation (6.4) implies } I_{k+1} = \frac{1}{(n-k-1)!} (R - (\rho_{k+1} + (n-k-1)\varepsilon))^{n-k-1}.$$

Since

$$I'_k = \int_{\rho_k}^{\rho_k + \varepsilon} I_{k+1} d\rho_{k+1},$$

$$I'_k = \frac{-1}{(n-k)!} \left(R - (\rho_{k+1} + (n-k-1)\varepsilon) \right)^{n-k} \Big|_{\rho_k}^{R-(n-k-1)\varepsilon}.$$

We find that

$$I'_k = \frac{1}{(n-k)!} \left(R - (\rho_k + (n-k-1)\varepsilon) \right)^{n-k}.$$

- $I'_{i-1} = \int_{\rho_{i-1}}^{R-(n-k-1)\varepsilon} I'_i d\rho_i.$

If the induction proposition is true for i , then

$$\begin{aligned} I'_{i-1} &= \int_{\rho_{i-1}}^{R-(n-k-1)\varepsilon} \frac{1}{(n-i)!} \left(R - (\rho_i + (n-k-1)\varepsilon) \right)^{n-i} d\rho_i \\ &= \frac{-1}{(n-i+1)!} \left(R - (\rho_i + (n-k-1)\varepsilon) \right)^{n-i+1} \Big|_{\rho_{i-1}}^{R-(n-k-1)\varepsilon} \\ &= \frac{1}{(n-i+1)!} \left(R - (\rho_{i-1} + (n-k-1)\varepsilon) \right)^{n-i+1}, \end{aligned}$$

and the induction proposition is true for $i-1$.

Finally, $P\{A_k\} = \frac{n!}{R^n} \int_0^{R-(n-k-1)\varepsilon} I'_1 d\rho_1$

$$\begin{aligned} &= \frac{n!}{R^n} \int_0^{R-(n-k-1)\varepsilon} \frac{1}{(n-1)!} \left(R - (\rho_1 + (n-k-1)\varepsilon) \right)^{n-1} d\rho_1 \\ &= \frac{(R-(n-k-1)\varepsilon)^n}{R^n} \end{aligned}$$

Now we prove the lemma by induction

- The lemma is true for $k=0$, indeed:

$$\begin{aligned} P\{v_1 > \varepsilon, \dots, v_{n-1} > \varepsilon\} &= P\{A_0\} \\ &= \frac{(R-(n-1)\varepsilon)^n}{R^n} = (-1)^0 \frac{1}{R^n} \sum_{l=0}^0 \binom{0}{l} (-1)^l (R-(n-1-l)\varepsilon)^n. \end{aligned}$$

- Suppose the induction proposition is true up to k ,

Let us write $B = P\{v_1 \leq \varepsilon, \dots, v_{k+1} \leq \varepsilon, v_{k+2} > \varepsilon, \dots, v_{n-1} > \varepsilon\}$.

$$P\{A_{k+1}\} = \sum_{r=0}^{k+1} \binom{k+1}{r} P\{v_1 \leq \varepsilon, \dots, v_r \leq \varepsilon, v_{r+1} > \varepsilon, \dots, v_{n-1} > \varepsilon\}.$$

By the induction hypothesis,

$$\begin{aligned} P\{A_{k+1}\} &= \sum_{r=0}^k \binom{k+1}{r} (-1)^r \frac{1}{R^n} \sum_{l=0}^r \binom{r}{l} (-1)^l (R-(n-1-l)\varepsilon)^n + B \\ &= \sum_{l=0}^k \sum_{r=l}^k \binom{k+1}{r} (-1)^r \frac{1}{R^n} \binom{r}{l} (-1)^l (R-(n-1-l)\varepsilon)^n + B \\ &= \frac{1}{R^n} \sum_{l=0}^k (-1)^l (R-(n-1-l)\varepsilon)^n \sum_{r=l}^k \binom{k+1}{r} (-1)^r \binom{r}{l} + B. \end{aligned}$$

We accept without proof that $\sum_{r=l}^k \binom{k}{r} (-1)^r \binom{r}{l} = 0, \forall k, l \in \mathbb{N}^*, l \leq k$.

$$\begin{aligned}
& \text{Using this, } \sum_{r=l}^k \binom{k+1}{r} (-1)^r \binom{r}{l} = \sum_{r=l}^{k+1} \binom{k+1}{r} (-1)^r \binom{r}{l} - (-1)^{k+1} \binom{k+1}{l} \\
& = 0 - (-1)^{k+1} \binom{k+1}{l}, \text{ consequently,} \\
& P\{v_1 \leq \epsilon, \dots, v_{k+1} \leq \epsilon, v_{k+2} > \epsilon, \dots, v_{n-1} > \epsilon\} \\
& = P\{A_{k+1}\} + (-1)^{k+1} \frac{1}{R^n} \sum_{l=0}^k \binom{k+1}{l} (-1)^l (R - (n-1-l)\epsilon)^n \\
& = (-1)^{k+1} \frac{1}{R^n} \sum_{l=0}^{k+1} \binom{k+1}{l} (-1)^l (R - (n-1-l)\epsilon)^n. \quad \blacksquare
\end{aligned}$$

Theorem 7 For SPM-C with the second version of the insertion of grains, the probability that the system will jam is

$$\sum_{k=\tau}^{n-1} \left(\binom{n-1}{k} - F^{(\tau)}(n-1, k) \right) P_k(n, \epsilon, R)$$

where $F^{(\tau)}$ is as in section 5.3.

Proof

The probability that the system will jam is

$$\begin{aligned}
& P\{\exists i \in \{1, \dots, n-\tau\} \mid v_i \leq \epsilon, \dots, v_{i+\tau-1} \leq \epsilon\} \text{ (by lemma 4)} \\
& = P\{\{\exists i \in \{1, \dots, n-\tau\} \mid v_i \leq \epsilon, \dots, v_{i+\tau-1} \leq \epsilon\} \cap \\
& \quad \{\exists I \subseteq \{1, \dots, n-1\} | card(I) = k, v_i \leq \epsilon, \forall i \in I, v_i > \epsilon, \forall i \in \{1, \dots, n-1\} \setminus I\}\} \\
& = \sum_{I \subseteq \{1, \dots, n-1\}, card(I)=k} P\{\{\exists i \in \{1, \dots, n-\tau\} \mid v_i \leq \epsilon, \dots, v_{i+\tau-1} \leq \epsilon\} \cap \\
& \quad \{v_i \leq \epsilon, \forall i \in I, v_i > \epsilon, \forall i \in \{1, \dots, n-1\} \setminus I\}\} \\
& = \sum_{k=\tau}^{n-1} M^{(\tau)}(n-1, k) P_k(n, \epsilon, R) \\
& \quad \text{(by lemma 5, } M^{(u)}(n, k) \text{ being the number of subsets of cardinality } k \text{ in a ordered set} \\
& \quad \text{of } n \text{ elements, that has } u \text{ consecutive elements),} \\
& = \sum_{k=\tau}^{n-1} \left(\binom{n-1}{k} - F^{(\tau)}(n-1, k) \right) P_k(n, \epsilon, R). \quad \blacksquare
\end{aligned}$$

6.4 Conclusion

We have studied simple models of granular flow in a hopper to understand how to find analytical expressions for the jamming probability or other similar quantities. More generally, the underlying problem is how to calculate these quantities for a given model. We have shown that this mathematical problem can be quite complex, for example requiring a theory on recurrence sequences. The work done in this chapter is a step in understanding how to calculate quantities related to jamming for more complex models. A next step could perhaps be to introduce an interaction between grains in the simple models studied.

Computers are incredibly fast, accurate, and stupid. Human beings are incredibly slow, inaccurate, and brilliant. Together they are powerful beyond imagination.
– Albert Einstein

Chapter 7

2D DEM simulations of granular jamming in a hopper

7.1 Introduction

Part of the material found in the two following chapters has been published in [Tsukahara et al., 2009].

In this chapter, we present the 2D DEM simulations of granular flow in a hopper we carried out on the Greedy Pool, a grid computing facility at EPFL, based on the Condor grid computing software [University of Wisconsin Madison], that allowed a average factor 30 speed up compared to a unique processor. The goal was to study the influence of friction, hole size, number of grains, grain length, hopper angle on the jamming probability, the average time before jamming when jamming occurs and the average number of grains that fall through the hole when jamming occurs.

7.2 Influence of friction, hole size, number of grains

7.2.1 Setup

To study the influence of friction, hole size and number of grains on the jamming probability, simulations were carried out as follows. The hopper is a truncated isosceles triangle, with its apex pointing downwards, placed in a rectangular receptacle, see Fig. 7.1. Hopper angle ϕ was taken equal to $\pi/3$. The hole size was chosen equal σ times the grain diameter, with σ taking values 2 or 3. The hopper height H was chosen for each hole size so that a fixed number of disc-shaped grains could be introduced without overlapping. One of the goals is to compare values

of the jamming probability for different choices of parameters. For a meaningful comparison of two values, these should differ more than the error made on estimating the jamming probability. For this reason, we chose the parameters so as to have a wide range of values of the jamming probability in $[0, 1]$. Therefore, the number of grains used and hopper dimensions differed for $\sigma = 2$ and $\sigma = 3$. Table 7.1 gives the hopper dimensions for each hole size.

$\sigma = 2$	$\sigma = 3$
$L = 0.623 \text{ m}, H = 0.470 \text{ m}, H' = 1.0 \text{ m}$	$L = 1.063 \text{ m}, H = 0.817 \text{ m}, H' = 1.5 \text{ m}$

Table 7.1: Hopper dimensions for $\sigma = 2$ and $\sigma = 3$.

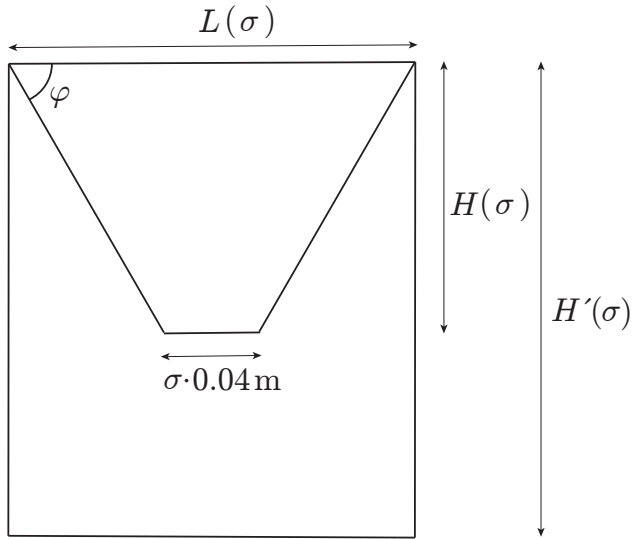


Figure 7.1: Scheme of the hopper.

Table 7.2 shows how the number of grains N and the Coulomb friction coefficient μ were varied for each hole size. For each choice of parameters about $M = 160$ simulations were run.

$\sigma = 2$	$(N, \mu) \in \{2, 4, 6, \dots, 50, 80\} \times \{0.1, 0.125, 0.15, 0.175, 0.2\}$
$\sigma = 3$	$(N, \mu) \in \{5, 10, 15, \dots, 125, 250\} \times \{0.2, 0.3, 0.4, 0.5, 0.6\}$

Table 7.2: Planning of 2D DEM simulations to study the influence of friction, hole size and number of grains on the jamming probability.

In each simulation, the N grains of diameter 0.04 m , density $2500 \text{ kg} \cdot \text{m}^{-2}$ and mass m are inserted sequentially in the hopper: the center position of each grain is chosen randomly in the hopper with a uniform spacial distribution. A grain is inserted in this position only if it does not overlap with any previously inserted ones, otherwise the choice of the position is iterated until the grain can be properly inserted. Starting from these initial positions and initial speeds equal to zero, DEM is run with the outlet closed until the grains settle down. We consider that the grains have settled down when the total kinetic energy stays below 0.09 J for 2500 iterations. The outlet is then opened and the simulation is run until the grains flow through the hopper or jam. Jamming is considered to have occurred when there is at least one grain above the hole

and the total kinetic energy stays below 0.09 J for 2500 iterations. Flow is considered to have occurred when all the grains are below the hole.

7.2.2 Results and discussion

Fig. 7.2 shows snapshots of a simulation for which jamming has occurred.

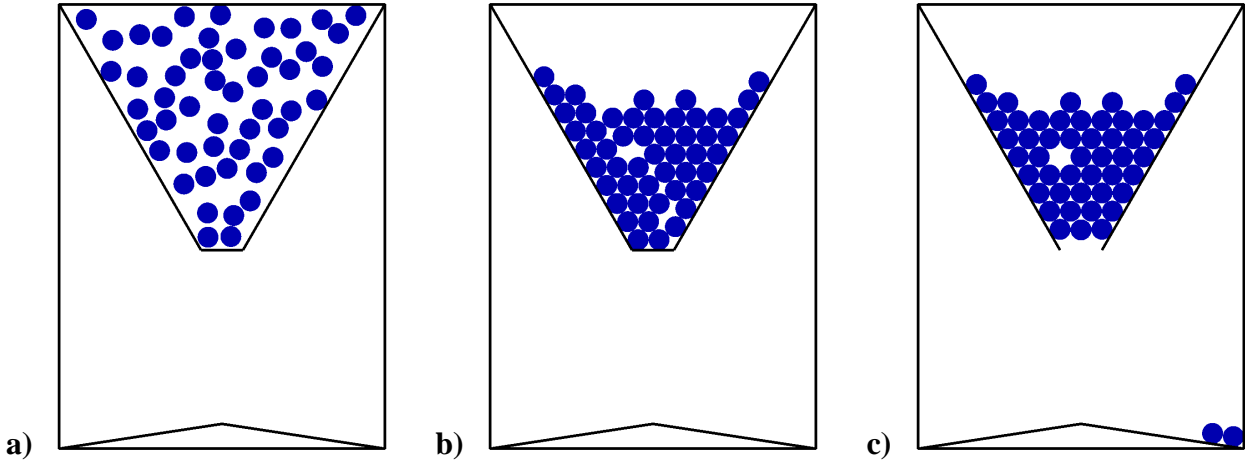


Figure 7.2: Snapshots of a simulation for which jamming has occurred: a) Initial insertion of grains b) Settled configuration before hole opening c) Jammed configuration.

Recall that for each choice of parameters (N, σ, μ) we ran $M = 160$ simulations. Call $S_i(N, \sigma, \mu)$ the i^{th} simulation with parameters (N, σ, μ) . The outcome,

$$\xi_i(N, \sigma, \mu) = \begin{cases} 1 & \text{if jamming has occurred} \\ 0 & \text{otherwise} \end{cases} \quad (7.1)$$

was recorded for every simulation $S_i(N, \sigma, \mu)$.

For each choice of parameters, the jamming probability was calculated by

$$J_{DEM}(N, \sigma, \mu) = \frac{\sum_{i=1}^M \xi_i(N, \sigma, \mu)}{M}. \quad (7.2)$$

An estimator of the standard deviation of J_{DEM} was calculated by

$$J_{DEM}^{(stddev)}(N, \sigma, \mu) = \sqrt{\frac{\sum_{i=1}^M (J_{DEM}(N, \sigma, \mu) - \xi_i(N, \sigma, \mu))^2}{(M-1)M}}. \quad (7.3)$$

For $S_i(N, \sigma, \mu)$, at times t such as $t = 0.01 \cdot k$ s, $k \in \mathbb{N}$ and t smaller than the end time of the simulation the positions

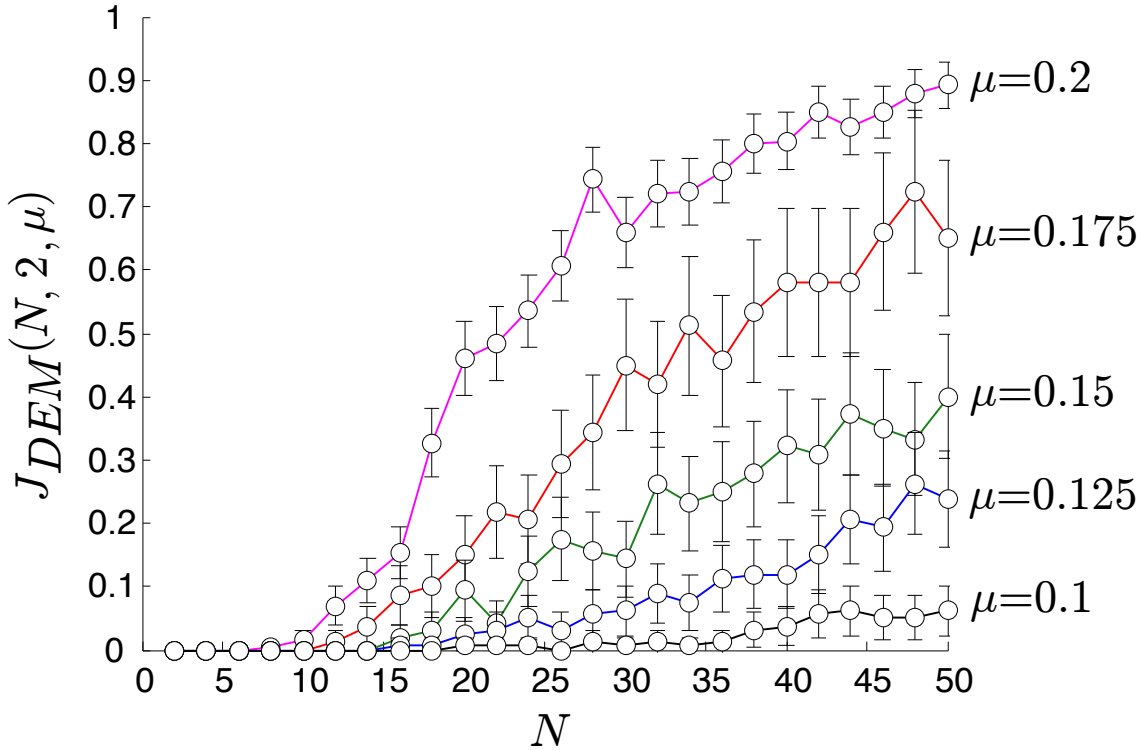


Figure 7.3: Jamming probability $J_{DEM}(N, \sigma, \mu)$ for $\sigma = 2$ and for varying N and μ . Estimators of the standard deviations $J_{DEM}^{(stddev)}(N, \sigma, \mu)$ are shown as bars.

$$x_{ij}(N, \sigma, \mu)(t) = \begin{pmatrix} x_{ij}(N, \sigma, \mu)_1(t) \\ x_{ij}(N, \sigma, \mu)_2(t) \end{pmatrix}, \quad j = 1, \dots, N \quad (7.4)$$

and velocities

$$v_{ij}(N, \sigma, \mu)(t), \quad j = 1, \dots, N \quad (7.5)$$

of the centers of gravity of the grains were recorded.

This allowed to calculate for $S_i(N, \sigma, \mu)$, the following kinetic energy functions:

- the average total energy of the grains,

$$E_i^{(1)}(N, \sigma, \mu)(t) = \frac{1}{N} \sum_{j=1}^N \frac{m}{2} v_{ij}(N, \sigma, \mu)(t)^2, \quad (7.6)$$

- and the average energy of the grains above the hole,

$$E_i^{(2)}(N, \sigma, \mu)(t) = \frac{\sum_{j=1}^N \frac{m}{2} v_{ij}(N, \sigma, \mu)(t)^2 \mathbf{1}_{x_{ij}(N, \sigma, \mu)_2(t) > H'(\sigma) - H(\sigma)}}{\sum_{j=1}^N \mathbf{1}_{x_{ij}(N, \sigma, \mu)_2(t) > H'(\sigma) - H(\sigma)}}, \quad (7.7)$$

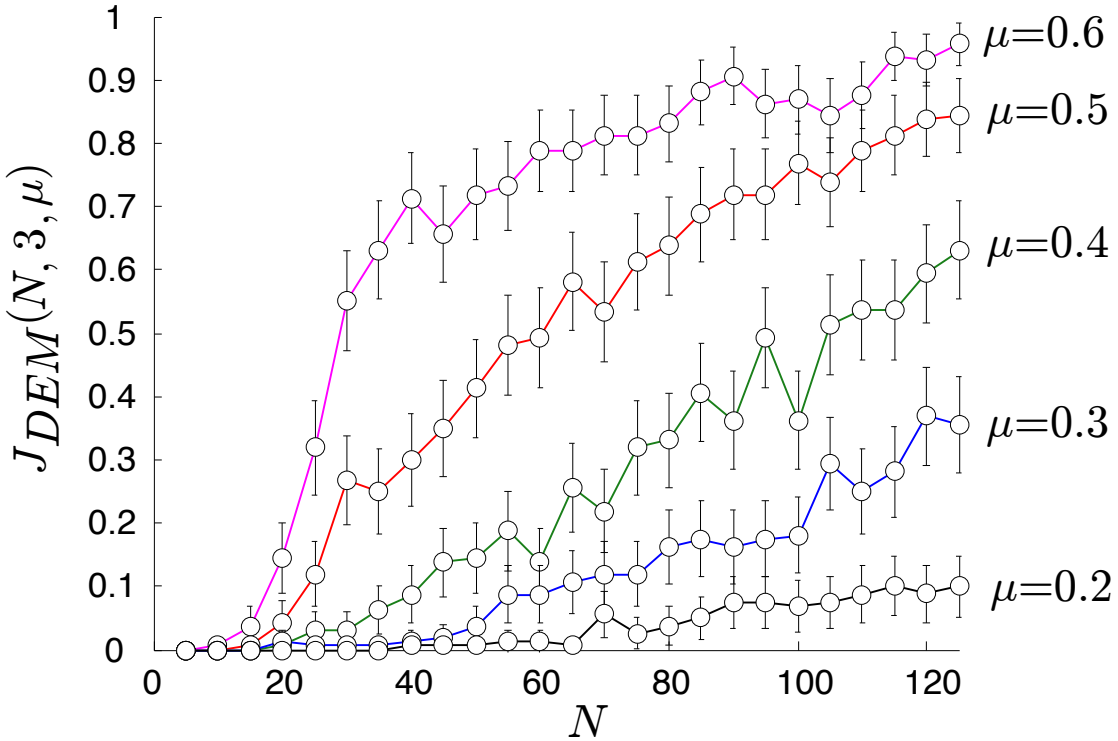


Figure 7.4: Jamming probability $J_{DEM}(N, \sigma, \mu)$ for $\sigma = 3$ and for varying N and μ . Estimators of the standard deviations $J_{DEM}^{(stddev)}(N, \sigma, \mu)$ are shown as bars.

$$\text{where } 1_p = \begin{cases} 1 & \text{if } p \text{ is true} \\ 0 & \text{otherwise} \end{cases}.$$

For $S_i(N, \sigma, \mu)$, the time at which the hole is opened $t_i^{(h)}(N, \sigma, \mu)$ was recorded. Using these values, we calculated the following functions:

- the average kinetic energy function after hole opening for simulations for which jamming occurred

$$E^{(1)}(N, \sigma, \mu)(t) = \frac{\sum_{i=1}^M E_i^{(1)}(N, \sigma, \mu)(t_i^{(h)}(N, \sigma, \mu) + t) \cdot \xi_i(N, \sigma, \mu)}{\sum_{i=1}^M \xi_i(N, \sigma, \mu)} \quad (7.8)$$

and the estimator of the standard deviation

$$E^{(1, stddev)}(N, \sigma, \mu)(t) = \sqrt{\frac{\sum_{i=1}^M (E^{(1)}(N, \sigma, \mu)(t) - E_i^{(1)}(N, \sigma, \mu)(t)) \cdot \xi_i(N, \sigma, \mu)}{(\sum_{i=1}^M \xi_i(N, \sigma, \mu) - 1) \sum_{i=1}^M \xi_i(N, \sigma, \mu)}} \quad (7.9)$$

- the average kinetic energy function of the grains above the hole, after hole opening for simulations for which jamming occurred

$$E^{(2)}(N, \sigma, \mu)(t) = \frac{\sum_{i=1}^M E_i^{(2)}(N, \sigma, \mu)(t_i^{(h)}(N, \sigma, \mu) + t) \cdot \xi_i(N, \sigma, \mu)}{\sum_{i=1}^M \xi_i(N, \sigma, \mu)} \quad (7.10)$$

and the estimator of the standard deviation

$$E^{(2, \text{stddev})}(N, \sigma, \mu)(t) = \sqrt{\frac{\sum_{i=1}^M (E^{(2)}(N, \sigma, \mu)(t) - E_i^{(2)}(N, \sigma, \mu)(t))^2 \xi_i(N, \sigma, \mu)}{(\sum_{i=1}^M \xi_i(N, \sigma, \mu) - 1) \sum_{i=1}^M \xi_i(N, \sigma, \mu)}}. \quad (7.11)$$

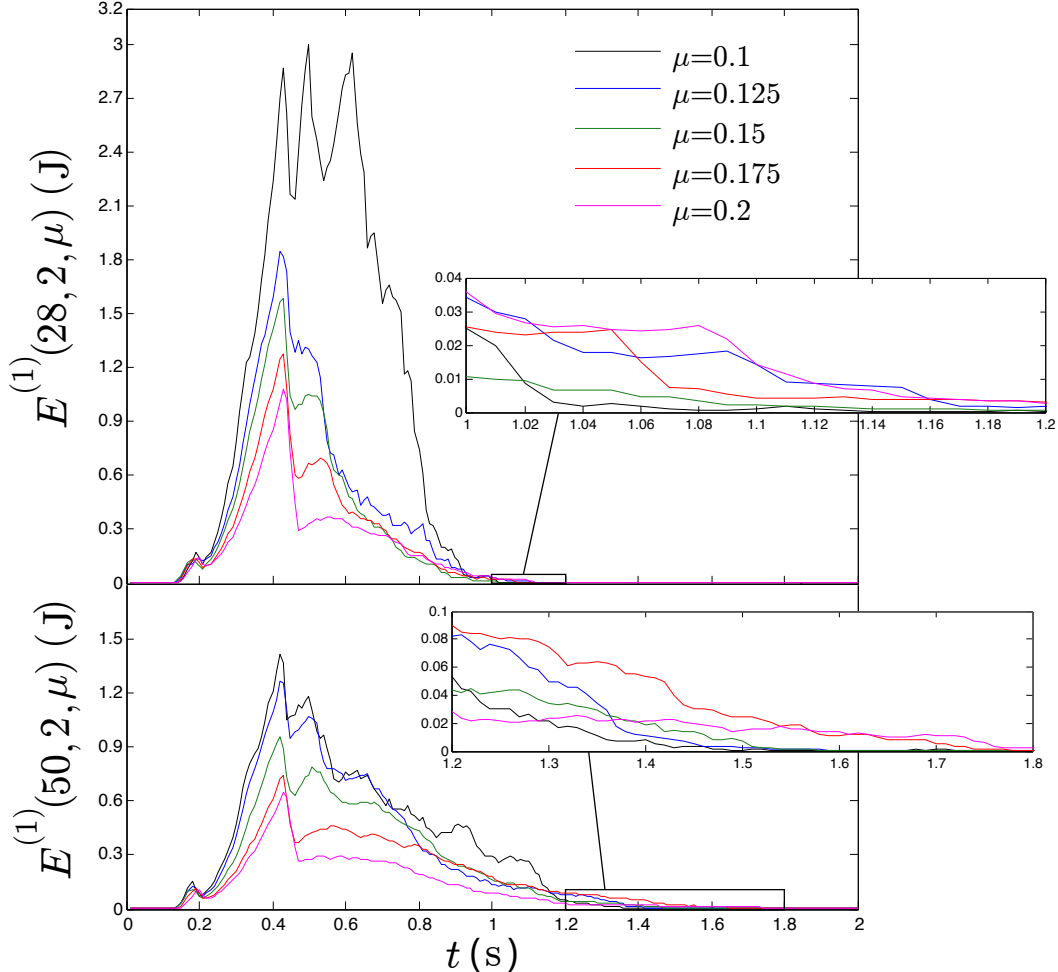


Figure 7.5: Average kinetic energy function $E^{(1)}(N, 2, \mu)(t)$ plotted against time, for $N = 28, 50$ and $\mu = 0.1, 0.125, 0.15, 0.175, 0.2$.

For $S_i(N, \sigma, \mu)$, the number of grains that flowed through the hole $\psi_i(N, \sigma, \mu)$ was calculated by

$$\psi_i(N, \sigma, \mu) = \sum_{j=1}^N \mathbf{1}_{x_{ij}(N, \sigma, \mu)_2(t_i^{(f)}) \leq H'(\sigma) - H(\sigma)}, \quad (7.12)$$

where $t_i^{(f)}$ is the time of the end of the simulation $S_i(N, \sigma, \mu)$.

This allowed to calculate the average number of grains $\psi(N, \sigma, \mu)$ that flowed through the hole for simulations for which jamming occurred and for a certain choice of parameters,

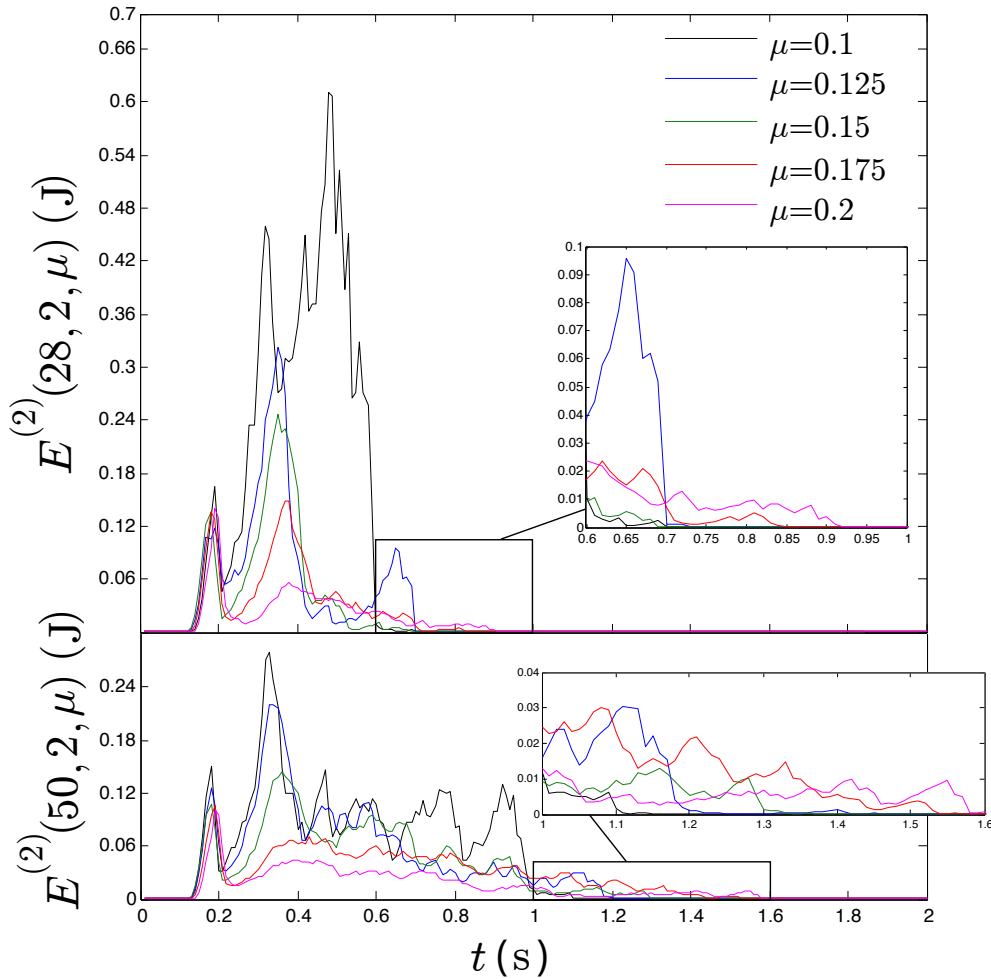


Figure 7.6: Average kinetic energy function $E^{(2)}(N, 2, \mu)(t)$ plotted against time, for $N = 28, 50$ and $\mu = 0.1, 0.125, 0.15, 0.175, 0.2$.

$$\psi(N, \sigma, \mu) = \frac{\sum_{i=1}^M \psi_i(N, \sigma, \mu) \xi_i(N, \sigma, \mu)}{\sum_{i=1}^M \xi_i(N, \sigma, \mu)}, \quad (7.13)$$

and the associated estimator of the standard deviation

$$\psi^{(stdddev)}(N, \sigma, \mu) = \sqrt{\frac{\sum_{i=1}^M (\psi(N, \sigma, \mu) - \psi_i(N, \sigma, \mu))^2 \xi_i(N, \sigma, \mu)}{(\sum_{i=1}^M \xi_i(N, \sigma, \mu) - 1) \sum_{i=1}^M \xi_i(N, \sigma, \mu)}}. \quad (7.14)$$

Figures 7.3 and 7.4 give $J_{DEM}(N, \sigma, \mu)$ for $\sigma = 2$ and for $\sigma = 3$ and for varying N and μ . In these figures, the bars give $J_{DEM}^{(stdddev)}(N, \sigma, \mu)$. According to these figures, the jamming probability is in good approximation a monotonic function of N and μ . Also, the jamming probability increases with increasing N and increasing μ . These results agree with intuition: one may conjecture that increasing N and increasing μ increases the jamming configurations and thus increase the jamming probability.

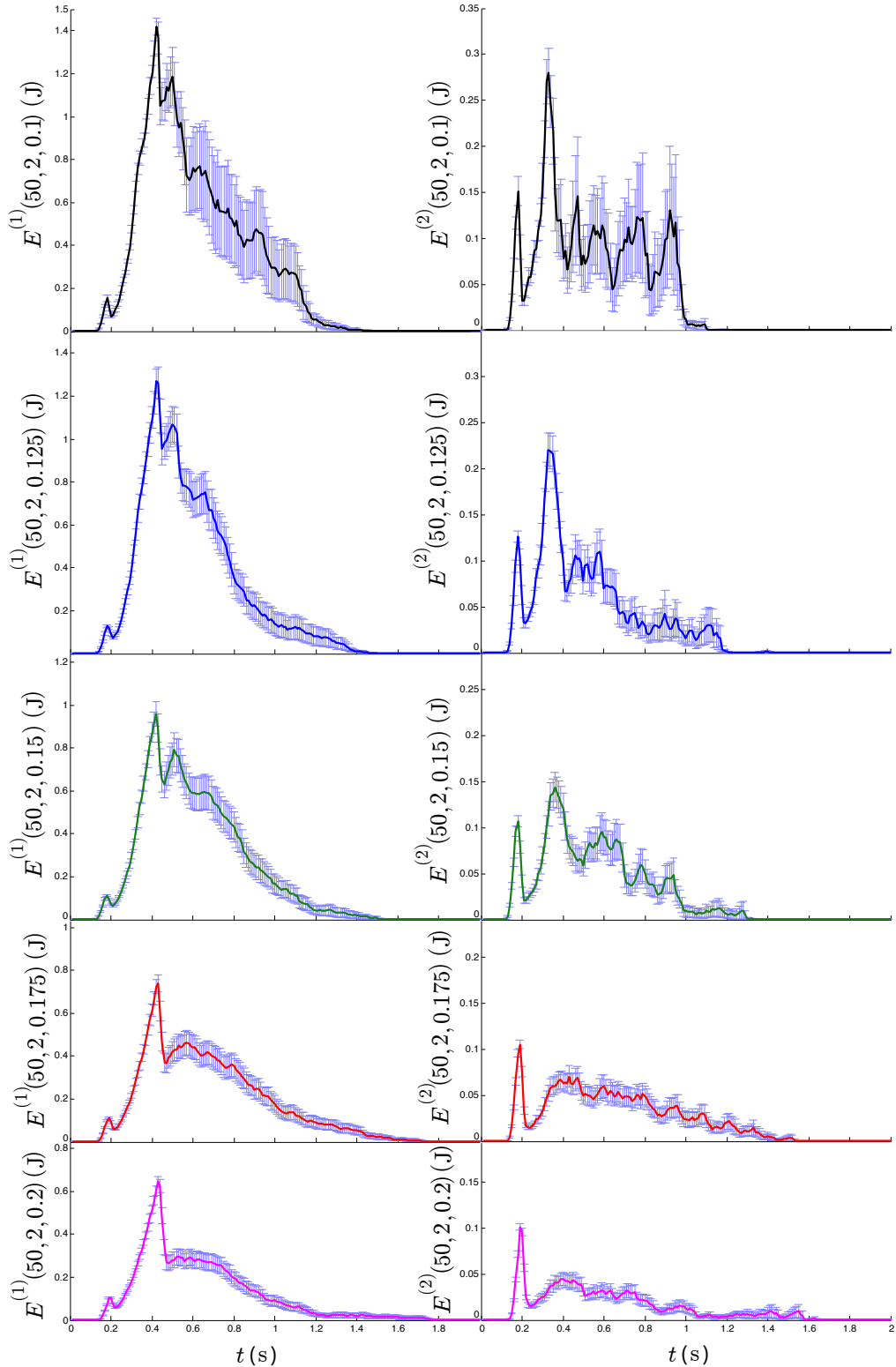


Figure 7.7: Average kinetic energy functions $E^{(1)}(50,2,\mu)(t)$ and $E^{(2)}(50,2,\mu)(t)$ plotted against time, for $\mu = 0.1, 0.125, 0.15, 0.175, 0.2$. Estimators of standard deviations $E^{(1, stddev)}(50,2,\mu)(t)$ and $E^{(2, stddev)}(50,2,\mu)(t)$ are shown as bars.

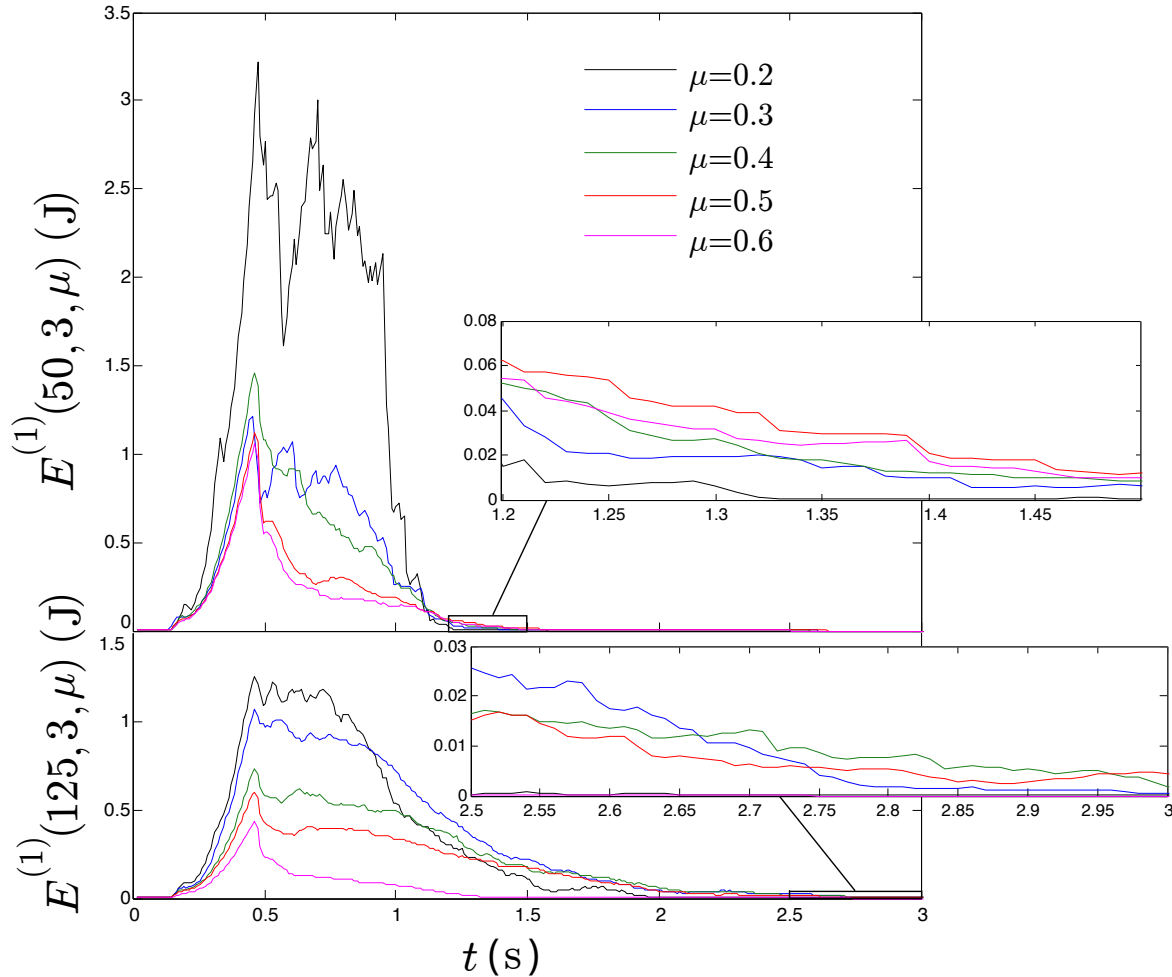


Figure 7.8: Average kinetic energy function $E^{(1)}(N,3,\mu)(t)$ plotted against time, for $N = 50, 125$ and $\mu = 0.2, 0.3, 0.4, 0.5, 0.6$.

Figures 7.5 and 7.6 show $E^{(1)}(N,2,\mu)(t)$ and $E^{(2)}(N,2,\mu)(t)$ for $N = 28, 50$ and $\mu = 0.1, 0.125, 0.15, 0.175, 0.2$. To give an idea on the precision of these results, figure 7.7 shows the same graphs as in figures 7.5 and 7.6 for $N = 50$ with $E^{(1, stddev)}(N, \sigma, \mu)$ and $E^{(2, stddev)}(N, \sigma, \mu)$ shown as bars. Figures 7.8 and 7.9 show $E^{(1)}(N,3,\mu)(t)$ and $E^{(2)}(N,3,\mu)(t)$ for $N = 50, 125$ and $\mu = 0.2, 0.3, 0.4, 0.5, 0.6$. In all figures showing $E^{(1)}$ and $E^{(2)}$ and in the associated insets, we observe that the energies are decreasing functions of μ up to a certain time and thereupon become increasing functions of μ . The reversal of tendency is quite clear in the insets except for $E^{(2)}$ in figure 7.9. The explanation for the first tendency is that in average the number of grains that flow through the hole is a decreasing function of μ (see Fig. 7.11). We don't yet have an explanation for the reversal of tendency. A measure of the average time before jamming is the time at which energy functions $E^{(1)}$ or $E^{(2)}$ stay below a given threshold. A consequence of the observed reversal of tendency is that depending on which threshold is chosen the average time before jamming can be found to be an increasing or decreasing function of μ .

Figures 7.6 and 7.9 show that $E^{(2)}(N, \sigma, \mu)$ has two distinct bumps. We conjecture that the first bump corresponds to a reaction of the medium to the hole opening and the second to the flow phase. This is not yet well understood and requires more study.

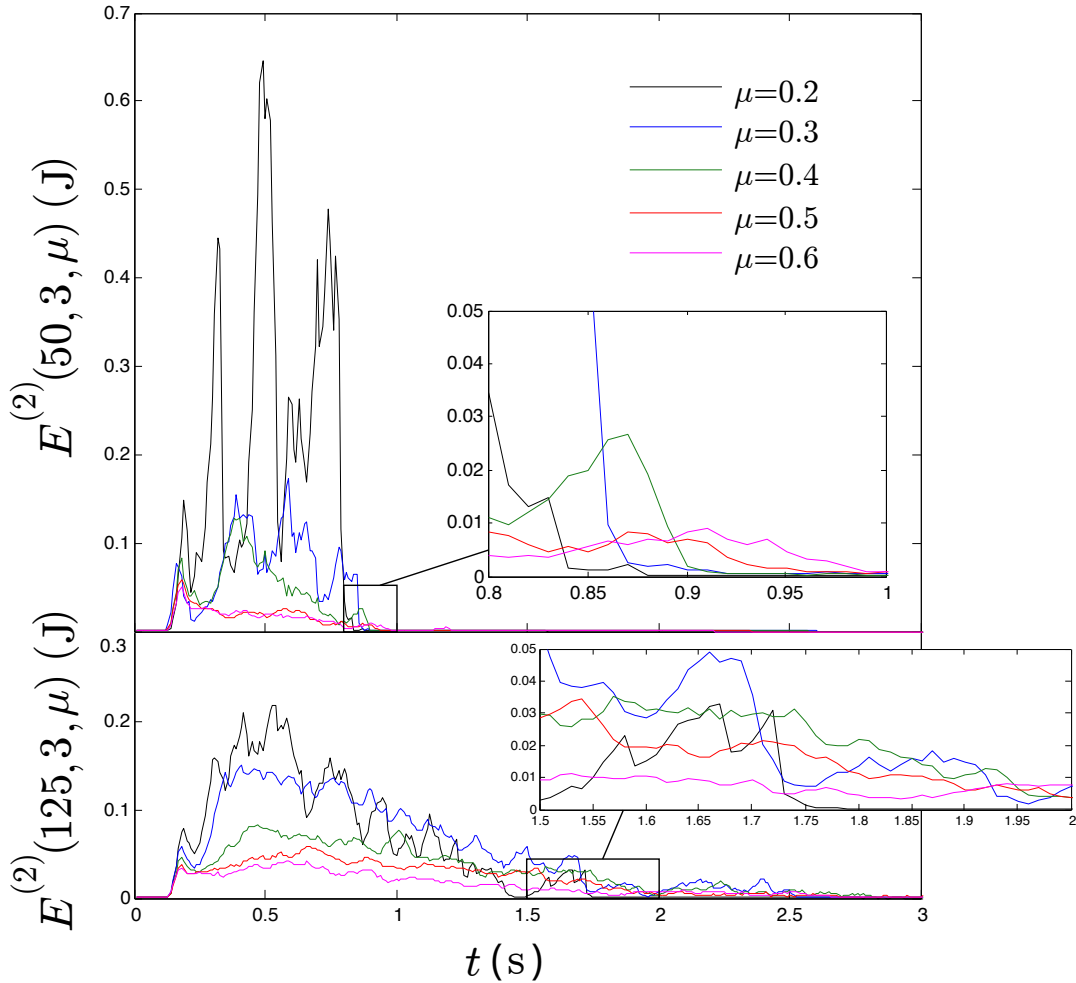


Figure 7.9: Average kinetic energy function $E^{(2)}(N, 3, \mu)(t)$ plotted against time, for $N = 50, 125$ and $\mu = 0.2, 0.3, 0.4, 0.5, 0.6$.

Figure 7.10 shows $E^{(2)}(N, 2, \mu)(t)$ for $\mu = 0.15, 0.2$ and different values of N , and $E^{(2)}(N, 3, \mu)(t)$ for $\mu = 0.4, 0.6$ and different values of N . In this figure, we notice that $E^{(2)}$ is an increasing function of N . This is in agreement with intuition since the flow of grains when jamming occurs is larger when N is higher (see Fig. 7.11). Thus, it seems plausible that when jamming occurs the grains reach higher velocities and higher kinetic energies when N is higher.

Figure 7.11 shows $\psi(N, \sigma, \mu)$ as a function of N for $\sigma = 2$ and $\mu = 0.1, 0.125, 0.15, 0.175, 0.2$, and $\sigma = 3$ and $\mu = 0.2, 0.3, 0.4, 0.5, 0.6$. In this figure, one may observe that ψ is in good approximation an increasing linear function of N , and a decreasing function of μ . This shows that the flow when jamming occurs increases with increasing N and decreasing μ .

We confirm in this section the result that several authors have already described [Brown, 1961; To et al., 2001; Zuriguel et al., 2003] that the jamming probability increases as the ratio $\frac{\sigma}{d}$ between hopper opening and grain diameter decreases.

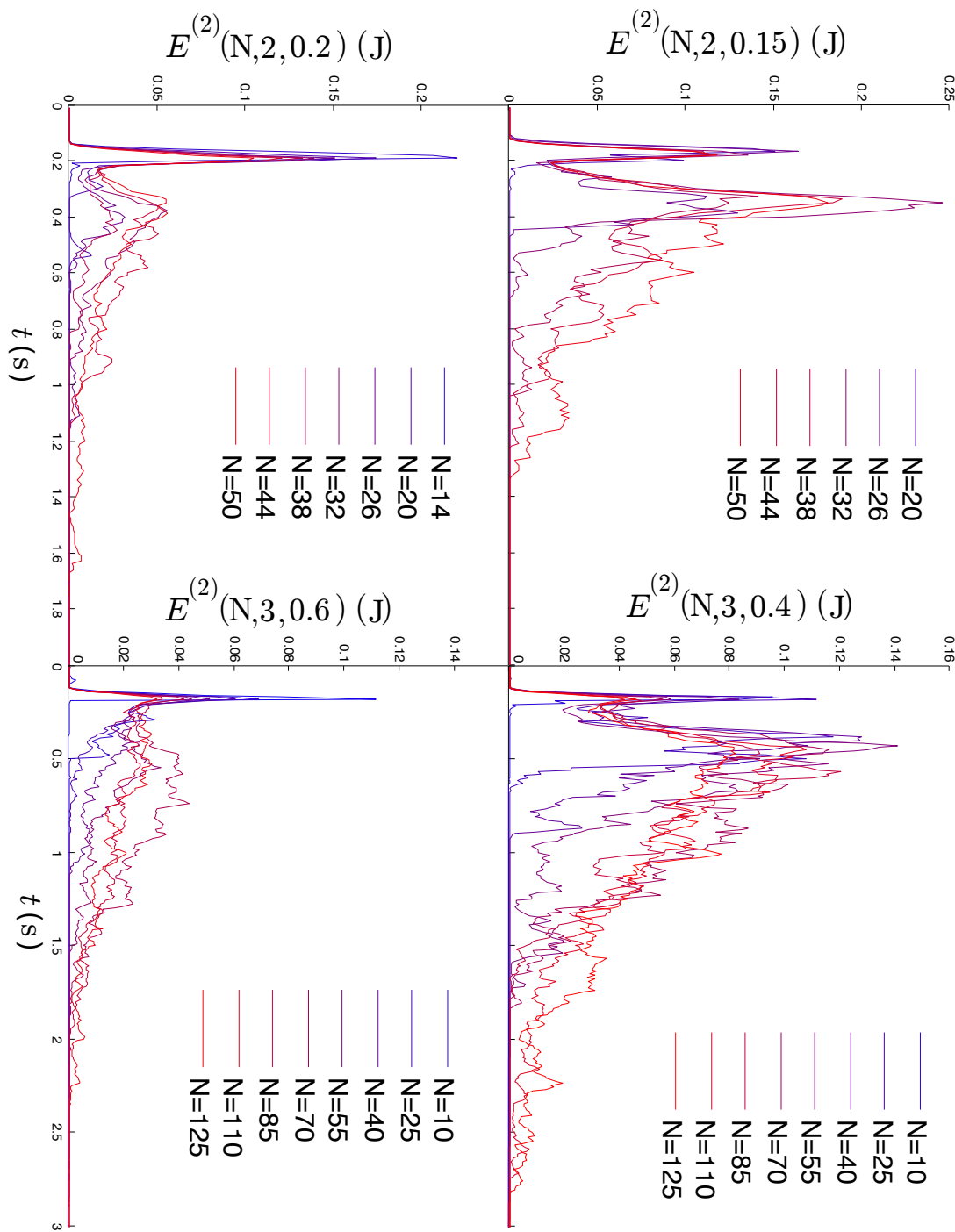


Figure 7.10: Average kinetic energy function $E^{(2)}(N, 2, \mu)(t)$ plotted against time, for $\mu = 0.15, 0.2$ and different values of N , as well as average kinetic energy function $E^{(2)}(N, 3, \mu)(t)$ plotted against time, for $\mu = 0.4, 0.6$ and different values of N .

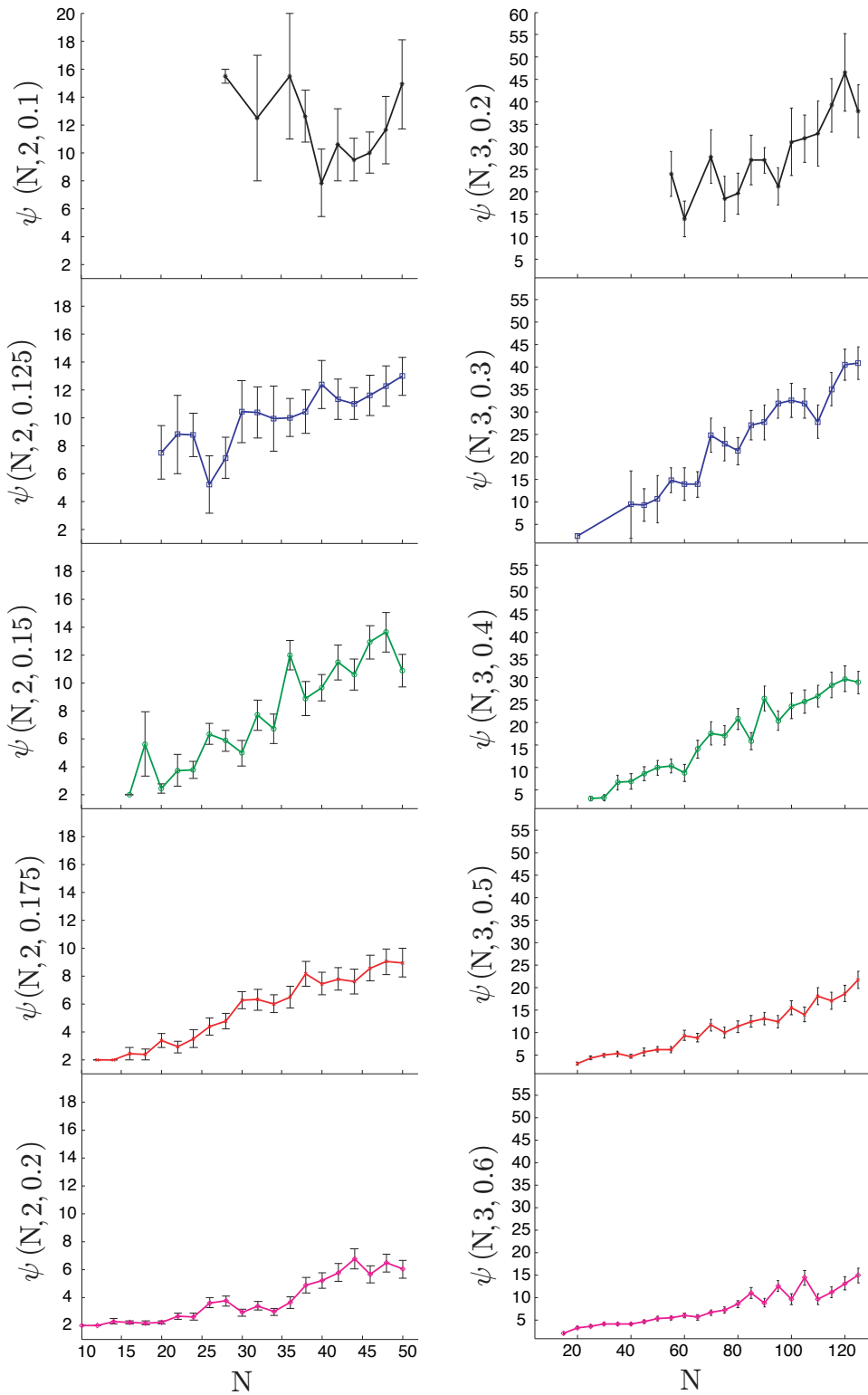


Figure 7.11: Average number, $\psi(N, \sigma, \mu)$, of grains that fall through the hole as a function of N for $\sigma = 2$ and $\mu = 0.1, 0.125, 0.15, 0.175, 0.2$, and $\sigma = 3$ and $\mu = 0.2, 0.3, 0.4, 0.5, 0.6$. Estimators of the standard deviations $\psi^{(stddev)}(N, \sigma, \mu)$ are shown as bars.

7.3 Influence of grain length

7.3.1 Setup

The setup for the simulations to study the influence of grain length was as follows.

The hopper was as in figure 7.1 with $\sigma = 2$, $\phi = \pi/3$, $L = 0.810022m$ and $H = 0.632218m$. In each simulation, 50 identical 2D spherocylinders of radius r , length l and area $A = 0.00125664 m^2$ were inserted. The grain friction coefficient was $\mu = 0.1$. Grain length, l was varied from $0.0 m$ to $0.1 m$ by steps of $0.01 m$. The different types of grains are represented in Fig. 7.12. For each length about 800 simulations were carried out.

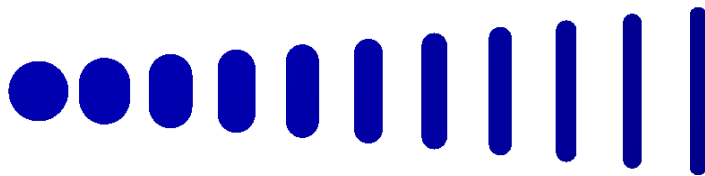


Figure 7.12: Different types of grains to study the influence of grain length on jamming.

Insertion of grains, initial settlement of grains with hole closed and simulation after hole is opened was the same as in section 7.2.

7.3.2 Results and discussion

Fig. 7.13 shows snapshots of a simulation with grains of length 0.1 for which jamming has occurred.

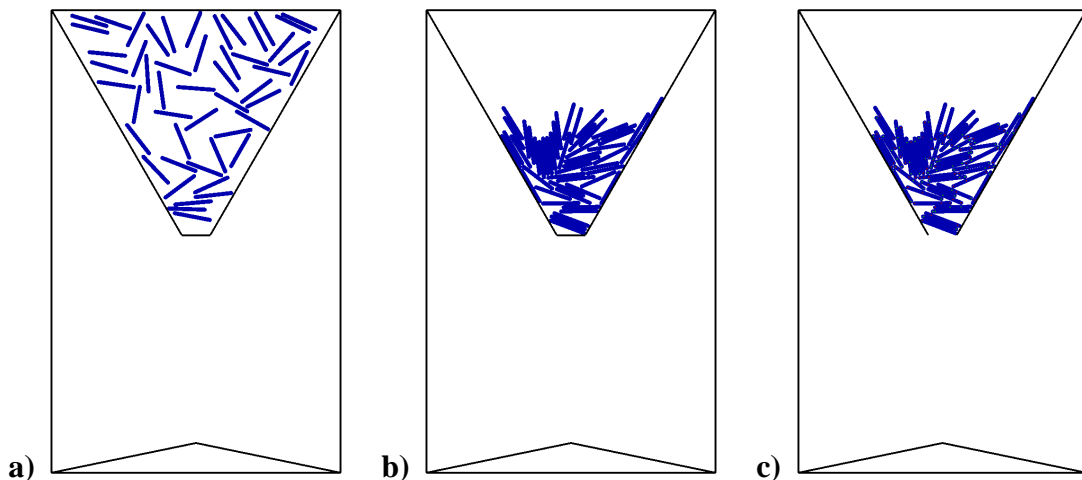


Figure 7.13: Snapshots of a simulation for which jamming has occurred: a) Initial insertion of grains b) Settled configuration before hole opening c) Jammed configuration.

Similarly as in section 7.2, for the i^{th} simulation \bar{S}_i in which grains have length l , we calculated different quantities that characterize the jamming behavior: the jamming probability $\bar{J}_{DEM}(l)$ and associated standard deviation $\bar{J}_{DEM}^{(stddev)}(l)$, energy functions $\bar{E}^{(1)}(l)$ and $\bar{E}^{(2)}(l)$ and associated standard deviations $\bar{E}^{(1,stddev)}(l)$ and $\bar{E}^{(2,stddev)}(l)$, and average grains that fall through the hole $\bar{\Psi}(l)$. For definitions of these replace M by \bar{M} , S by \bar{S} , (N, σ, μ) by (l) , ξ by $\bar{\xi}$, x by \bar{x} , v by \bar{v} , J by \bar{J} , E by \bar{E} and ψ by $\bar{\Psi}$ in the definitions of section 7.2.2.

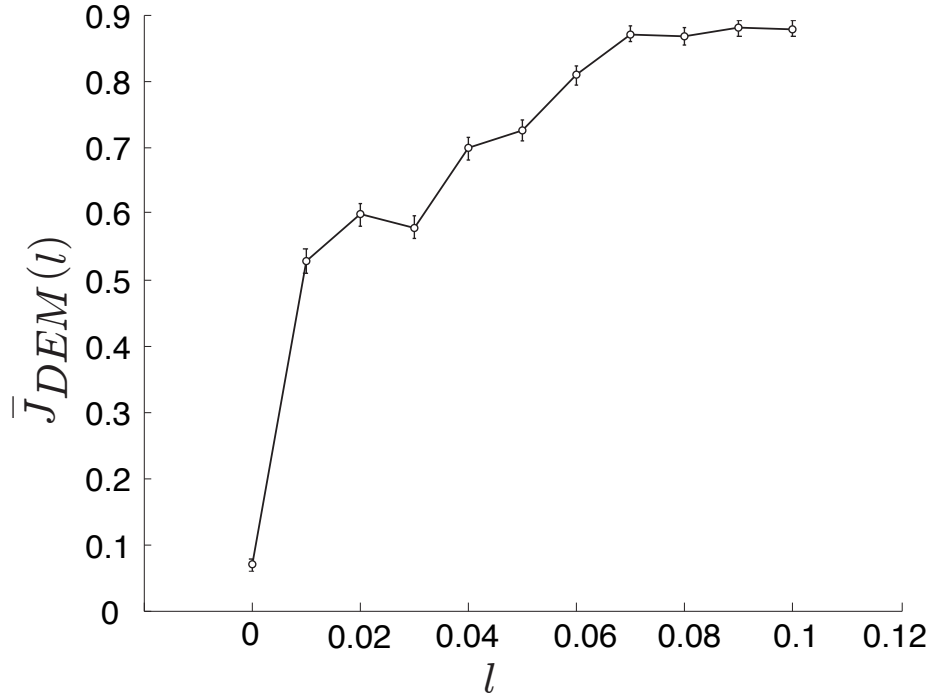


Figure 7.14: Jamming probability $\bar{J}_{DEM}(l)$ for varying grain length l . Estimators of the standard deviations $\bar{J}_{DEM}^{(stddev)}(l)$ are shown as bars.

Figure 7.14 shows that jamming probability is a roughly increasing function of the grain length. We conjecture that this is because for increasing grain length the number of jamming configurations increase. An explanation for this might be that even if the grain area is kept constant the grain perimeter increases with grain length. Figures 7.15 and show that both $\bar{E}^{(2)}$ and $\bar{\Psi}$ are non-monotonic functions of l . An explanation for the abrupt decrease of $\bar{\Psi}$ between $l = 0.06\text{ m}$ and $l = 0.07\text{ m}$ is that for $l = 0.06\text{ m}$ the grains can pass horizontally through the hole while for $l = 0.07\text{ m}$ they can not. An explanation for the increase of $\bar{\Psi}$ between $l = 0.07\text{ m}$ and $l = 0.1\text{ m}$ is that the closer the grain length is to the hole size the more there is a tendency for the grains near the hole to be placed in the settled configuration in a horizontal configuration blocking the hole (see Fig. 7.17).

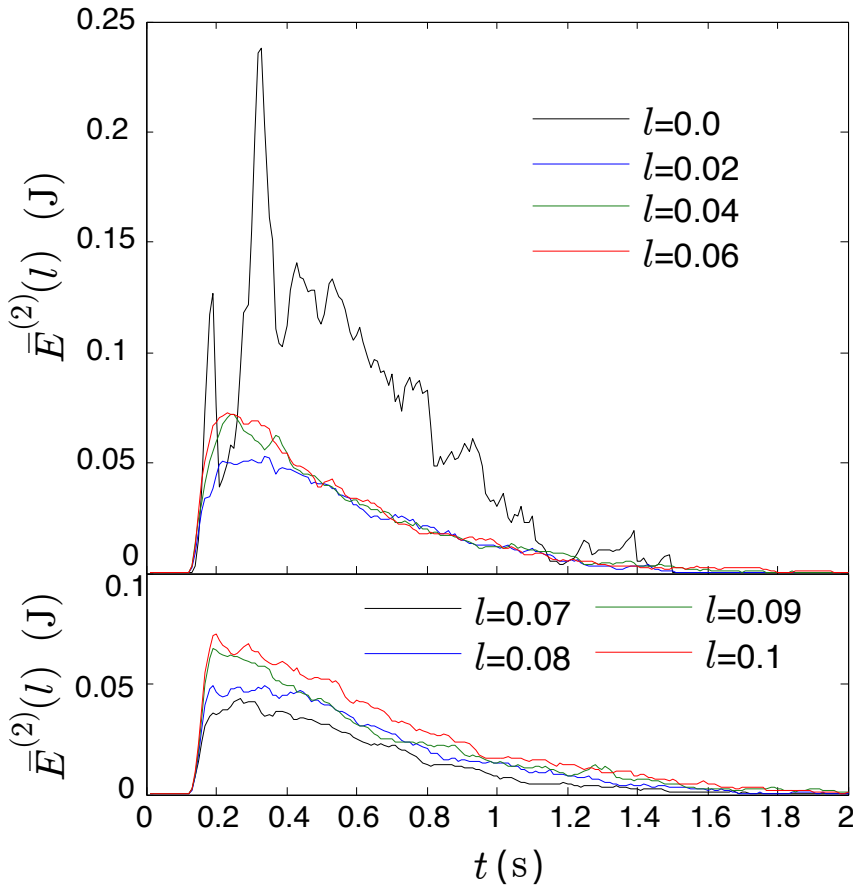


Figure 7.15: Average kinetic energy function $\bar{E}^{(2)}(l)$ plotted against time, for varying grain length l . Note the differing behavior of the upper and lower curves for increasing grain length.

7.4 Influence of hopper angle

7.4.1 Setup

The setup for the simulations to study the influence of hopper angle was as follows.

The hopper was as in figure 7.1 with $\sigma = 2$, $L = 0.810022m$ and $H = 0.632218m$. Hopper angle was varied between $\phi = 30^\circ$ and $\phi = 75^\circ$ by steps of 5° . The grains were identical discs of radius $r = 0.02m$. The grain friction coefficient was $\mu = 0.15$. For each hopper angle about $\hat{M} = 800$ simulations were carried out.

Insertion of grains, initial settlement of grains with hole closed and simulation after hole is opened was the same as in section 7.2.

7.4.2 Results and discussion

Fig. 7.18 shows final snapshots of simulations for $\phi = 30^\circ$ and $\phi = 75^\circ$ and for which jamming has occurred.

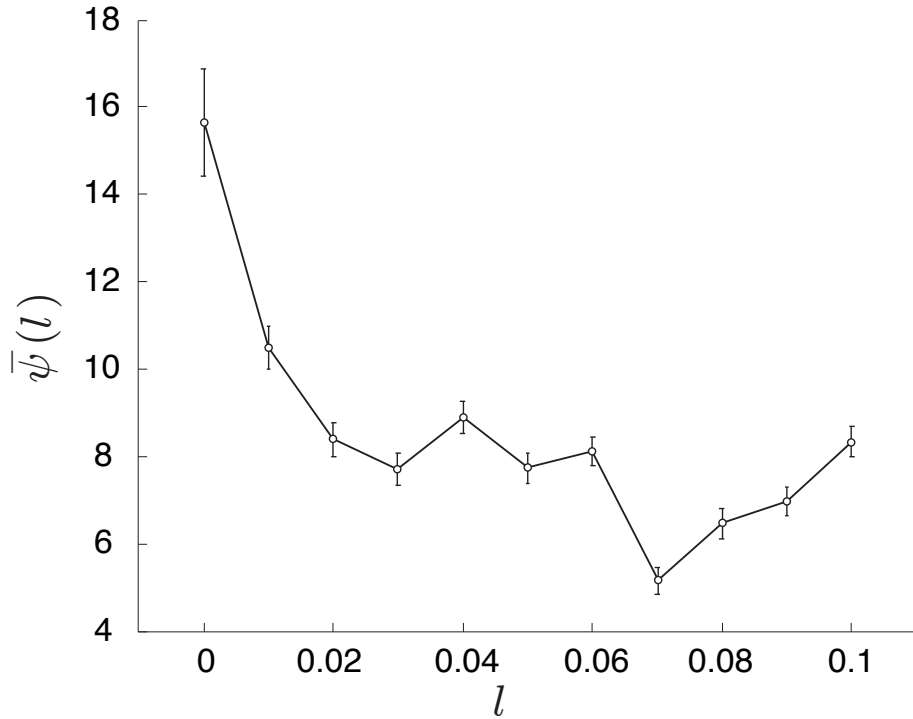


Figure 7.16: Average number, $\bar{\psi}(l)$, of grains that fall through the hole for varying grain length l . Estimators of the standard deviations $\bar{\psi}^{(stddev)}(l)$ are shown as bars.

Similarly as in section 7.2, for the i^{th} simulation \hat{S}_i in which hopper angle is ϕ , we calculated different quantities that characterize the jamming behavior: the jamming probability $\hat{J}_{DEM}(\phi)$ and associated standard deviation $\hat{J}_{DEM}^{(stddev)}(\phi)$, energy functions $\hat{E}^{(1)}(\phi)$ and $\hat{E}^{(2)}(\phi)$ and associated standard deviations $\hat{E}^{(1,stddev)}(\phi)$ and $\hat{E}^{(2,stddev)}(\phi)$, and average grains that fall through the hole $\hat{\psi}(\phi)$. For definitions of these replace M by \hat{M} , S by \hat{S} , (N, σ, μ) by (ϕ) , ξ by $\hat{\xi}$, x by \hat{x} , v by \hat{v} , J by \hat{J} , E by \hat{E} and ψ by $\hat{\psi}$ in the definitions of section 7.2.2.

Figure 7.19 shows the results in agreement with intuition that the jamming probability \hat{J}_{DEM} is a roughly decreasing function ϕ . This confirms results found by To [To, 2002]. However, figures 7.20 and 7.21 show a surprising result in that the flow of grains which increases up to $\phi = 65^\circ$, suddenly decreases between $\phi = 65^\circ$ and $\phi = 70^\circ$ and increases again between $\phi = 70^\circ$ and $\phi = 75^\circ$. We do not yet have an explanation for this.

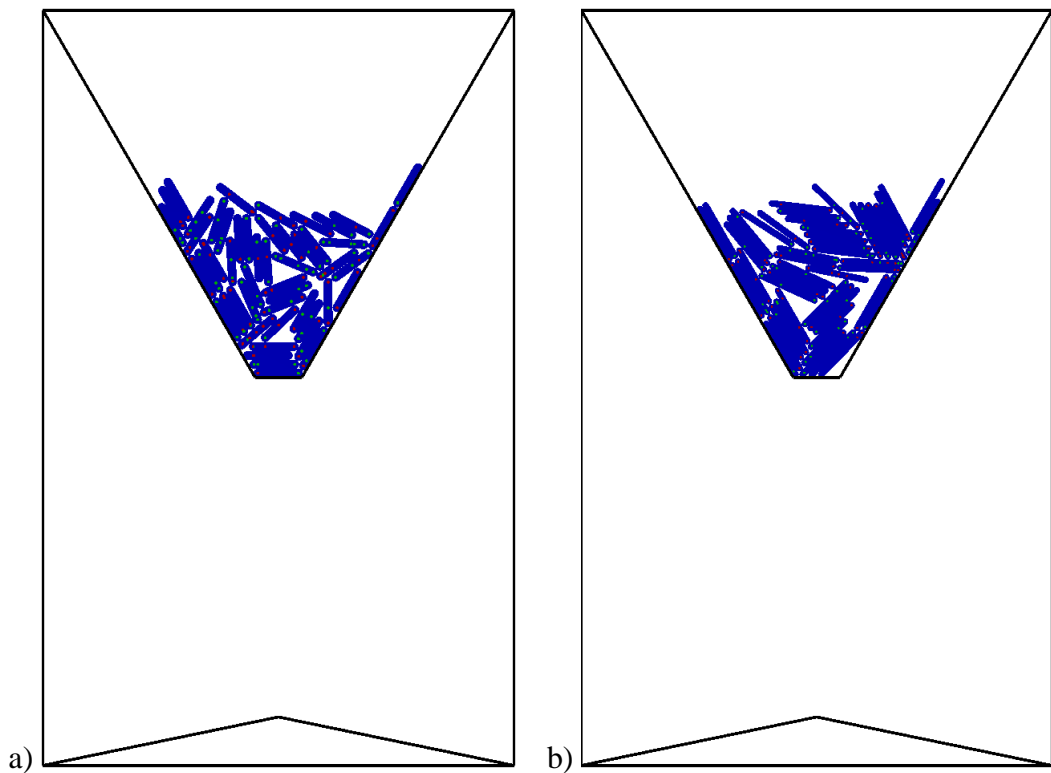


Figure 7.17: Snapshots of settled configuration for two simulations used to study the influence of length on jamming: a) $l = 0.07 \text{ m}$ b) $l = 0.1 \text{ m}$. Notice that for $l = 0.07 \text{ m}$ the grains near the hole are in horizontal position while for $l = 0.1 \text{ m}$ they are not.

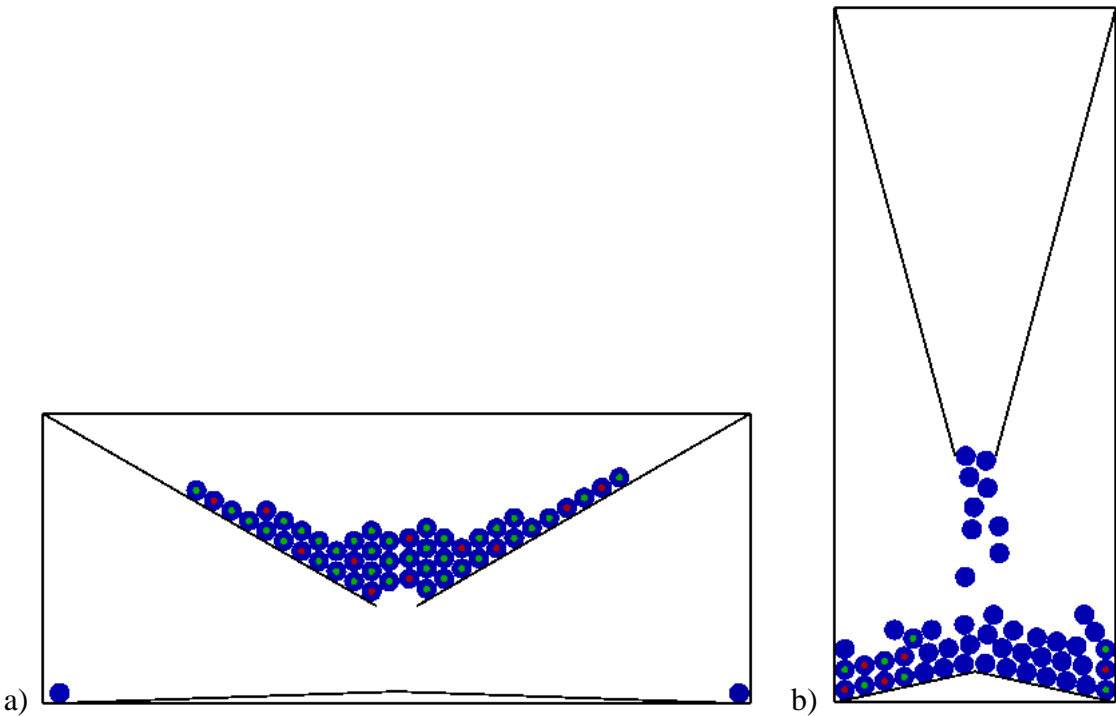


Figure 7.18: Final snapshots of two simulations used to study the influence of hopper angle on jamming: a) $\phi = 30^\circ$ b) $\phi = 75^\circ$.

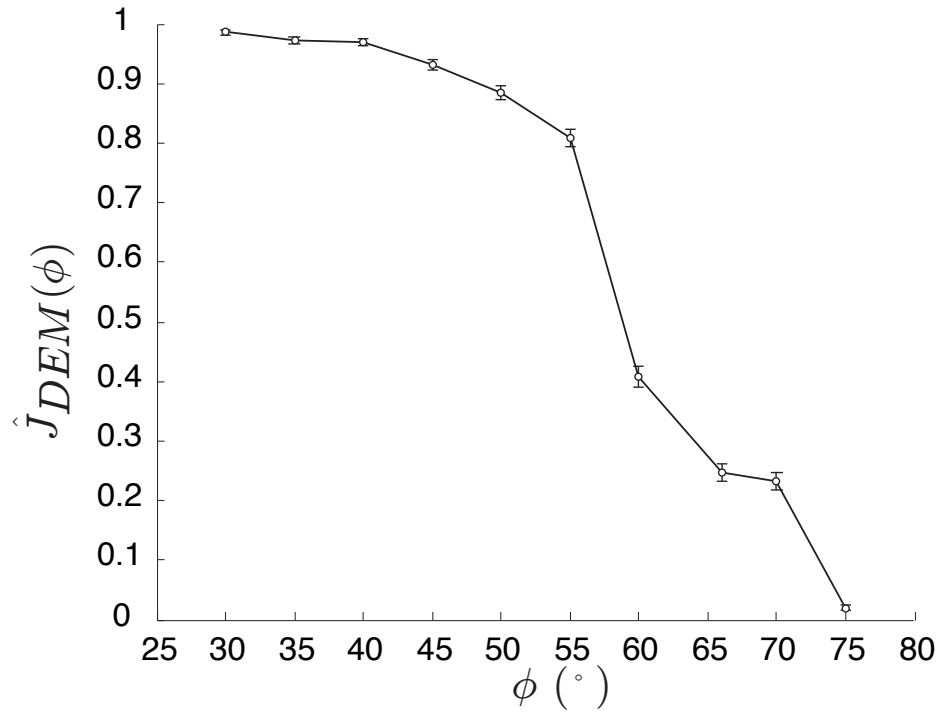


Figure 7.19: Jamming probability $\hat{J}_{DEM}(\phi)$ for varying hopper angle ϕ . Estimators of the standard deviations $\hat{J}_{DEM}^{(stddev)}(\phi)$ are shown as bars.

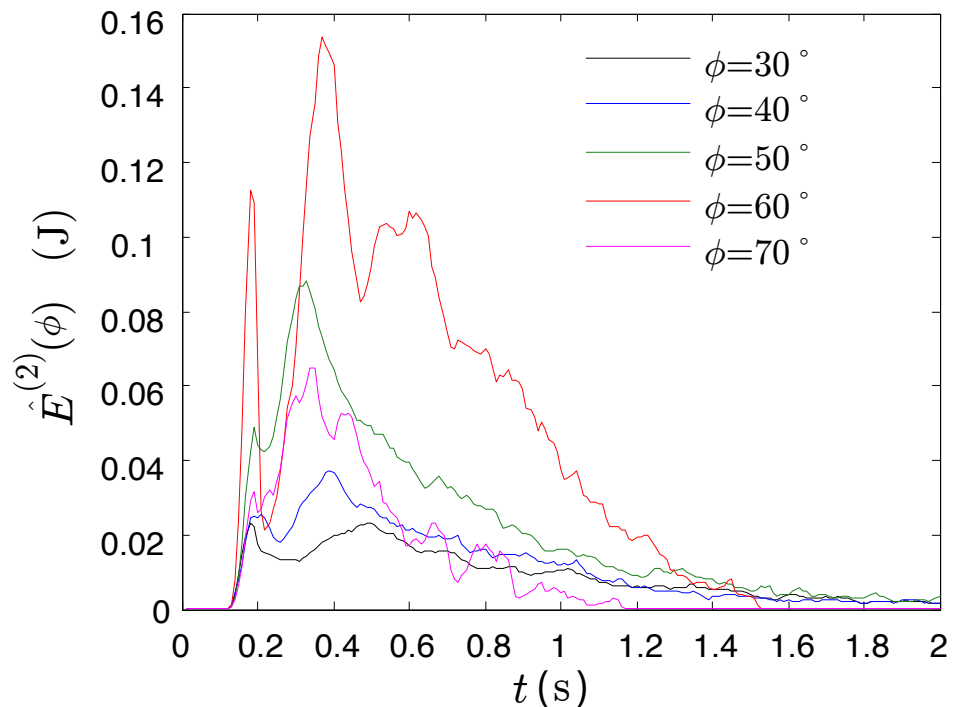


Figure 7.20: Average kinetic energy function $\hat{E}^{(2)}(\phi)$ plotted against time, for varying hopper angle ϕ .

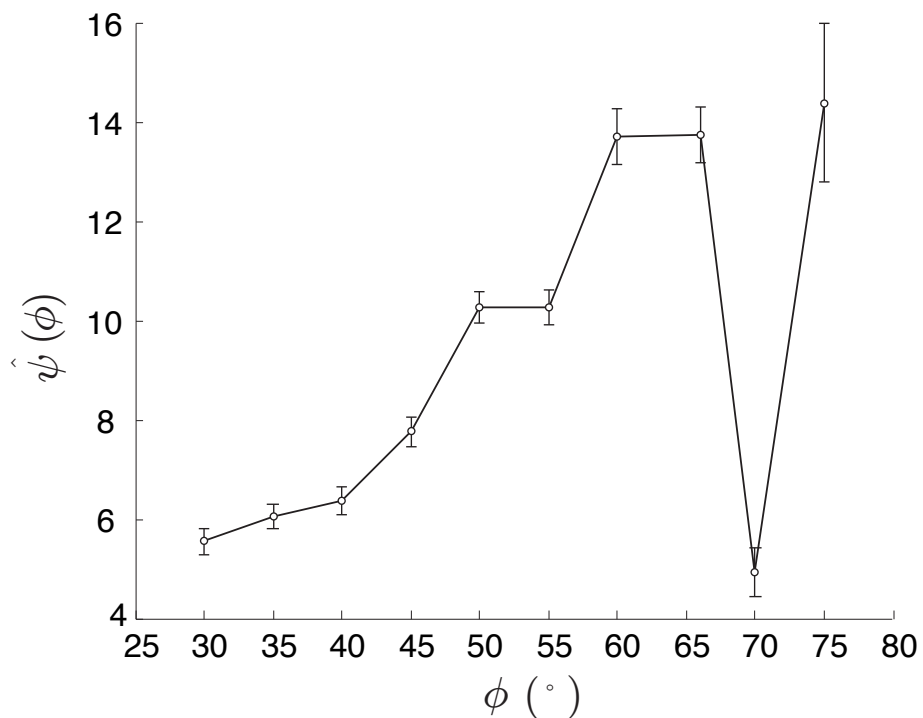


Figure 7.21: Average number, $\hat{\psi}(\phi)$, of grains that fall through the hole for varying hopper angle ϕ . Estimators of the standard deviations $\hat{\psi}^{(stddev)}(\phi)$ are shown as bars.

Physicists define stress as force per unit area. The rest of humanity defines stress as physics.
– Author unknown

Chapter 8

Fitting SPM and DEM

8.1 How to find a relationship between SPM and DEM

We call the jamming probabilities for SPM with the first version of the insertion of grains, and DEM, $J_{SPM}(n, \tau, \varepsilon)$ and $J_{DEM}(N, \sigma, \mu)$. The objective is to use SPM to capture J_{DEM} . More precisely, we look for a dictionary, i.e. functions $f_1(N, \sigma, \mu)$, $f_2(N, \sigma, \mu)$ and $f_3(N, \sigma, \mu)$ such that

$$J_{DEM}(N, \sigma, \mu) = J_{SPM}((f_1, f_2, f_3)(N, \sigma, \mu)). \quad (8.1)$$

As a first step, we supposed that $f_1(N, \sigma, \mu) = N$ and $f_2(N, \sigma, \mu) = \sigma$. We then searched for $\varepsilon = f_3(N, \sigma, \mu)$ which satisfied

$$J_{DEM}(N, \sigma, \mu) = J_{SPM}(N, \sigma, f_3(N, \sigma, \mu)). \quad (8.2)$$

It can be shown that J_{SPM} is a monotonous function of its variables. Hence, if $g_{n, \tau}(\varepsilon) = J_{SPM}(n, \tau, \varepsilon)$, $g_{n, \tau}$ is a monotonous function whose inverse $g_{n, \tau}^{-1}$ exists. Thus, according to equation (8.2)

$$f_3(N, \sigma, \mu) = g_{N, \sigma}^{-1} \circ J_{DEM}(N, \sigma, \mu). \quad (8.3)$$

To study f_3 , for each N and σ as given in TABLE 7.2, we found $g_{n, \tau}^A$, a linear least squares approximation of $g_{n, \tau}$, and J_{DEM}^A a linear or cubic least squares approximation of J_{DEM} , thus yielding approximation of f_3

$$f_3^A(N, \sigma, \mu) = g_{N, \sigma}^{A-1} \circ J_{DEM}^A(N, \sigma, \mu). \quad (8.4)$$

f_3^A is either a linear or cubic function.

8.2 Results and discussion

The procedure described in the last section was carried out using all the DEM data except the simulations with 80 grains and $\sigma = 2$ and with 250 grains and $\sigma = 3$.

When J_{DEM}^A was approximated by a cubic function, the variation of f_3^A did not show any simple tendency. The reason for this is not clear. However, we suppose that the residual random fluctuation of the DEM jamming probability estimates was the cause for this. Future work should include testing this explanation. On the other hand when J_{DEM}^A was approximated by a linear function, the variation of f_3^A did take a simple form, as described below, allowing its extrapolation to other values of N . Note that since only 2 values of σ were used, it was impossible to extrapolate to other values of σ . In this case, $\mu \mapsto f_3^A(N, \sigma, \mu)$ was a linear function:

$$a(N, \sigma)\mu + b(N, \sigma). \quad (8.5)$$

$a(N, \sigma)$ and $b(N, \sigma)$ are plotted in FIG. 8.1 and in FIG. 8.2 where a scaling parameter $\gamma(\sigma)$ has been used to ease their representation.

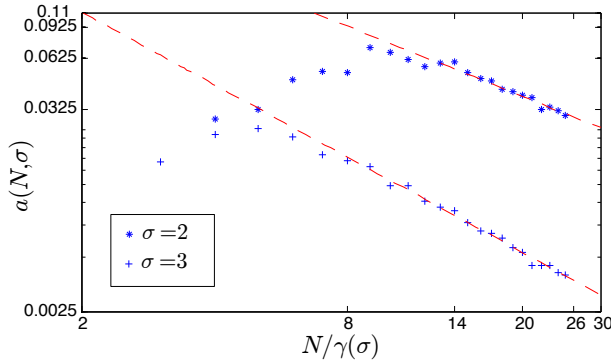


Figure 8.1: Values of coefficient a , the first derivative of linear function $\mu \mapsto f_3^A(N, \sigma, \mu)$: scaling parameter; $\gamma(2) = 2$, $\gamma(3) = 5$

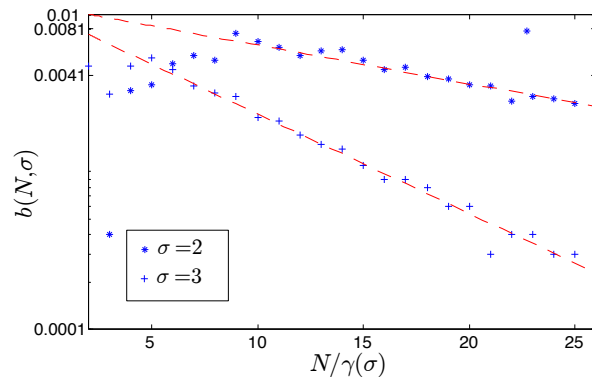


Figure 8.2: Values of coefficient b , the constant coefficient of linear function $\mu \mapsto f_3^A(N, \sigma, \mu)$: scaling parameter; $\gamma(2) = 2$, $\gamma(3) = 5$

	$\sigma = 2$	$\sigma = 3$
$a(N, \sigma)$	$1.3981N^{-0.9753}$	$2.3272N^{-1.322}$
$b(N, \sigma)$	$-0.0113 \cdot 0.9721^N$	$-0.01 \cdot 0.9713^N$

Table 8.1: Least squares approximations of $a(N, \sigma)$ and $b(N, \sigma)$, the coefficients of $\mu \mapsto f_3^A(N, \sigma, \mu)$, for $\sigma = 2, 3$

FIG. 8.1 shows that when N is larger than a threshold value, the plot of $a(N, \sigma)$ is approximately linear in a log-log representation. This implies that in good approximation $a(N, \sigma)$ for N large has the form

$$a(N, \sigma) = A(\sigma)N^{B(\sigma)}. \quad (8.6)$$

Similarly, when N is larger than a threshold value, the plot of $b(N, \sigma)$ is approximately linear in a semi-logarithmic (in the ordinate) representation. This implies that in good approximation $b(N, \sigma)$ for N large has the form

$$b(N, \sigma) = C(\sigma)D(\sigma)^N. \quad (8.7)$$

Coefficients $A(\sigma)$, $B(\sigma)$, $C(\sigma)$ and $D(\sigma)$ were found by the least squares method. $a(N, \sigma)$ and $b(N, \sigma)$ are recapitulated in TABLE 8.1.

Using the dictionary found between SPM and DEM it was possible to predict the DEM jamming probability. FIG. 8.3 and FIG. 8.4 shows the DEM simulation results and predictions using SPM. These figures show that the predictions using SPM fit the available DEM data quite well for n large enough.

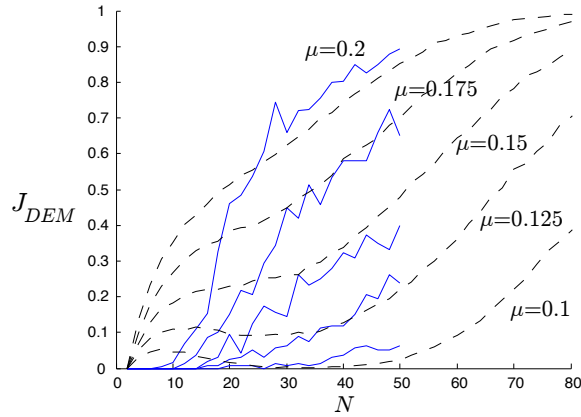


Figure 8.3: DEM jamming probability, J_{DEM} , as a function of N for $\sigma = 2$ and various values of μ : continuous line, simulation results; dashed line, predictions using SPM

The absolute difference between predictions and simulation results, for $\sigma = 2$ and $N = 80$, and for $\sigma = 3$ and $N = 250$, are plotted in FIG. 8.5 and FIG. 8.6. These figures show that the long

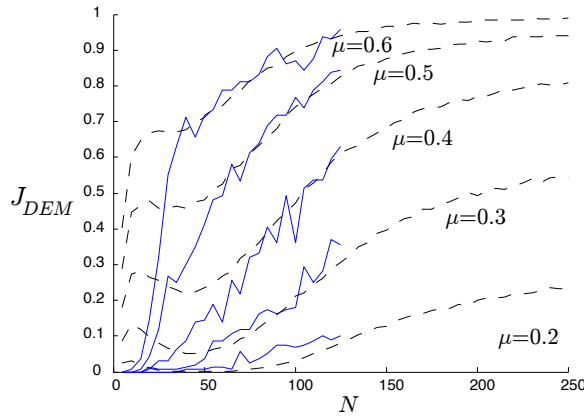


Figure 8.4: DEM jamming probability, J_{DEM} , as a function of N for $\sigma = 3$ and various values of μ : continuous line, simulation results; dashed line, predictions using SPM

range predictive power is limited. This is most probably due to the hypotheses made on the dictionary (recall that $\mu \mapsto f_3(N, \sigma, \mu)$ was assumed linear). In future work, different simple models should be tried out to see if realistic hypotheses are easier to make.

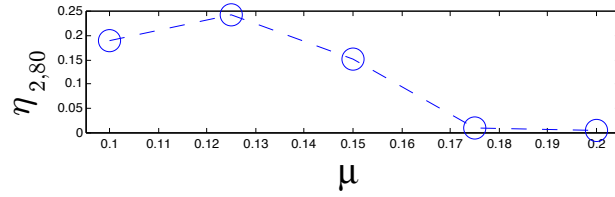


Figure 8.5: Error in predicting J_{DEM} , $\eta_{2,80} = |J_{DEM}^{SPM} - J_{DEM}|$, for $N = 80$ and $\sigma = 2$ (J_{DEM}^{SPM} , prediction using SPM)

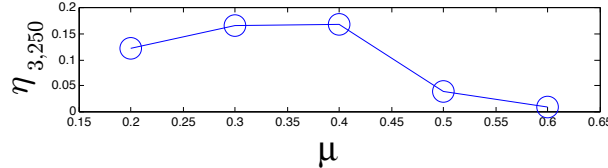


Figure 8.6: Error in predicting J_{DEM} , $\eta_{3,250} = |J_{DEM}^{SPM} - J_{DEM}|$ for $N = 250$ and $\sigma = 3$

8.3 Conclusion

We have proposed a simple probabilistic model (SPM) of granular flows in bi-dimensional hoppers. We have found that when the number of grains is large enough, the jamming probabilities for SPM and for DEM simulations are related, allowing us to extrapolate the jamming probability for DEM. Due to limited computer power our study was restrained to 2 small sizes of the hopper hole. This was not enough to analyze the behavior of the DEM jamming probability as a

function of the hole size. However, although the long range predictive power of the approach is limited, we demonstrated that SPM can capture well the DEM jamming probability in the range of the available DEM data. Future work should include generalizing the approach to cases when the input data is of higher precision. Furthermore, SPM may be replaced by other models in a search for the most adequate model for predicting the DEM jamming probability.

*Write bad things that are done to you in sand, but write the good things that happen to you on
a piece of marble*
–Arab proverb

Conclusion

In one main part of this thesis we present an experimental validation of DEM. Nine real experiments of jamming in a hopper were carried out. In each, a cylindrical container with a closed bottom aperture was filled with glass beads. A initial 3D X-ray synchrotron digital tomograph of the medium was taken. Then the aperture was opened. After settlement of the medium a final tomograph was taken. In order to find sphere-fittings of the beads, the tomographs were computer processed and analyzed. For this, a multi-resolution computer program was developed. The main steps in this program were pre-processing of the raw images, watershed-based preliminary estimation of the sphere-fittings and optimization of the preliminary sphere-fittings. The program allowed to give satisfactory sphere-fittings in around 98.5% of cases. After user correction, satisfactory sphere-fittings were found for all the beads in the field of view. It was found that the average error made on the estimation of the positions and radii was below 10% of the average bead radius. Furthermore, sphere-fittings were used to give an estimation of the cylinder position, which presented unmeasured variations during the experiments. Sphere-fittings of the beads as tomographed before hole opening, as well as the estimation of the cylinder position were used as initial conditions for 2-stage 3D DEM simulations. In the first stage, the aperture was kept closed and settlement of the beads was awaited. In the second, the hole was opened and again settlement of the beads was awaited. Final configurations found by DEM simulation were compared to the sphere-fittings of the beads as tomographed at the end of the experiments. In seven cases, a good agreement was found between simulation and experiment. This was the case when in the experiment jamming occurred without a substantial flow of the beads. In the two remaining cases, substantial flow had occurred and simulation and experiment did not agree. It is worthwhile noticing that while DEM has already been used to reproduce global phenomena in granular media such as crystallization and segregation, we give here one of the first attempts to reproduce the microstructure. This attempt strongly hints the ability of DEM in doing so. However, we have also seen that DEM predictions of the microstructure are in certain cases unreliable. The real potential of the approach is still unknown. We propose that combining it with ensemble forecasting might enhance this potential.

We also present a study of what we call the statistical physics of granular jamming, i.e. what has to do with the relation between fine-scale and global modeling of granular jamming. In this study, two kinds of fine-scale models are considered: simple models SPM of non-interacting particles and 2D DEM. We have endeavored to find how global parameters such as hole size, number of grains, friction coefficient, grain length, hopper shape can be used to give information on the jamming process.

In the case of simple models, the jamming probability or the average time before jamming

could be expressed analytically as a function of the global parameters. Two simple models were studied: a cellular automaton and a continuous model closely related to the subject of order statistics.

For the continuous model, the formula found for the jamming probability necessitated the introduction of a bi-indexed integer recurrence sequence, giving the number of subsets without u consecutive elements in an ordered set. A simple relation was found between this recurrence sequence and the bi-indexed recurrence sequence giving the number of ways of placing balls into fixed-size urns. Different algorithms to compute both recurrence sequences were given. The complexities of these algorithms were compared. We noticed that depending on what values of the sequence are wanted, one or the other algorithm suits better. This shows that given a granular jamming model there are likely different ways of computing the jamming probability or other quantities of interest, that may be more or less efficient depending on what values are wanted. Albeit these results, the computation of bi-indexed integer recurrence sequences is not well understood. Moreover, the computation of general multi-indexed integer recurrence sequences also.

In the case of 2D DEM, analytical formulas could not be found, and we resorted to simulations to understand how quantities of interest are related to global parameters. We have found that the jamming probability and the average number of grains escaping the hopper appear to be monotonous functions of the number of grains and the friction coefficient. The behavior in this case resembles that of the simple models. However, we have also noticed differences in behavior. For example, the average number of grains escaping the hopper shows a non-monotonic behavior as a function of the grain length and the hopper angle. This phenomenon is not yet understood.

Finally we related SPM to DEM showing that one can be used to locally express the jamming probability for the other.

Increasing the realism of SPM models could be considered in future work. Moreover, the generalization to 3D of certain of the 2D results found in this thesis could also be considered.

Thus the duty of the man who investigates the writings of scientists, if learning the truth is his goal, is to make himself an enemy of all that he reads, and, applying his mind to the core and margins of its content, attack it from every side.

—Alhazen

Bibliography

- C. R. A. Abreu, F. W. Tavares, and M. Castier. Influence of particle shape on the packing and on the segregation of spherocylinders via Monte Carlo simulations. *Powder Technology*, 134: 167–180, 2003.
- R. Al-Raoush and C. Willson. Extraction of physically realistic pore network properties from three-dimensional synchrotron X-ray microtomography images of unconsolidated porous media systems. *J. Hydrol.*, 300:44–64, 2005.
- S. Al-Thyabat and N. J. Miles. An improved estimation of size distribution from particle profile measurements. *Powder Technol.*, 166(3):152–160, 2006.
- C. Ancey, M. Meunier, and D. Richard. Inverse problem in avalanche dynamics models. *Water Resour. Res.*, 39(4), 2003.
- B. Andreotti, P. Claudin, and O. Pouliquen. Aeolian Sand Ripples: Experimental Study of Fully Developed States. *Phys. Rev. Lett.*, 96:028001, 2006.
- M. B. Araújo and M. New. Ensemble forecasting of species distributions. *Trends Ecol. Evol.*, 22(1):42–47, 2006.
- B. C. Arnold, N. Balakrishnan, and H. N. Nagaraja. *A first course in order statistics*. Wiley Series in Probability and Mathematical Statistics: Probability and Mathematical Statistics. John Wiley & Sons Inc., New York, 1992. A Wiley-Interscience Publication.
- T. Aste, M. Saadatfar, A. Sakellariou, and T. Senden. Investigating the geometrical structure of disordered sphere packings. *Physica A*, 339:16–23, 2004.
- R. A. Bagnold. *The Physics of Blown Sand and Desert Dunes*. Methuen London, 1941.
- S. Baik, H. S. Kim, M. H. Jeong, C. S. Lee, J. H. Je, Y. Hwu, and G. Margaritondo. International consortium on phase contrast imaging and radiology beamline at the Pohang Light Source. *Rev. Sci. Instrum.*, 75(11):4355–4358, 2004.
- P. Bak, C. Tang, and K. Wiesenfeld. Self-organized criticality. *Phys. Rev. A*, 62(1):40–43, 1988.
- C. A. Baldwin, A. J. Sederman, M. D. Mantle, P. Alexander, and L. F. Gladden. Determination and Characterization of the Structure of a Pore Space from 3D Volume Images. *J. Colloid Interface Sci.*, 181:79–92, 1996.
- P. Ballesta, A. Duri, and L. Cipelletti. Unexpected drop of dynamical heterogeneities in colloidal suspensions approaching the jamming transition. *Nat. Phys.*, 4(7):550–554, 2008.

- J. M. Bates and C. W. J. Granger. Combination of forecasts. *Operational Research Quarterly*, 20(4):451–468, 1969.
- J. D. Bernal. A Geometrical Approach to the Structure Of Liquids. *Nature*, 183:141–147, 1959.
- J. D. Bernal and J. Mason. Packing of Spheres: Co-ordination of Randomly Packed Spheres. *Nature*, 188:910–911, 1960.
- W. A. Beverloo, H. A. Leniger, and J. van de Velde. The flow of granular solids through orifices. *Chem. Eng. Sci.*, 15(3-4):260–&, 1961.
- E. C. Bingham and R. W. Wikoff. The Flow of Dry Sand through Capillary Tubes. *J. Rheology*, 2:395, 1931.
- T. Börzsönyi, T. C. Hasley, and R. E. Ecke. Avalanche dynamics on a rough inclined plane. *Phys. Rev. E*, 78:011306, 2008.
- R. L. Brown. The Fundamental Principles of Segregation. *J. Inst. Fuel*, 13:15, 1939.
- R. L. Brown. Flow from Bunkers. *Fuel*, 29:220, 1950.
- R. L. Brown. Flow Properties. In *Powders in Industry*. Soc. Chem. Ind., Monograph No. 14, 1961.
- R. L. Brown and P. G. W. Hawksley. The Internal Flow of Granular Masses. *Fuel*, 26:159–173, 1947.
- R. L. Brown and J. C. Richards. Discussion on Mixing in a Cone. *Trans. Instn. Chem. Engrs.*, 37:59, 1959a.
- R. L. Brown and J. C. Richards. Profile of Flow of Granules through Apertures. *Trans. Instn. Chem. Engrs.*, 38:243–256, 1959b.
- R. L. Brown and J. C. Richards. *Principles of Powder Mechanics: Essays on the Packing and Flow of Powders and Bulk Solids*. Pergamon Press, 1970.
- M. E. Cates, J. P. Wittmer, J.-P. Bouchaud, and P. Claudin. Jamming, Force Chains, and Fragile Matter. *Phys. Rev. Lett.*, 81(9):1841–1844, 1998.
- M. P. Ciamarra, M. D. D. Vizia, A. Fierro, M. Tarzia, A. Coniglio, and M. Nicodemi. Granular Species Segregation under Vertical Tapping: Effects of Size, Density, Friction, and Shaking Amplitude. *Phys. Rev. Lett.*, 96(5):058001, 2006.
- R. T. Clemen. Combining forecasts: A review and annotated bibliography. *Int. J. Forecast.*, 5 (4):559–583, 1989.
- E. I. Corwin, H. M. Jaeger, and S. R. Nagel. Structural signature of jamming in granular media. *Nature*, 435(7045):1075–1078, 2005.
- P. A. Cundall and O. D. L. Strack. A discrete numerical model for granular assemblies. *Geotechnique*, 29(1):47–65, 1979.

- D. A. Darling. On a Class of Problems Related to the Random Division of an Interval. *Annals of Mathematical Statistics*, 24(2):239–253, 1953.
- H. A. David. *Order statistics*. John Wiley & Sons Inc., New York, second edition, 1981. Wiley Series in Probability and Mathematical Statistics.
- W. E. Deming and A. L. Mehring. The Gravitational Flow of Fertilizers and other Comminuted Solids. *Ind. Engng. Chem.*, 29:661, 1929.
- L. E. Dickson. *History of the Theory of Numbers*, volume 1. Chelsea Publishing Company, 1971.
- A. Donev, S. Torquato, and F. H. Stillinger. Pair correlation function characteristics of nearly jammed disordered and ordered hard-sphere packings. *Phys. Rev. E*, 71(1, Part 1), 2005.
- A. Drescher, A. J. Waters, and C. A. Rhoades. Arching in hoppers: I. Arching theories and bulk material flow properties. *Powder Techol.*, 84(2):165–176, 1995a.
- A. Drescher, A. J. Waters, and C. A. Rhoades. Arching in hoppers: II. Arching theories and bulk material flow properties. *Powder Techol.*, 84(2):177–183, 1995b.
- J. Duran. *Sands, Powders, and Grains, An Introduction to the Physics of Granular Materials. Partially Ordered Systems*. Springer, 2000. Translated from the French Introduction à la physique des matériaux granulaires, 1997 by Editions Eyrolles, Paris, France.
- M. Ediger. Spatially heterogeneous dynamics in supercooled liquids. *Annu. Rev. Phys. Chem.*, 51:99–128, 2000.
- F. Engelund. Instability of erodible beds. *J. Fluid Mech.*, 42:225–244, 1970.
- G. Enstad. On the theory of arching in mass flow hoppers. *Chem. Eng. Sci.*, 30(10):1273–1283, 1975.
- G. Everest, A. van der Poorten, I. Shparlinski, and Thomas. *Recurrence sequences*, volume 104 of *Mathematical Surveys and Monographs*. American Mathematical Society, Providence, RI, 2003.
- P. Evesque. Analysis of the statistics of sandpile avalanches using soil-mechanics results and concepts. *Phys. Rev. A*, 43(6):2720–2740, 1991.
- J.-A. Ferrez and T. M. Liebling. Dynamic triangulations for efficient detection of collisions between spheres with applications in granular media simulations. *Philos. Mag. B-Phys. Condens. Matter Stat. Mech. Electron. Opt. Magn. Prop.*, 82(8):905–929, 2002.
- J. L. Finney. Random Packings and the Structure of Simple Liquids. I. The Geometry of Random Close Packing. *Proc. R. Soc. London, Ser. A*, 319:479–493, 1970.
- P. F. Fisher and P. Galdies. A computer model for barchan-dune movement. *Comput. Geosci.*, 14(2):229–253, 1988.
- Y. Forterre and O. Pouliquen. Long-surface-wave instability in dense granular flows. *J. Fluid Mech.*, 486:21–50, 2003.

- F. C. Franklin and L. N. Johanson. Flow of Granular Material through a Circular Orifice. *Chem. Engng. Sci.*, 4:119–129, 1955.
- X. Fu, M. Dutt, A. C. Bentham, B. C. Hancock, R. E. Cameron, and J. A. Elliott. Investigation of particle packing in model pharmaceutical powders using X-ray microtomography and discrete element method. *Powder Technol.*, 167(3):134–140, 2006.
- J. Galanis, D. Harries, D. L. Sackett, W. Losert, and R. Nossal. Spontaneous Patterning of Confined Granular Rods. *Phys. Rev. Lett.*, 96(2):028002, 2006.
- F. Garwood. An application of the Theory of Probability to the Operation of Vehicular-Controlled Traffic Signals. *Supplement to the Journal of the Royal Statistical Society*, 7 (1):65–77, 1940.
- S. Geisser. A Bayes approach for combining correlated estimates. *J. Am. Stat. Assoc.*, 60(310): 602–607, 1965.
- M. Greenwood. The Statistical Study of Infectious Diseases. *Journal of the Royal Statistical Society*, 109(2):85–110, 1946.
- P. Hahmann. The formation of sand dunes with consistent currents. *Annalen der Physik*, 39 (13):637–676, 1912.
- S. Henkes and B. Chakraborty. Jamming as a critical phenomenon: A field theory of zero-temperature grain packings. *Phys. Rev. Lett.*, 95(19), 2005.
- H. J. Herrmann and G. Sauermann. The shape of dunes. *Physica A*, 283:24–30, 2000.
- C. Hogue. *Computer modelling of the motions of granular particles*. Phd thesis, University of Cambridge, 1993.
- L. Holst. On the Lengths of the Pieces of a Stick Broken at Random. *Journal of Applied Probability*, 17(3):623–634, 1980.
- A. Huber. Schwallwellen in Seen als Folge von Felsstürzen. *Mitteilung No. 47 der Versuchsanstalt für Wasserbau, Hydrologie und Glaziologie an der ETH*, pages 1–122, 1980.
- A. W. Jenike. Better Design for Bulk Handling. *Chem. Engng.*, 61:175–180, 1954.
- A. W. Jenike. Gravity flow of bulk solids. *Bulletin 108, Utah University*, 1961.
- J. F. Kennedy. The mechanics of dunes and antidunes in erodible-bed channels. *J. Fluid Mech.*, 16:521–544, 1963.
- A. S. Keys, A. R. Abate, S. C. Glotzer, and D. J. Durian. Measurement of growing dynamical length scales and prediction of the jamming transition in a granular material. *Nat. Phys.*, 3 (4):260–264, 2007.
- G. Kuwabara and K. Kono. Restitution coefficient in a collision between two spheres. *Jap. J. Appl. Phys.*, 26(8):1230–1233, 1987.
- R. Kvapil. *The Theory of Flow of Bulk Materials*. Berlin, VEB Verlag Technik, 1959.

- J. Lambert, I. Cantat, R. Delannay, A. Renault, F. Graner, J. A. Glazier, I. Veretennikov, and P. Cloetens. Extraction of relevant physical parameters from 3D images of foams obtained by X-ray tomography. *Colloid Surf. A-Physicochem. Eng. Asp.*, 263(1-3):295–302, 2005. 5th European Conference on Foams, Emulsions and Applications (EUFOAM 2004), Champs sur Marne, FRANCE, JUL 05-08, 2004.
- P.-S. Laplace. *Deuxième supplément à la Théorie Analytique des Probabilités*. 1818.
- P. Lévy. Sur la division d'un segment par des points choisis au hasard. *C. R. Acad. Sci. Paris*, 208:147–149, 1939.
- W. B. Lindquist, S.-M. Lee, D. A. Coker, K. W. Jones, and P. Spanne. Medial axis analysis of void structure in three-dimensional tomographic images of porous media. *J. Geophys. Res.*, 101(B4):8297–8310, 1996.
- A. J. Liu and S. R. Nagel. Nonlinear dynamics - Jamming is not just cool any more. *Nature*, 396(6706):21–22, 1998.
- A. Longjas, C. Monterola, and C. Saloma. Force analysis of jamming with disks of different sizes in a two-dimensional hopper. *J. Stat. Mech.-Theory Exp.*, 2009.
- E. N. Lorenz. Deterministic Nonperiodic Flow. *J. Atmos. Sci.*, 20:130–141, 1963.
- K. Lu, E. E. Brodsky, and H. P. Kavehpour. A thermodynamic unification of jamming. *Nat. Phys.*, 4(5):404–407, 2008.
- E. Lucas. *Théorie des nombres. Tome I: Le calcul des nombres entiers, le calcul des nombres rationnels, la divisibilité arithmétique*. Nouveau tirage augmenté dun avant-propos de Georges Bouligand. Librairie Scientifique et Technique Albert Blanchard, Paris, 1961.
- V. J. Lumelsky. On Fast Computation of Distance Between Line Segments. *Inf. Process. Lett.*, 21(2):55–61, 1985.
- M. Mailman, C. F. Schreck, C. S. O'Hern, and B. Chakraborty. Jamming in Systems Composed of Frictionless Ellipse-Shaped Particles. *Phys. Rev. Lett.*, 102(25), 2009.
- T. S. Majmudar, M. Sperl, S. Luding, and R. P. Behringer. Jamming transition in granular systems. *Phys. Rev. Lett.*, 98(5), 2007.
- C. Mankoc, A. Garcimartin, I. Zuriguel, D. Maza, and L. A. Pugnaloni. Role of vibrations in the jamming and unjamming of grains discharging from a silo. *Phys. Rev. E*, 80(1, Part 1), 2009.
- A. J. Matchett. The shape of the cohesive arch in hoppers and silos - Some theoretical considerations. *Powder Technol.*, 171(3):133–145, 2007.
- R. Meldau and E. Stach. The Fine Structure of Powders in Bulk with Special Reference to Pulverised Coal. *J. Inst. Fuel*, 7:336–354, 1934.
- P. A. P. Moran. The Random Division of a Interval. *Supplement to the Journal of the Royal Statistical Society*, 9:92–98, 1947.

- D. Müller. *Techniques informatiques efficaces pour la simulation de milieux granulaires par des méthodes d'éléments distincts*. Thèse N° 1545, EPFL, 1996.
- B. S. Neumann. Chapter 10, “Powders”. *Flow Properties of Disperse Systems*, pages 382–422, 1953.
- I. Newton. *Philosophiae Naturalis Principia Mathematica*. 1687.
- C. S. O’Hern, L. E. Silbert, A. J. Liu, and S. R. Nagel. Jamming at zero temperature and zero applied stress: The epitome of disorder. *Phys. Rev. E*, 68(1, Part 1), 2003.
- Y. Oyama. Horizontal Rotating Cylinder. *Bull. Inst. Phys. Chem. Res. (Tokyo)*, page 6001, 1939.
- J. Perdijon. *Histoire de la physique*. Dunod, 2008.
- L. Pournin. *On the behavior of spherical and non-spherical grain assemblies, its modeling and numerical simulation*. Thèse N° 3378, EPFL, 2005.
- L. Pournin and T. M. Liebling. From Spheres to Spheropolyhedra: Generalized Distinct Element Methodology and Algorithm Analysis. In W. J. Cook and L. Lovasz and J. Vygen, editor, *RESEARCH TRENDS IN COMBINATORIAL OPTIMIZATION*, pages 347–363, HEIDELBERGER PLATZ 3, D-14197 BERLIN, GERMANY, 2009. SPRINGER-VERLAG BERLIN. Workshop on Research Trends in Combinatorial Optimization, Bonn, GERMANY, NOV 03-07, 2008.
- L. Pournin, T. M. Liebling, and A. Mocellin. Molecular-dynamics force models for better control of energy dissipation in numerical simulations of dense granular media. *Phys. Rev. E*, 65(1, Part 1), 2002.
- L. Pournin, M. Ramaioli, P. Folly, and T. M. Liebling. About the influence of friction and polydispersity on the jamming behavior of bead assemblies. *Eur. Phys. J. E*, 23(2):229–235, 2007.
- L. Pournin, M. Tsukahara, and T. M. Liebling. Particle shape versus friction in granular jamming. In *Powders and Grains 2009, AIP Conference Proceedings 1145*, pages 499–502. American Institute of Physics, 2009.
- L. Pournin, M. Weber, M. Tsukahara, J.-A. Ferrez, M. Ramaioli, and T. M. Liebling. Three-dimensional distinct element simulation of spherocylinder crystallization. *Granular matter*, 7(2-3):119–126, 2005.
- J. Rajchenbach. Flow in Powders: From Discrete Avalanches to Continuous Regime. *Phys. Rev. Lett.*, 65(18):2221–2224, 1990.
- M. Ramaioli. *Granular flow simulations and experiments for the food industry*. Thèse N° 3997, EPFL, 2008.
- M. Ramaioli, L. Pournin, and T. M. Liebling. Vertical ordering of rods under vertical vibration. *Phys. Rev. E*, 76(2, Part 1):021304, 2007.

- W. S. Rasband. Computer code IMAGEJ. U.S. National Institutes of Health, Bethesda, MD, <http://rsb.info.nih.gov/ij/>, 2006.
- J. M. Rausch. *Gravity Flow of Solid Beds in Vertical Towers*. PhD thesis, Chem. Engng. Dept., Univ. Princeton, 1949.
- P. Richard, P. Philippe, F. Barbe, S. Bourlès, X. Thibault, and D. Bideau. Analysis by x-ray microtomography of a granular packing undergoing compaction. *Phys. Rev. E*, 68:020301(R), 2003.
- K. J. Richards. The formation of ripples and dunes on an erodible bed. *J. Fluid Mech.*, 99: 597–618, 1980.
- A. Rosato, K. J. Strandburg, F. Prinz, and R. H. Swendsen. Why the Brazil Nuts Are on Top: Size Segregation of Particulate Matter by Shaking. *Phys. Rev. Lett.*, 58:1038–1040, 1987.
- H. E. Rose and T. Tanaka. Rate of Discharge of Granular Materials from Bins and Hoppers. *Engineer*, 208:465, 1959.
- M. Saadatfar, A. Kabla, T. J. Senden, and T. Aste. The geometry and the number of contacts of monodisperse sphere packs using X-ray tomography. In R. García-Rojo, H. J. Herrmann, and S. McNamara, editors, *Powders and Grains*, pages 33–36. Taylor and Francis Group, London, 2005.
- F. Sanders. On subjective probability forecasting. *J. Appl. Meteorol.*, 2:191–201, 1963.
- G. Sauermann, P. Rognon, A. Poliakov, and H. J. Herrmann. The shape of the barchan dunes of Southern Morocco. *Geomorphology*, 36:47–62, 2000.
- S. B. Savage and K. Hutter. The motion of a finite mass of granular material down a rough incline. *J. Fluid Mech.*, 199:177–215, 1989.
- T. Schnautz, R. Brito, C. A. Kruelle, and I. Rehberg. A Horizontal Brazil-Nut Effect and Its Reverse. *Phys. Rev. Lett.*, 95(2):028001, 2005.
- G. D. Scott. Packing of Spheres: Packing of Equal Spheres. *Nature*, 188:908–909, 1960.
- A. J. Sederman, P. Alexander, and L. F. Gladden. Structure of packed beds probed by Magnetic Resonance Imaging. *Powder Technol.*, 117:255–269, 2001.
- G. Seidler, G. Martinez, L. Seeley, K. Kim, E. Behne, S. Zaranek, B. Chapman, S. Heald, and D. Brewe. Granule-by-granule reconstruction of a sandpile from x-ray microtomography data. *Phys. Rev. E*, 62(6):8175–8181, 2000.
- B. Sherman. A Random Variable Related to the Spacing of Sample Values. *Annals of Mathematical Statistics*, 21(3):339–361, 1950.
- L. E. Silbert, D. Ertaş, G. S. Grest, T. C. Halsey, and D. Levine. Analogies between granular jamming and the liquid-glass transition. *Phys. Rev. E*, 65(5, Part 1), 2002a.
- L. E. Silbert, D. Ertaş, G. S. Grest, T. C. Halsey, and D. Levine. Geometry of frictionless and frictional sphere packings. *Phys. Rev. E*, 65(3, Part 1), 2002b.

- L. E. Silbert, A. J. Liu, and S. R. Nagel. Structural signatures of the unjamming transition at zero temperature. *Phys. Rev. E*, 73(4, Part 1), 2006.
- P. Spanne, J. F. Thovert, C. J. Jacquin, W. B. Lindquist, K. W. Jones, and P. M. Adler. Synchrotron computed microtomography of porous media: Topology and transports. *Phys. Rev. Lett.*, 73:2001–2004, 1994.
- P. T. Stainforth and R. C. Ashley. An Analytical Hopper Design Method for Cohesive Powders. *Powder Technol.*, 7:215–243, 1973.
- C. Tang and P. Bak. Critical Exponents and Scaling Relations for Self-Organized Critical Phenomena. *Phys. Rev. Lett.*, 60(23):2347–2350, 1988.
- K. To. Effect of Hopper Angles on Jamming Probability in 2-Dimensional Hoppers. *Chin. J. Phys.*, 40(4):379–386, 2002.
- K. To. Jamming transition in two-dimensional hoppers and silos. *Phys. Rev. E*, 71(6, Part 1): 060301, 2005.
- K. To, P.-Y. Lai, and H. K. Pak. Jamming of Granular Flow in a Two-dimensional Hopper. *Phys. Rev. Lett.*, 86(1):71–74, 2001.
- D. Train. Some Aspects of the Property of Angle of Repose of Powders. *J. Pharm. Pharmac.*, 10:127T–135T, 1958.
- V. Trappe, V. Prasad, L. Cipelletti, P. N. Segre, and D. A. Weitz. Jamming phase diagram for attractive particles. *Nature*, 411(6839):772–775, 2001.
- W. L. Tsai, P. C. Hsu, Y. Hwu, J. H. Je, Y. Ping, H. O. Moser, A. Groso, and G. Margaritondo. Edge-enhanced radiology with broadband synchrotron X-rays. *Nucl. Instrum. Methods Phys. Res. Sect. B-Beam Interact. Mater. Atoms*, 199:436–440, 2003. 3rd International Conference on Synchrotron Radiation in Materials Science, SINGAPORE, SINGAPORE, JAN 21-24, 2002.
- M. Tsukahara. Web page with DEM simulations and DEM-experiment comparisons. <http://ima.epfl.ch/~tsukahar/public-data>, 2009.
- M. Tsukahara, S. Mitrovic, V. Gajdosik, G. Margaritondo, L. Pournin, M. Ramaioli, D. Sage, Y. Hwu, M. Unser, and T. M. Liebling. Coupled tomography and distinct-element-method approach to exploring the granular media microstructure in a jamming hourglass. *Phys. Rev. E*, 77(6, Part 1), 2008.
- M. Tsukahara, L. Pournin, and T. M. Liebling. Simple Probabilistic Modeling of Granular Jamming and Validation Using DEM. In *Powders and Grains 2009, AIP Conference Proceedings 1145*, pages 507–510. American Institute of Physics, 2009.
- University of Wisconsin Madison. Condor High Throughput Computing web page. <http://www.cs.wisc.edu/condor>.
- L. Vanel, A. D. Rosato, and R. N. Dave. Rise-Time Regimes of a Large Sphere in Vibrated Bulk Solids. *Phys. Rev. Lett.*, 78(7):1255–1258, 1997.

- C. Vega and S. Lago. A Fast Algorithm to Evaluate the Shortest Distance Between Rods. *Comput. Chem.*, 18(1):55–59, 1994.
- F. X. Villarruel, B. E. Lauderdale, D. M. Mueth, and H. M. Jaeger. Compaction of rods: Relaxation and ordering in vibrated, anisotropic granular material. *Phys. Rev. E*, 61(6, Part B): 6914–6921, 2000.
- L. Vincent and P. Soille. Watersheds in digital spaces - an efficient algorithm based on immersion simulations. *IEEE Trans. Pattern Anal. Mach. Intell.*, 13(6):583–598, 1991.
- D. M. Walker. An approximate theory for pressures and arching in hoppers. *Chem. Eng. Sci.*, 21:975–997, 1966.
- O. R. Walton and R. L. Braun. Viscosity, Antigranulocytes-Temperature, and Stress Calculations for Shearing Assemblies of Inelastic, Frictional Disks . *J. Rheol.*, 30(5):949–980, 1986.
- L. Weiss. The Limiting Joint Distribution of the Largest and Smallest Sample Spacings. *Annals of Mathematical Statistics*, 30(2):590–593, 1959.
- L. Weiss. Joint Asymptotic Distribution of the k-Smallest Sample Spacings. *Journal of Applied Probability*, 6(2):442–448, 1969.
- K. Wieghardt. Some Experiments on Flow in Sand. *Ingenieur.-Archiv.*, 20:109–115, 1952.
- E. F. Wolf and H. L. von Hohenleiten. Experimental Study of the Flow of Coal in Chutes. *Trans. Am. Soc. Mech. Engrs.*, 67:585–599, 1945.
- E. F. Wolf and H. L. von Hohenleiten. Flow of Coal in Chutes. *Mech. Engng.*, 70:313–314, 1948.
- F. A. Zenz and D. F. Othmer. *Fluidization and Fluid Particle Systems*. New York, Reinhold Pub. Corp., 1960.
- I. Zuriguel, A. Garcimartin, D. Maza, L. A. Pugnaloni, and J. M. Pastor. Jamming during the discharge of granular matter from a silo. *Phys. Rev. E*, 71(5, Part 1):051303, 2005.
- I. Zuriguel, L. A. Pugnaloni, A. Garcimartín, and D. Maza. Jamming during the discharge of grains from a silo described as a percolating transition. *Phys. Rev. E*, 68(3, Part 1):030301, 2003.

Michel Tsukahara
Born February 15, 1976

rosowww.epfl.ch/mts
tsukaharamichel@yahoo.fr

EDUCATION

- | | | |
|--------------------|---|--|
| 2006 – 2009 | École Polytechnique Fédérale de Lausanne , Lausanne, Switzerland:
<i>PhD under the supervision of Prof. Th. M. Liebling</i>
<i>Thesis subject: "Jamming in Granular Media: Experiments and Models"</i> | www.epfl.ch |
| 1994 – 2003 | École Polytechnique Fédérale de Lausanne , Lausanne, Switzerland:
<i>Degree in mathematical engineering of the EPFL obtained October 2003</i> | www.epfl.ch |
| 1991 – 1994 | Lycée International de Ferney-Voltaire , Ferney-Voltaire, France:
<i>Baccalauréat C (scientific) obtained July 1994</i> | www.lyferney.net |

PROFESSIONAL EXPERIENCE

- | | | |
|--------------------|---|--|
| 2003 – 2009 | EPFL–Institute of Mathematics-Chair of Operations Research, Lausanne:
<i>Assistant of Prof. Th. M. Liebling</i> | www.epfl.ch |
| 1998 – 1999 | EPFL–Special Mathematics Course, Lausanne:
<i>Student-assistant</i> | cms.epfl.ch |
| 1995 – 1998 | Institut Gamma, Lausanne:
<i>Student-assistant</i> | www.institutgamma.ch |

PUBLICATIONS

- | | |
|-------------|--|
| 2009 | L. Pournin, M. Tsukahara and Th. M. Liebling, <i>Particle shape versus friction in granular jamming</i> , Powders and Grains 2009, AIP Conference Proceedings 1145, 499-502, M. Nakagawa and S. Luding (Editors) (2009) |
| 2009 | M. Tsukahara, L. Pournin and Th. M. Liebling, <i>Simple probabilistic modeling of granular jamming and validation using DEM</i> , Powders and Grains 2009, AIP Conference Proceedings 1145, 507-510 M. Nakagawa and S. Luding (Editors) (2009) |
| 2008 | M. Tsukahara, S. Mitrovic, V. Gajdosik, G. Margaritondo, L. Pournin, M. Ramaioli, D. Sage, Y. Hwu, M. Unser and Th. M. Liebling, <i>Coupled tomography and distinct-element-method approach to exploring the granular media microstructure in a jamming hourglass</i> , Phys. Rev. E 77, 061306 (2008) |
| 2005 | L. Pournin, M. Weber, M. Tsukahara, J.-A. Ferrez, M. Ramaioli and Th. M. Liebling, <i>Three-dimensional distinct element simulation of spherocylinder crystallization</i> , Granular Matter 7, 119-126 (2005) |

VARIOUS

- | | |
|-------------------|--|
| Personal: | Swiss, married, 2 children |
| Languages: | Fluent in French and English, notions of Japanese and German |